

## Numerical simulation of cavitating water jet issuing from an orifice nozzle

Guoyi Peng \*  
College of Engineering, Nihon University

Seiji Shimizu  
College of Engineering, Nihon University

Shigeo Fujikawa  
Graduate School of Engineering, Hokkaido University

\* peng@mech.ce.nihon-u.ac.jp

### ABSTRACT

Concerned on the numerical simulation of high-speed water jet accompanied with intensive cavitation, a practical compressible mixture flow method is developed by coupling a simplified estimation of bubble cavitation and a flexible compressible flow computation procedure. The fluid media of cavitating water jet are treated as a mixture of liquid and bubbles, and the mean flow of the two-phase mixture is calculated under the assumption of locally homogeneous medium by neglecting the velocity slip between liquid and bubbles. Reynolds Averaged Navier-Stokes equations for compressible fluids are used to describe the unsteady flow field, and the intensity of cavitation in a local field is evaluated by the volume fraction of gas phase varying with the mean flow.

High speed submerged water jets issuing from an orifice nozzle are treated. Both cavitating and non-cavitating flows are investigated under different cavitation number to clarify the behavior of cavitating jet. The results demonstrate that pressure decreases sharply at the entrance of nozzle throat and cavitation occurs initially in the shear layer near the entrance of throat. Under the effect of cavitation the discharge coefficient decreases obviously compared to the case of no-cavitating jet although the maximum velocity in the throat increases.

### NOMENCLATURE

$c$	Sonic speed in a fluid
$c_q$	discharge coefficient
$d$	diameter of nozzle
$g$	Gravity
$n$	Specific heat ratio
$p$	Pressure
$t$	Time [s]
$\mathbf{u}$	Velocity vector
$\alpha$	Fluid volume fraction
$\mu$	Dynamic viscosity
$\rho$	Density
$\sigma$	Cavitation number
$\tau$	Stress tensor

Subscripts:

$L$  Liquid phase

$G$  Gas phase  
 $M$  Mixture

### 1. INTRODUCTION

High-speed water jets have been applied in many fields of industries such as cleaning of complicated mechanical products, cutting of solid materials, etc. As a new technology utilizing cavitation phenomena effectively, submerged water jets have received much attention [1]. However, the structure of high-speed cavitating jet and the behavior of unsteady cavitation bubbles are still unclear because of the difficulty for observing the interior of cavitating flows. For the purpose of performance prediction and efficient design of water jet devices much attention has been attracted to the numerical simulation of cavitating flow. Modeling of cavitation has been studied from different view points [3] and methods developed can be mainly classified into two different categories of two-fluid one and two-phase mixture flow one. The two-fluid method treats cavitation phenomena by computing liquid and gas flows separately, and the computed flow fields strongly depend upon physical models used for evaluating the interaction between the liquid and bubbles [4]. For lack of a general method evaluating the interaction of liquid and bubbles an extra effort is required in applying the method to high-speed cavitating jets.

On the other hand, cavitation usually takes place in low-pressure regions of relative high velocity and the size of cavitation bubbles is very small compared to its flow field. Cavitation bubbles and the working liquid may be sufficiently mixed and their relative motion in a small local area is often insignificant. Thus, the so-called two-phase flow method treats the flows of liquid and cavitation bubbles together by assuming that they flow at the same velocity. For its convenience the method is often used under certain simplifications of flow phenomena by combined with some cavitation models [5]. Generally, the computation of two-phase mixture model is cheaper than that of two-fluid model because there is no need to treat the motion of a mass of cavitation bubbles separately but there is a difficulty for dealing with the sharp density variation caused by cavitation.

Focused on the numerical prediction of turbulent cavitating flow, this paper presents a practical compressible mixture flow method by coupling a simplified estimation of bubble cavitation

and a compressible mixture flow computation [7]. Two-phase fluid media of cavitating flow are treated as a mixture of liquid and spherical gas bubbles which are supposed to disperse uniformly in the liquid. The mean flow of two-phase mixture is calculated by Navier-Stokes equations for compressible fluids and the intensity of cavitation in a local field is then evaluated by the volume fraction of gas phase varying with the mean flow. Turbulent cavitating flows of submerged water jet issuing from an orifice nozzle are treated under different conditions, and the reliability of numerical computation is confirmed by comparing the computational results with experimental data available.

## 2. COMPRESSIBLE HOMOGENEOUS MIXTURE FLOW BUBBLE CAVITATION MODEL

### 2.1 Compressibility of Bubble-liquid Mixture

The fluid media of cavitating flow are taken as a two-phase mixture of working liquid and cavitation bubbles. The gas phase is supposed to disperse in the liquid phase and its volume fraction is denoted as  $\alpha_G$ . The liquid volume fraction is written to be  $\alpha_L$ . Then, the density of two-phase mixture is defined as follows by volume averaging.

$$\rho_M = \rho_L \alpha_L + \rho_G \alpha_G \quad (1)$$

Concerning the compressibility of the two-phase mixture, the variation of mixture density can be written as follows by taking the differential of above equation.

$$\frac{d\rho_M}{dt} = \alpha_G \frac{d\rho_G}{dt} + \alpha_L \frac{d\rho_L}{dt} + (\rho_G - \rho_L) \frac{d\alpha_G}{dt} \quad (2)$$

Considering the continuity of mixture flow, we may arrange it to the following form.

$$\frac{1}{\rho_M} \frac{d\rho_M}{dt} = \frac{\alpha_G}{\rho_G} \frac{d\rho_G}{dt} + \frac{\alpha_L}{\rho_L} \frac{d\rho_L}{dt} \quad (3)$$

According to the definition of compressibility the above equation is then written as follows.

$$\frac{1}{\rho_M} \frac{d\rho_M}{dt} = \frac{\alpha_G}{\rho_G c_G^2} \frac{dp_G}{dt} + \frac{\alpha_L}{\rho_L c_L^2} \frac{dp_L}{dt} \quad (4)$$

where  $p$  and  $c$  denote pressure and sonic speed in a given fluid respectively. Both the liquid and the gas included in bubbles are supposed to work exponentially and their state equations are given as follows.

$$\frac{p_L + B}{p_0 + B} = \left( \frac{\rho_L}{\rho_{L0}} \right)^{n_L}, \quad \frac{p_G}{p_{G0}} = \left( \frac{\rho_G}{\rho_{G0}} \right)^{n_G} \quad (5)$$

Here the subscript 0 denotes a reference state which is taken to be the atmospheric one and  $B$  is a constant given to be  $3.049 \times 10^8$  Pa. Then, sonic speeds in the liquid and gas media are written as the function of working pressure.

$$\rho c_L^2 = n_L (p_L + B), \quad \rho c_G^2 = n_G p_G \quad (6)$$

According to above we understand that the compressibility of the two-phase mixture depends upon the volume fraction of gas phase as well as the variation of gas pressure, which is determined by bubble size. Thus, the compressibility of a bubble-liquid mixture needs be evaluated based on a careful

consideration of bubble dynamics, but it is very time consuming. In order to work out a practical method for engineering applications a simplification on the gas pressure that  $dp_G/dt \approx dp_L/dt$  is adopted and then Eq. (4) is arranged to the following form.

$$\frac{1}{\rho_M} \frac{d\rho_M}{dt} = \frac{1}{\rho_M c_M^2} \frac{dp_L}{dt} \quad (7)$$

where the average sonic speed in the mixture is defined by the following equation.

$$\frac{1}{\rho_M c_M^2} \equiv \frac{\alpha_G}{\rho_G c_G^2} + \frac{\alpha_L}{\rho_L c_L^2} \quad (8)$$

### 2.2 Governing Equations for Turbulent Cavitating Flow

The mean flow of two-phase mixture consisting of liquid and bubbles is concerned by neglecting their relative velocity slip. Considering the variation of mixture density caused by cavitation, Reynolds Averaged Navier-Stokes equations for compressible fluid are used as main flow governing equations. The variation of temperature caused by cavitation is thought to be very small in the whole flow field and thus the conservation equation of energy is omitted in this work. Conservation equations of mass and momentum are given as follows in vector form. For convenience the subscript  $M$  denoting the fluid mixture is omitted hereafter.

$$\frac{\partial \rho}{\partial t} + \mathbf{u} \cdot \nabla \rho = -\rho \nabla \cdot \mathbf{u} \quad (9)$$

$$\rho \frac{\partial \mathbf{u}}{\partial t} + \rho (\mathbf{u} \cdot \nabla) \mathbf{u} = -\nabla p + \nabla \cdot \boldsymbol{\tau} + \mathbf{g} \quad (10)$$

where  $\boldsymbol{\tau}$  denotes the stress tensor and its components are given as follows.

$$\tau_{ij} = 2\mu S_{ij} - \frac{2}{3}\mu (\nabla \cdot \mathbf{u}) \delta_{ij} - \overline{\rho u_i u_j} \quad (11)$$

in which  $i$  and  $j$  denote respectively three components of the coordinates.  $\delta_{ij}$  denotes the Kronecker delta and  $S_{ij}$  does the strain tensor.  $-\overline{\rho u_i u_j}$  does the Reynolds stress, which is evaluated by the RNG  $k$ - $\varepsilon$  turbulence model for high Reynolds number turbulent flow.  $\mu$  denotes the mean viscosity of the two-phase mixture and it is estimated with the following formula [8].

$$\mu = \alpha_L (1 + 2.5\alpha_G) \mu_L + \alpha_G \mu_G \quad (12)$$

In order to close above equations, the relation of mixture density and pressure given in Eq. (7) is applied and the following pressure transport equation is then derived considering the flow continuity.

$$\frac{\partial p}{\partial t} + \mathbf{u} \cdot \nabla p = -\rho c^2 \nabla \cdot \mathbf{u} \quad (13)$$

Furthermore, to estimate the variation of gas volume fraction the following gas mass conversation equation is employed.

$$\frac{\partial}{\partial t} (\rho_G \alpha_G) + \mathbf{u} \cdot \nabla (\rho_G \alpha_G) = -(\rho_G \alpha_G) \nabla \cdot \mathbf{u} \quad (14)$$

where  $\rho_G \alpha_G$  denotes the gas mass fraction. Here the vapor evaporation and condensation in cavitation bubbles are supposed to be negligible for the purpose of simplification.

Equations (9), (10), (13), (14) compose a set of cavitating flow governing equations. For the coexistence of strong compressible bubbly flow region and weak compressible liquid flow region in cavitating water jet these equations are solved by the CIP-CUP method [9] based on the time splitting technique. The advection phase is calculated by CIP scheme, and the non-advection phase is calculated by finite difference method, where the viscous term and the acoustic term are respectively discretized by explicit and implicit schemes respectively. The mean pressure is then calculated by solving the Poisson equation of pressure variation [10]. Validations of the computer code may refer to reference [11].

### 3. COMPUTATIONAL RESULTS AND DISCUSSIONS

High-speed water jet issuing from a submerged nozzle is usually encountered in engineering practice and it has received much attention for the effect of cavitations. Its numerical simulation is still a challenging because strong cavitations may be caused in such turbulent jet by a high flow driving pressure. In this work, submerged water jets issuing from a sharp-edged circular orifice are treated under different flow conditions and the computation results are compared with experimental data available [12]. Geometry parameters of the orifice concerned are  $L/d=5.0$  and  $D/d=2.88$ , where  $L$  denote the length of orifice and  $D$  does the inlet diameter. As an index of cavitation inception, the following device cavitation number is defined for a given jet.

$$\sigma = \frac{P_o - P_v}{P_{in} - P_o} \quad (15)$$

where  $P_{in}$  denotes the total driving pressure,  $P_o$  the discharge static pressure and  $P_v$  the saturated vapor pressure. The discharge coefficient  $c_q$  of jet nozzle is defined as follows.

$$c_q = \frac{q_m}{0.25\pi d^2 \sqrt{2\rho_L(P_{in} - P_o)}} \quad (16)$$

where  $q_m$  denotes the mass flow rate under given condition.

Figure 1 shows the geometry of orifice nozzle concerned as well as the computational domain and the computational mesh adopted. Focused on the symmetric vortex structure before it falls down the circumferential variation is neglected and the assumption of axi-symmetric flow is adopted here. The upstream boundary is taken to  $9d$  upstream of the throat and the downstream boundary is taken to  $50d$  downstream of the nozzle exit. The surrounding boundary is taken to  $20d$  in radial, which is treated to be solid one. For the flow computations, a pressure condition is imposed at the inlet according to the total pressure specified. At the outlet a flow-dependent static pressure is imposed to restrain the reflection of pressure wave. At all the wall boundaries except above the no-slip condition is applied.

At first, concerning the structure of no-cavitation flow numerical simulations were performed under a large cavitation number by specifying a discharge pressure high enough for a given driven pressure difference. As an example, Fig. 2 shows the distribution of no-cavitaing jet when the driving pressure  $\Delta p \cong 10p_o$ , here  $p_o$  denotes the standard atmospheric pressure

( $\sigma \geq 2.5$ ). According to the result the mean velocity of jet reaches to 45m/s and the Reynolds number is about  $Re \cong 4.5 \times 10^5$ . Figure 2 (a) and (b) show the contour maps of axial velocity  $u$  and pressure  $p$  at a well-developed state. As shown in the figures, the flow accelerates near the entrance of throat. Pressure decreases at the entrance corresponding to the increase of flow velocity, and a low-pressure region is formed near the wall at the entrance of throat, where cavitation is easy to take place. Figure 2 (c) and (d) shows the structure of no-cavitaing jet in the local areas of orifice entrance and exit. The results demonstrate that a small separation vortex is caused in the low-pressure region at the entrance and a large vortex is formed at the exit of orifice.

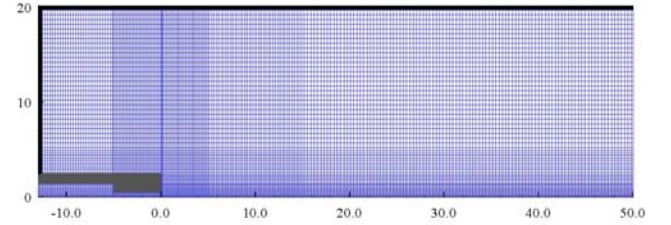
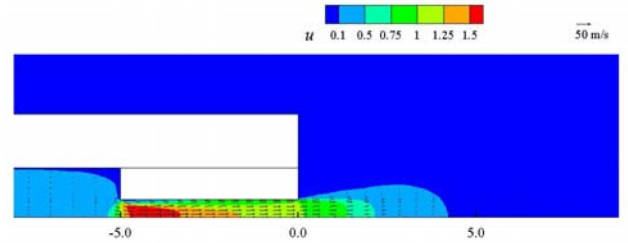
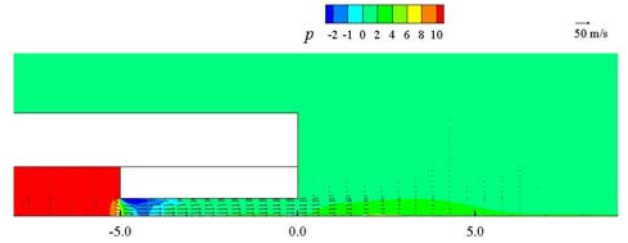


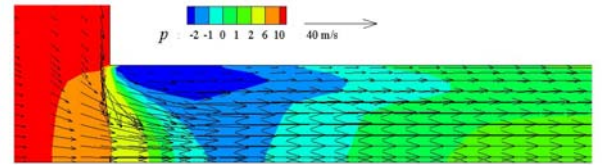
Figure 1 Computational domain and mesh



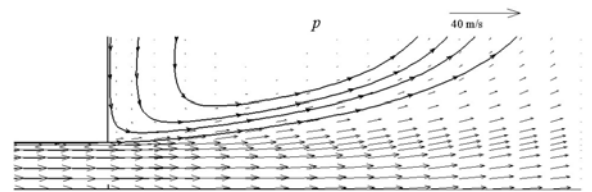
(a) Velocity



(b) Pressure



(c) Low-pressure region at the entrance



(d) Vortex at the exit

Figure 2 Flow distribution of no-cavitaing jet ( $\sigma \geq 2.5$ )

With a special concern on cavitation, water jets injected at a low cavitation number are investigated by decreasing the discharge pressure. Figure 3 shows, as a sample, the temporal variation of gas volume fraction where the driving pressure is kept to  $\Delta p \cong 10 p_0$  and the cavitation number  $\sigma$  is decreased to 0.1 by adjusting the discharge pressure to the atmospheric one. Figure 3 (a) to (f) present the contour maps of  $\alpha_G$  in a sequence time, where  $\alpha_G$  increases to 0.8 locally when the flow gets to be well-developed. The result demonstrates that cavitation take place initially in the shear layer at the entrance of throat. According to Figure 3 (b) to (d) we understand that  $\alpha_G$  increases gradually with developing of jet flow and cavitation bubbles flow downstream along the shear layer between the jet and surrounding water.

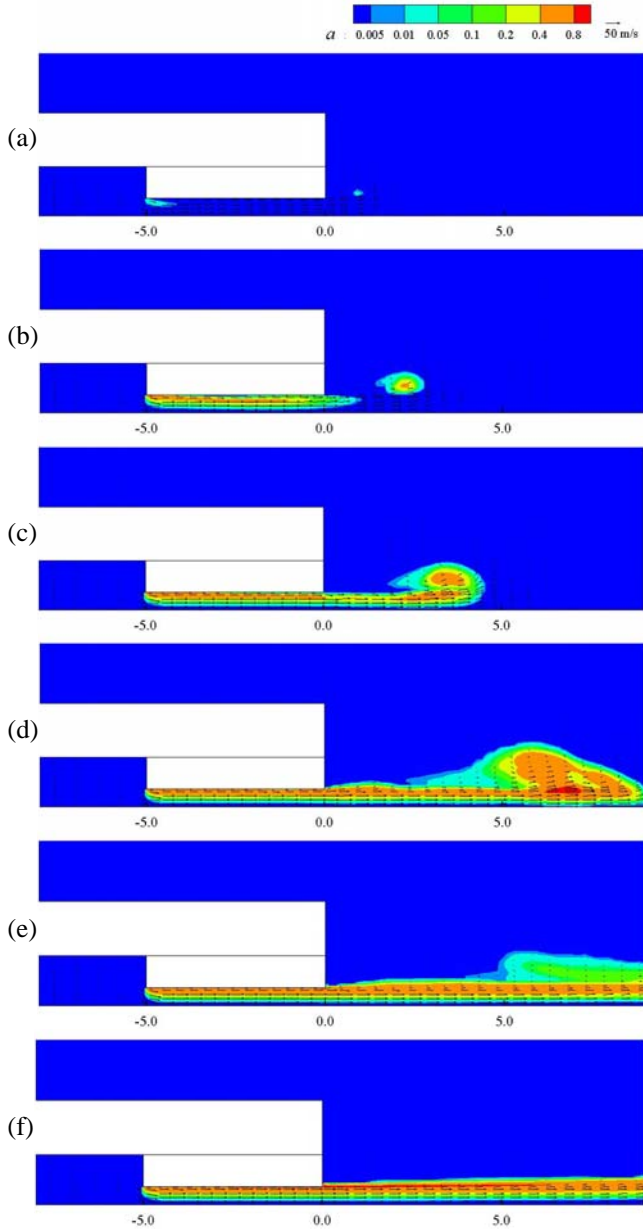


Fig. 3 Development of cavitating jet ( $\sigma = 0.1$ )

Figure 4 shows the distribution of gas volume fraction in submerged water jets under different cavitation numbers. Figure 4 (a) presents the contour map of  $\alpha_G$  and the distribution of velocity vector at a well-developed stage when the jet driving pressure  $\Delta p \cong 0.1$  MPa and  $\sigma > 2.0$ , where the maximum value of  $\alpha_G$  is less than 0.005 and no noticeable cavitation has been caused. Figure 4 (b), (c) and (d) respective present the contour maps of  $\alpha_G$  when the cavitation number is decreased to 0.1, 0.05, 0.02, where the driving pressure is increased to 1.0MPa, 2.0MPa, and 5.0MPa. The figure demonstrates that the value of  $\alpha_G$  locally increases to 0.5 when  $\sigma$  is decreased to 0.1, and thus the occurrence of cavitation is confirmed. Comparing Fig. 4 (b), (c) and (d) we understand that the maximum value of  $\alpha_G$ , which indicates the intensity of cavitation, increases gradually up to 0.8 and then keeps almost the same when the cavitation number is decreased further to 0.05. However, the area of strong cavitation, which is denoted by high value of  $\alpha_G$ , increases with the

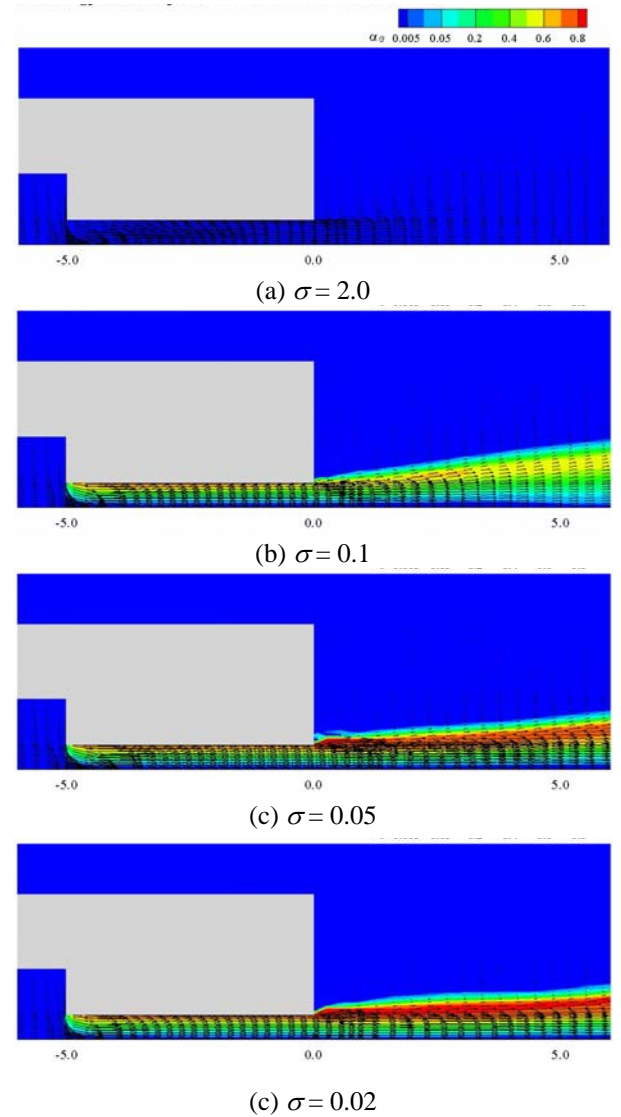


Fig. 4 Distribution of gas volume fraction in jets under different cavitation number

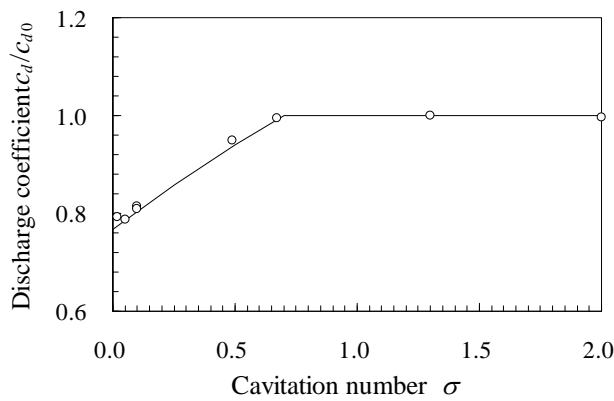


Fig. 5 Variation of discharge coefficient

decrease of cavitation number. As shown in the figure, cavitation bubbles caused in the jet flow downstream along the shear layer surrounding the jet.

Figure 5 shows the value of discharge coefficient evaluated under different cavitation conditions, where the vertical axis is normalized by the discharge coefficient  $c_{d0}$  of no-cavitating jet. The circles indicate computational results obtained by present method and the solid line refers to Nurick's experimental data [12]. The figure demonstrates that the computational results agree to the experimental data acceptably. Although much more detailed investigations are further required, the reliability of present methods is confirmed in a certain extent. The result demonstrates that the discharge coefficient decreases under the effect of cavitation. When the cavitation number  $\sigma = 0.1$ , the discharge coefficient decreases to 83% approximately compared to the case of no-cavitating flow.

#### 4. CONCLUSION

A practical compressible mixture flow method is developed for the computation of high Reynolds number turbulent cavitating flow by coupling a simplified estimation of bubble cavitation and the compressible mixture flow computation procedure. The method has applied to water jets issuing from a submerged orifice nozzle to explore the structure of high-speed turbulent cavitating flow and the reliability of flow computation is confirmed by comparison with experimental data.

The results demonstrate that (1) cavitation takes place initially at the entrance of orifice when the cavitation number is decrease to a certain critical value and cavitation bubbles mainly concentrate in the shear between the jet and surrounding water. (2) The intensity of cavitation denoted by the maximum value of gas volume fraction and the area of strong cavitation increases with the decrease of cavitation number. (3) Under the effect of cavitation bubbles the discharge coefficient of orifice decreases obviously compared to the case of no-cavitating jet.

#### ACKNOWLEDGMENTS

This work was supported by the Japan Society for the Promotion of science, Grant-in-Aid for Scientific Research (C) (No. 22560177).

#### REFERENCES

- [1] Soyama, H. et al. High-speed observation of ultrahigh-speed submerged water jets, *Experimental Thermal and Fluid Science*, Vol.12 (1996), pp.411-416.
- [2] Foldyna, J., Sitek, L., Svehla, B. and Svehla, S., Utilization of ultrasound to enhance high-speed water jet effects, *Ultrasonics Sonochemistry*, Vol.11 (2004), pp.131-137.
- [3] Wang G. et al., Dynamics of attached turbulent cavitating flows, *Progress in Aerospace Science*, Vol.37 (2001), pp.551-581.
- [4] Delale, C. F, Okita, K., and Matsumoto, Y., Steady-state cavitating nozzle flows with nucleation, *J. Fluids Eng.*, Vol.127 (2005), pp.770-777.
- [5] Kubota, A., Kato, H. and Yamaguti, H., A new modeling of cavitating flow: A numerical study of unsteady cavitation on a hydrofoil section, *J. Fluid Mech.*, Vol.240 (1992), pp.59-96.
- [6] Iga, Y. et al., Numerical study of sheet cavitation breakoff phenomenon on a cascade hydrofoil, *J. Fluids Eng.*, Vol.125 (2003), pp.643-651.
- [7] Peng, G., Fujikawa, S., Ishizuka, M. and Hayama, S., Numerical simulation of submerged water jet by an improved CIP-CUP method, *Computational Fluid Dynamics J.*, Vol.11 (2002), pp.27-34.
- [8] Beattie, D. and Whally, P., A simple two-phase frictional pressure drop calculation method, *Int. J. Multiphase Flow*, Vol.8 (1982), pp.83-87.
- [9] Yabe, T. and Aoki, T., A universal solver for hyperbolic equations by cubic-polynomial interpolation, *Computer Physics Communications*, Vol.66, (1991), 219-242.
- [10] Peng, G., Egashira, R., Yano, T. and Fujikawa, S., A pressure-based two-phase flow method for computation of bubble cavitation flows, Proc. 5th Joint ASME/JSME Fluids Eng. Conf., San Diego, USA, July 30–Aug.2, 2007, Paper No. FEDSM2007-37420.
- [11] Peng, G., Ishizuka, M. and Hayama, S., An improved CIP-CUP method for submerged water jet flow simulation, *JSME Int. J. (B): Fluids and Thermal Eng.*, Vol.44, No.4 (2001), pp.497-504.
- [12] Nurick, W. H., Orifice cavitation and its effect on spray mixing, *J. Fluids Eng.*, Vol.98 (1976), pp.681-687.



## Droplet Impact vs. Cavitation Erosion

T. Keil\*, P. F. Pelz, J. Kadavelil  
Technische Universität Darmstadt  
Chair of Fluid Systems Technology  
Magdalenenstraße 4, 64289 Darmstadt  
Germany

J. Necker\*, W. Moser, D. Christ  
Voith Hydro Holding GmbH & Co.KG  
Alexanderstraße 11, 89522 Heidenheim  
Germany

[thomas.keil@fst.tu-darmstadt.de](mailto:thomas.keil@fst.tu-darmstadt.de), [Joerg.necker@voith.com](mailto:Joerg.necker@voith.com)

### ABSTRACT

The quantification of the damage potential - aggressiveness - of imploding cavitation bubbles is of high importance for the economical use of low head water turbines, i.e. Kaplan-type turbines. For this kind of turbines a certain amount of cavitation is normally allowed even in the designed operating range to avoid costly deep settings.

The amount of admissible cavitation is governed among others by the requirement that no cavitation damage occurs in the machine. This requirement is strongly linked to the necessity to quantify the aggressiveness of the cavitation.

The common model test performed on a homologous model of the water turbine is an important mosaic for this quantification. Combined with the experience of prototype machines a fairly accurate decision on the admissible cavitation can be made. However, during this homologous test no erosion is seen in the model machine.

Input on the material resistance is acquainted at Voith by a droplet impact test rig. A water jet is stroken by a specimen causing damage on its surface. The macroscopic structure of the damage looks similar to a surface attacked by cavitation. Based on these experiments, relative statements on the material resistance can be done, such as: "Material A more resistant than Material B".

To extend the information content of the droplet impact test rig and to link the test rig parameters to cavitation parameters a specimen exposed to the water jet is analyzed at the Technische Universität Darmstadt using the 2-D pit-count method as well as a white-light-interferometer. The size of the impacts is analyzed in the very early stage of the surface destruction when no mass erosion has taken place yet (incubation time range).

A second set of specimen is exposed to cavitation in a test rig situated at the Chair of Fluid Systems Technology (FST). The specimen of the two test rigs show similar damage appearances with respect to the early and advanced incubation time period where displacements of grains in the material structure take place.

This paper describes the used test rigs, the pit-count analysis and the obtained results of the correlation between the droplet impact test rig and the cavitation test rig of FST.

To compare different erosion tests a dimensionless deformation energy  $\Pi_{D,C}$  is introduced. For the droplet test it is 2 to 3 orders of magnitude larger than for the cavitation tests done at TU Darmstadt.

On the other side a dimensionless cavitation erosion rate  $K$  is defined. The relation between  $\Pi_{D,C}$  and  $K$  as well as the dependency of both quantities on material properties is still ongoing research work.

### NOMENCLATURE

letter		
$E_{D,C}$	energy	$ML^2T^{-2}$
$E_o$	threshold energy	$ML^2T^{-2}$
$E$	elastic modulus	$ML^{-2}T^{-1}$
$d$	diameter	$L$
$f$	damage frequency	$T^{-1}$
$G$	elastic shear modulus	$MT^{-2}L^{-1}$
$h_i$	pit depth	$L$
$K$	cavitation rate	-
$L, l$	length	$L$
$p$	pressure	$ML^{-1}T^{-2}$
$R$	radius	$L$
$Re$	Reynolds number	-
$T$	exposure time	$T$
$V$	plastic deformation	$V$
$\Pi$	non-dim. energy	-
$\sigma$	cavitation number	-
$\rho$	density	$ML^{-3}$
$\square$	yield stress	$MT^{-2}L^{-1}$
$\nu$	kinematic viscosity	$L^2T^{-1}$
$\Omega$	angular velocity	$T^{-1}$

### indices

c	cavitation mill
d	droplet impact
m	material

## 1. INTRODUCTION

Imploding cavitation bubbles can damage relevant components in hydraulic systems. The vapor bubbles are caused by the decrease of the hydrodynamic pressure below a critical pressure of the fluid which is a function of the vapor pressure, the turbulence and the cavitation nuclei. When the bubble grow to a critical size (given by the so called Blake diameter) they become unstable and consequently implode which cause, in the vicinity of walls, pressure peaks up to several hundreds of MPa.

One aspect of the operating limits of a hydraulic system like displacement or centrifugal pump, flow valve or water turbine is the intensity of cavitation. A possibility to quantify the intensity is to use soft metal coating in homologous model tests. The considered geometry is coated by a soft metal like copper. The coating is exposed to the collapsing cavitation bubbles until plastic deformations (pits) or material loss can be detected. Using this method the location and the intensity of the cavitation damage can be analyzed. However, these tests are time consuming. For special purposes like measuring the material dependent fatigue and erosion curves, experiments are performed in which the surface degradation is usually faster than in the homologous model test. Beside the speed up, these experiments often allow a better visual access and an easier interpretation of the cavitation damage. The Chair of Fluid System Technology has a so-called "cavitation mill" for these purposes.

Another method to produce similar damage appearance like cavitation erosion is the droplet impact test. A fast rotating rod with attached material samples strikes through a water jet which flows in the direction of the rotation axis. The sample surface is degraded by the impact of the water jet.

In the context of a cooperation between Voith and the Chair of Fluid Systems Technology of TU Darmstadt samples of copper and of stainless steel are investigated in the droplet impact test rig and in the cavitation mill. Similar appearance of damage is adjusted to transfer the cavitation parameters to the droplet test rig. The damage is analyzed by the pit-count system of FST and white light-interferometer pictures of the surfaces are taken. The aim of the study is to find a correlation between the droplet impact and the cavitation mill.

## 2. EXPERIMENTAL SET UP

### Cavitation Mill

Consisting of a rotating disc in a closed case filled with water the fluid is set in movement with an angular velocity  $\Omega$ .

Four bore holes at the front side of the disc lead to a reduction of the local pressure in the cavities. The pressure is below the critical pressure of the fluid and four aggressive cavitation zones moving with the rotating disc are generated. The collapse of the cavitation zone takes place on the material surface of the samples which are arranged on the circumference in removable, stationary bridges close to the rotating disc. Altogether there are six of these bridges, but only four of them are used as sample holder. To ensure the same flow conditions in each experiment the specimen which is positioned in the marked area of Fig. 1 is used.

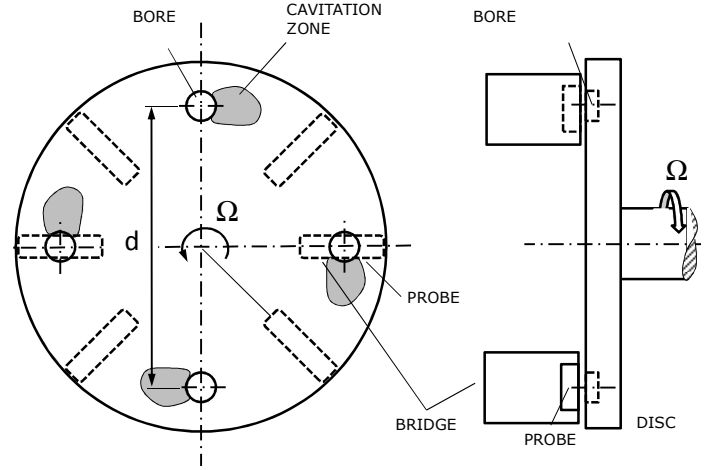


**Fig. 1:** Cavitation mill of the Chair of Fluid Systems Technology.

After the collapse onto the previous bridge the cavitation zone regenerates itself. By varying the motor speed the Reynolds number of the flow can be changed

$$Re := \frac{d^2 \Omega}{2\nu}, \quad (1)$$

where  $d$  is the distance between two opposite holes on the disc,  $\Omega$  is the angular velocity of the rotating disc and  $\nu$  the kinematic viscosity of water. The experiments were performed at a Reynolds number of  $Re = 11.5e6$ .

Independent of the Reynolds number is the cavitation number.

$$\sigma := \frac{p - p_v}{\frac{\rho}{2} \left( \frac{d}{2} \Omega \right)^2}. \quad (2)$$

$p$  is the system pressure,  $p_v$  the vapor pressure and  $\rho$  the water density. The cavitation number is controlled by the system pressure.

Fig. 2 shows the geometry of the specimens which are applied in the cavitation mill. The marked area on the surface is the range for the pit-count system. In addition, a smaller area shows the interested zone for scanning with a white-light-interferometer.

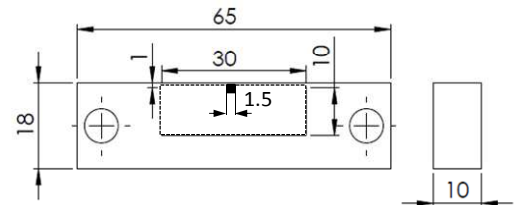


**Fig. 2:** Specimen for cavitation mill.

### Droplet Impact Test Rig

The droplet impact test rig consists of a rotating lever arm which rotates at a constant speed. To change the impact velocity the material specimen can be positioned at different radii.

During each revolution the specimens are hit by the water jet once. The speed of the water jet is controlled by a throttle. The embedded sketch shows the dimension of the specimen attached to the rotating lever arm.

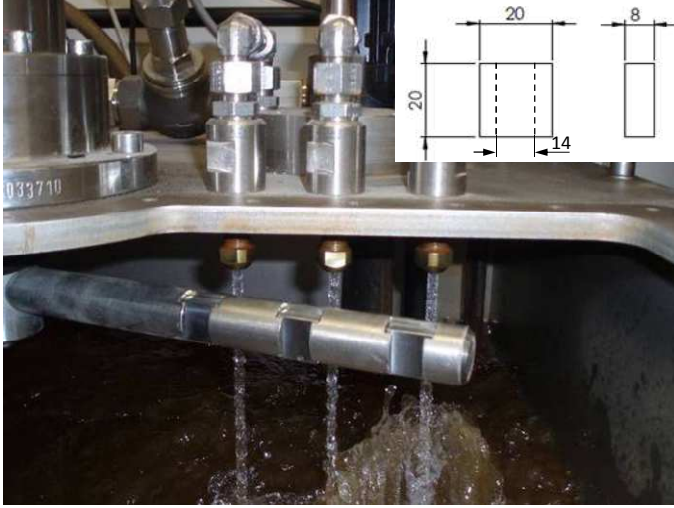


Fig. 3: Droplet impact test rig at Voith Hydro.

### Materials

Within our study copper and stainless steel 1.4313 specimens are tested.

### Cavitation and Cavitation Erosion

Different types of cavitation and different stages of the cavitation damage process can be distinguished. An overview about the main cavitation mechanism and their exposure time onto material surfaces is summarized and highlighted by Van Terwisga [1]. When the spherical cavitation bubble becomes unstable, it collapses and deforms to look like a donut. A microjet, a strong pressure wave towards the surface and high temperatures are observed for short durations which imply a significant load on a small area. Up to now it is unclear what the influence of the high temperature of the collapsing bubble is on the surface load.

Suppose the mean frequency of bubble cavitation is proportional to the rotating frequency times the number of specimen, and the exposure time is  $T$ , there will be  $\sim fT$  load cycles on the material surface. For quasi-stationary process conditions the fatigue process is divided in three stages:

#### 1. Incubation stage

In the early phase of exposure only plastic deformation occurs at the surface. In this period, no material loss is recorded, only small dents with different depths (and diameters) in the surface ("pits") can be analyzed. Empirical correlations between pit size, material and energy applied to the surface can be used in the early

stage of this phase when still no overlapping of the pits has happened or no boundaries of the grains are visible.

#### 2. Transitional stage

Following the incubation period, cracks along the grain-boundaries indicate the beginning of the second phase in which material is eroded from the surface. During this phase the ratio of mass-loss and time is progressive, i.e. the size of the pieces torn off the surface increases with time.

#### 3. Mass loss stage

Subsequently a third phase with a constant ratio of mass-loss and time can be distinguished. The size of the pieces torn off the surface stays approximately the same.

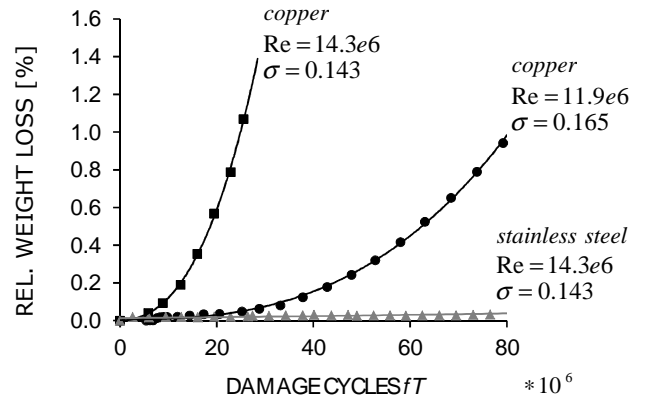


Fig. 4: Material loss diagram of copper and stainless steel.

Fig. 4 shows the mass loss plotted against the damage cycles for stainless steel and copper for constant process conditions. While copper is already in the transition or even the mass loss stage, no mass loss can be registered for the stainless steel ("incubation stage").

In analogy to a first order chemical reaction a first order time evolution model is proposed for cavitation erosion

$$\kappa(\sigma, Re, \Pi_{m1}, \Pi_{m2}, \dots) = -\frac{1}{V} \frac{dV}{d(tf)} \quad (3)$$

where  $V$  is the sum of plastic deformed and eroded material volume. The evolution equation (3) is at the same time a definition of a dimensionless cavitation erosion rate which has to be equivalent to the later introduced dimensionless deformation energy  $\Pi \sim K$ . Evaluating equation (3) the total volume change of a device is

$$\ln(V(0)/V) = \int_0^{fT} \kappa(\sigma(\Omega t), Re(\Omega t), \Pi_{m1}, \Pi_{m2}, \dots) d(tf) \quad (4)$$

The history of the process conditions is represented in equation (4) by the cavitation and the Reynolds number.

The dimensionless cavitation erosion rate is a function of dimensionless quantities describing the cavitating flow, here



cavitation and Reynolds number, and further dimensionless quantities describing the solid material. Up to now it is still an open question which dimensionless material quantities describe properly the erosion resistance of different materials.

For general visco-plastic-elastic material behavior the ratio of the square of the material viscosity to the material density  $\eta_m^2/\rho_m$  is a force typical for a material. It has to be made dimensionless with the yield stress  $\vartheta$  and a material typical length  $l_m$  (e. g. grain diameter). A second dimensionless quantity is certainly the ratio of the yield stress and the elastic shear modulus of the material  $G$ :

$$\Pi_{m1} = \frac{\vartheta l_m^2}{\eta_m^2/\rho_m}, \quad \Pi_{m2} = \frac{\vartheta}{G}, \quad \Pi_{m3} = \frac{l_m}{l_m}, \dots \quad (5)$$

The investigation carried out at the droplet impact test rig and the cavitation mill is specifically focused on the incubation stage. This allows a more precise quantification of the deformed surface and a better comparison of the damage mechanisms. Especially the correlation between pit size and applied energy is most accurate if single pits without overlapping can be analyzed.

### Water Impact Erosion

When the material surface of the specimen strikes through the water jet, the jet is atomized into small droplets in a very short time. The kinetic energy is introduced into the material surface, resulting in a plastic deformation of the material. Fig. 5 shows the impact of the specimen in a sequence of pictures recorded by a high-speed camera. The jet can be seen at  $t = 0$ . It flows from the top to the bottom. The specimen moves from the back towards the front. The impact velocity is approximately  $u = 70 \text{ m/sec}$ .

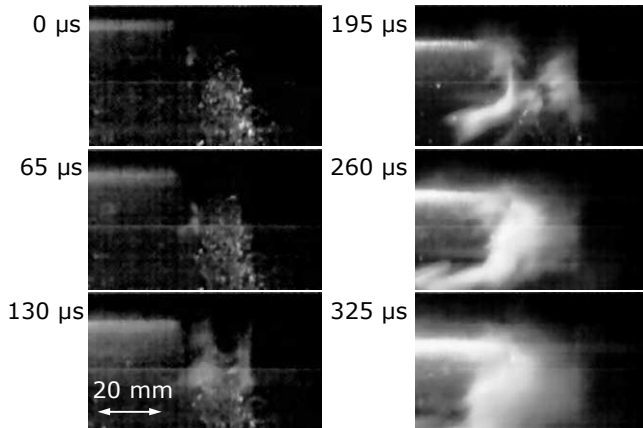


**Fig. 5:** High speed visualisation of the atomization of the water jet into water droplets.

The specimen hits the jet after  $65 \mu\text{s}$  elapsed. The atomization of the jet is continued till the specimen is moved out of the jet and the jet can recover again.

Even with the high performance high-speed camera a more detailed view of the impact is hidden behind a droplet curtain. If any cavitation is involved in the atomization and, if yes, the

extent of it, has not been sufficiently clarified yet. Knezevic [7] describes in the center of the droplet impact a very low pressure zone, where cavitation could be occurred. The low pressure in the droplets may come from a reflected shock wave also described by Farhat et al [12].

The process of a droplet impact describes Ni [4]. He divides the droplet impact into five stages. Upon impact, a part of the energy of the water jet, given by the kinetic energy of the jet and its surface energy and a part of the energy of the specimen, given by its kinetic energy are converted into the deformation of the specimen and in the atomization of the jet. In addition, part of the energy leads to a deceleration of the rotating arm and the heating of the water.

In the early stage of the tests, the damaged surface shows dents of different depths. The shape of the damage implies that the main load of the surface comes from droplets generated during the atomization of the jet. Pictures of the surface at different times during the incubation period are shown in Fig. 6. An analytical calculation of the energy needed for the deformation of the surface is difficult since e.g. no spectrum of the droplet sizes is available or even cavitation may contribute to the load of the surface.

Exceeding the incubation stage and entering the mass loss stages show the large aggressiveness of the droplet tests in general and of the test rig specifically. Only after a relatively small number of impacts in the order of  $10^6$  a stainless steel surface is heavily damaged.

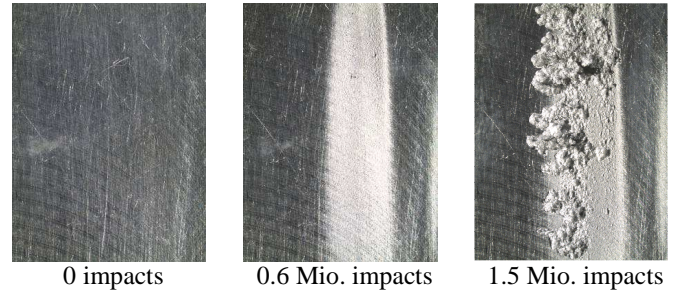


**Fig. 6:** Surface of stainless steel 1.4313 in droplet test rig.

This high potential of droplets to damage surfaces is in accordance with several prototype applications in different fields of prototype applications like in Pelton buckets or the low-pressure stage of a steam turbine. A quantification of the material loss of a stainless steel sample for the droplet impact test rig is given in Fig. 7.

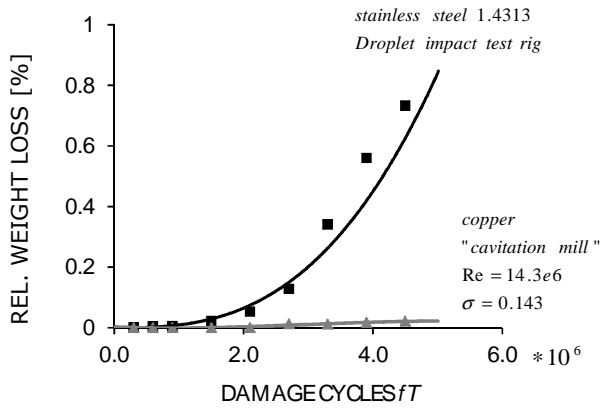


**Fig. 7:** Mass loss in the droplet test rig of *stainless steel* vs. mass loss of *copper* in the cavitation mill at FST.

It is interesting to see that the most aggressive operation of the cavitation mill shown in Fig. 7 is much less aggressive than the one investigated in the droplet test rig. Even with the - compared to copper - much more resistant stainless steel much larger mass-loss rates are achieved for equal damage cycles. This allows to obtain results from the droplet test rig for relative tests (Material “A” more resistant than material “B”) in very short durations.

For the presented study this large aggressiveness of the droplet test rig made it challenging to stop early enough the destruction of the surface before the displacement of the grains in the material already started. This requirement is important for an accurate application of the pit count method.

## EXPERIMENTAL RESULTS

The droplet impact tests were conducted with three copper and three stainless steel samples 1.4313. The number of damage cycles for one copper and one steel sample are 500, 5000 and 10000. The damaged specimen surfaces are shown in Fig. 8 scanned with the pit-count system at the Chair of Fluid Systems Technology. As expected, the copper specimens show more pronounced damage than the stainless steel during the same surface load.

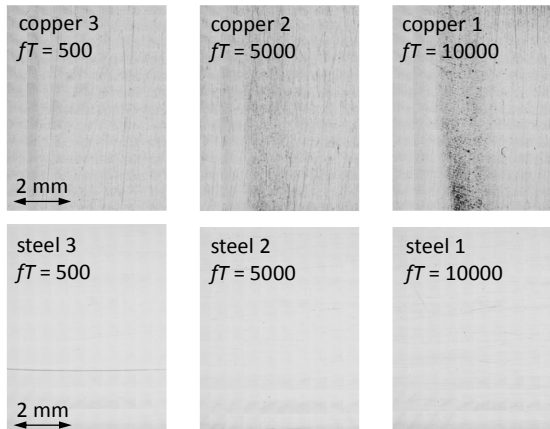


**Fig. 8:** Scanned material surfaces of copper and stainless steel.

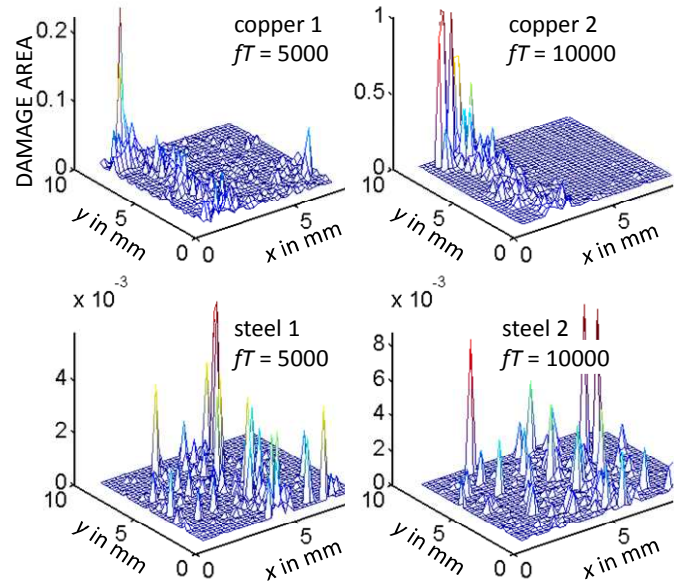


**Fig. 9:** Pit-count scanned copper and steel surface. Erosion by droplet impact.

The largest deformation occurs at the location at which the water jet touches the surface and the jet is atomized. The damaged area is separated sharply from the undamaged area.

The acting deformation on the surface leads to a shift of the dislocations in the material. For longer exposure times like 5000 and 10000 cycles of impacts, displacements of grains on the copper surface are clearly visible. It should be mentioned that still no mass loss is detected (incubation stage). Although the pit-count system has been developed for damages during the incubation period [11] [13], displacements of grains that deviate from the round shape of a pit, cannot be scanned.

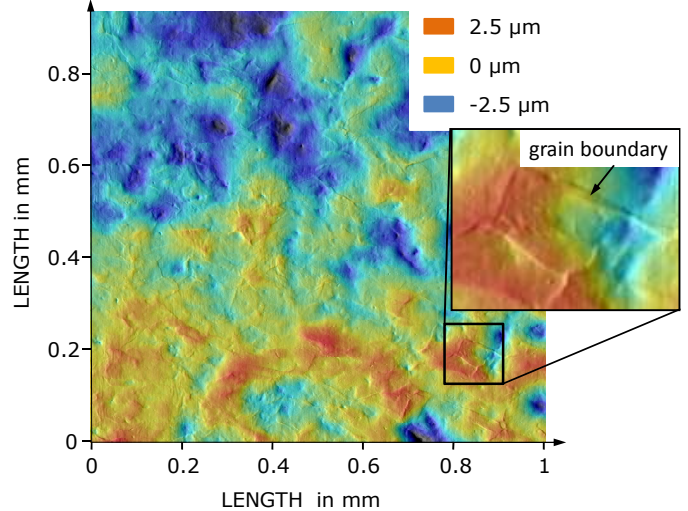


**Fig. 10:** White light interferometer shows a displacement of grain. Final stadium of the incubation period.

At 500 cycles of impacts, neither the copper sample nor the steel sample shows the shift of the grains in the surface. The surfaces of these samples show plastic deformation similar to

pits originated by bubble collapses near the surface. Following Lohrborg [11], the integral deformation energy associated with the counted and measured pits is given by

$$E = \vartheta L_m^3 \sum_i \left( 1 + \frac{R_i}{l_m} \right)^3. \quad (6)$$

Here  $\vartheta L_m^3$  is a material typical energy,  $L_m$  is a second material typical length in addition to the prior defined length  $l_m$ , and  $R_i$  is the detected pit radius. The total deformation energy is made dimensionless, with the water density  $\rho$ , the typical length of the arm  $d/2$  and the mass specific kinetic energy  $(d\Omega/2)^2/2$ :

$$\Pi_{D,C} := \frac{64}{fT} \frac{E_{D,C}}{d^5 \rho \Omega^2}. \quad (7)$$

$fT$  describes the number of damage cycles.

### Cavitation Tests

With the same material the cavitation test were performed. Two specimens were damaged at an operation point with moderate cavitation aggressiveness in the cavitation mill. The cavitation exposure times are 9 and 19 hours at a Reynolds number of  $11e6$  and a cavitation number of  $0.2184$ .

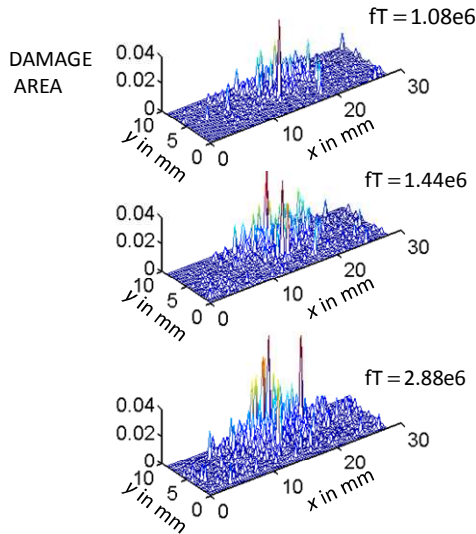


**Fig. 11:** Pit-count scanned copper surface. Erosion by collapsing bubbles

Compared to the droplet impact test, the damage focuses around the sample center at the upper edge. The damage intensity decreases radially outward, but not as abruptly as in the droplet impact test.

The deformation energy is determined using the empirical relation (6) together with the definition (7) for the dimensionless deformation energy per cycle  $\Pi_C$ . Again it is assumed that the deformation energy per cycle is proportional to the

dimensionless cavitation rate given by (3) which is in our future research focus at TU Darmstadt.

The following diagram Fig. 12 shows the dimensionless damage energy as a function of the cycle number during the first 9 hours of specimen 1 and 19 hours of specimen 2 in the incubation time. Both samples are made out of the same copper material, and they were damaged at same operating condition in the cavitation mill. The reproducibility of the measurement method is also shown in Fig. 12. Because of overlapping pits the damage of a longer exposure time is not possible to analyze with the pit-count method. The graphs have a slight increase for the first cycles, which is probably due to the fatigue of the material surface. This fatigue process may be not captured at the droplet test rig in the presented study due to the large aggressiveness of the destruction.

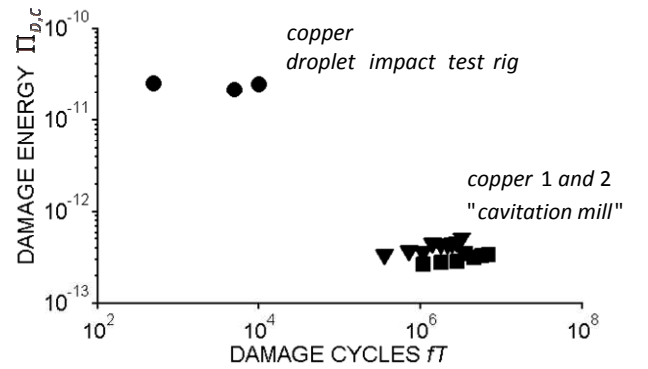


**Fig. 12:** Damage energy of cavitation mill and droplet impact test rig.

Two conclusions can be drawn when comparing the droplet impact test with the cavitation test in Fig. 12:

1. The dimensionless damage energy defined by equation (7) is only slightly depending on the number of damage cycles. Thus, (7) serves as a good measure to analyze the droplet impact and the cavitation test.
2. The damage energy of the droplet impact is around 2 to 3 orders of magnitude larger in comparison to the cavitation erosion for the considered operating point.

### Scaling of droplet impact to cavitation tests

Comparing the damage energy per cycle of the droplet impact test with the cavitation test

$$\frac{E_D(fT)_C}{E_C(fT)_D}, \quad (8)$$

the droplet impact applies more than 500 times more energy to the surface than the cavitation in the cavitation mill at the considered operation point.

Additionally to the pit-count, the damaged surfaces of the two test rigs are scanned by a white-light-interferometer. The white-light-interferometer scans the surface in 3 dimensions and hence a much more detailed topology of the surface is gained. In the following Fig. 13 a pit-count- and a white-light-interferometer-scan are compared. Because of the high precision



of the white light-interferometer in the range of nanometer only a small area of 1.5 mm x 1.5 mm is scanned.

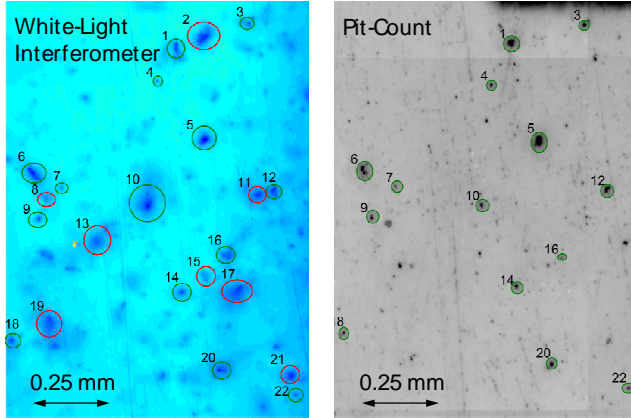


**Fig. 13:** Compare of pit-count and white light interferometer of a cavitation specimen.

The highlighted and labeled pits in the right and left picture are detected pits by the pit-count-method. Red circles indicate undetected deformations visible with the white light interferometer. Unmarked spots only look like pits, but are failures of the surface already existing before the cavitation test were performed. Fig. 14 shows the number of detected pits by the white-light-interferometer, the pits detected by the pit-count method and the difference of both which is the pits undetected by the pit-count. The ratio  $R_i/h_i$  of pit radius  $R_i$  and pit depth  $h_i$  is categorized in size classes. In principle it can be concluded that shallow pits with a large radius and a small depth cannot be identified by the pit-count because of the large opening angle of the pits. On the other hand, deep pits with small radius are detected without failure since the contrast of pits and surface is larger.

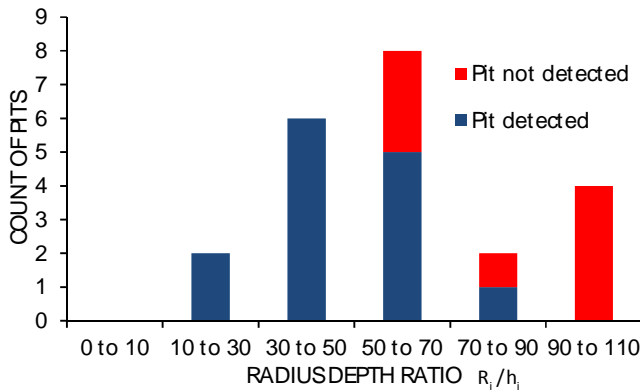


**Fig. 14:** Detected and undetected pits with pit-count.

Although more damage, i.e. more, deeper and larger pits could be detected with increasing number of cycles, no displacements of grains were determined like in the droplet impact tests for the operation with moderate cavitation. Therefore, another set of specimen are tested at a more aggressive operating point with a Reynolds number of 15.5e6 and a cavitation number of 0.112.

After 2.34e6 damage cycles the displacement of grains on the material surface were detected. The following pictures show the beginning of the displacement and the grains and the grain boundaries after a 4.68e6 damage cycles. As a result, the same material fatigue as with the droplet test rig could be achieved by the cavitation mill.

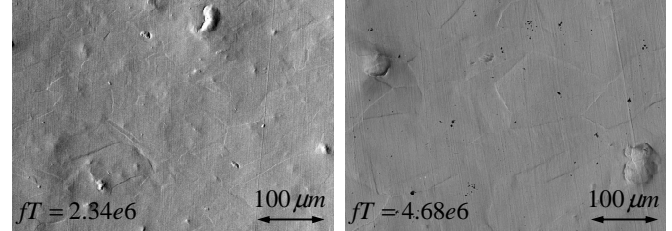


**Fig. 15:** Displacements of copper gains for 2.34e6 and 4.68e6 damage cycles.

## CONCLUSION

Copper and stainless steel are exposed to two types of surface loading in two different test rigs: the droplet impact test rig of Voith Hydro and the cavitation mill of the FST, TU Darmstadt. The surfaces of the specimens are analyzed with the pit-count method of the FST and a topology scan obtained by a white-light interferometer.

The microscopic view of the damage of the two test rigs look similar and the same processes can be detected during the incubation stage: local, plastic deformation causing pits in the surface followed by the displacement of the metal grains. This is the beginning for initial cracks and the subsequently following erosion with material removal. All phases could be reproduced by both test rigs.

An evolution model was proposed for the dimensionless erosion rate, which correlates the dimensionless pit energy.

The visual similarity of the damaged surfaces justifies the usage of the pit-count method to analyze the energy applied to each surface even though the root cause for the damage is different. The cavitation mill exposes the specimen to the collapse of cavitation while in the droplet test rig a water jet is atomized and a mixture of droplets and water slag (and maybe even cavitation) is causing the high load to the surface.

The dimensionless deformation energy by the droplet impact test rig for the considered operating point is more than 500 times larger than the cavitation mill. However, because of this large aggressiveness, a relatively small number of impacts already lead to the displacement of the metal grains that cannot be analyzed anymore. As a consequence the cavitation mill is more suitable for the detailed analysis of the incubation stage while relative material tests are faster done with the droplet impact tests.

A comparison of the white-light-interferometer and the pit-count method shows that the pit-count method works best for deep pits with a small radius. Beginning inaccuracy of the pit-count due to pits that are not detected anymore could be observed at radius - depth ratios of 50.

## REFERENCES

- [1] Van Terwisga, Fitzsimmons, P.A., Zirru, L., Foeth, E.J., *Cavitation Erosion – A review of physical mechanisms and erosion risk models*, Proc CAV2009 – 7th International Symposium on Cavitation, Ann Arbor, 2009
- [2] Fortes Patella, R., Reboud, J.L., *Interaction between pressure waves and spherical cavitation bubbles: Discussion about cavitation erosion mechanism*, Proc. Of the 2000 ASME Fluids Engineering Summer Conference, Boston, Massachusetts, 2000
- [3] Fortes Patella, R., Challier, G., Reboud, J.L., Archer, A., *Cavitation erosion mechanism: numerical simulations of the interaction between pressure waves and solid boundaries*, Proc. CAV2001 International Symposium on Cavitation, Pasadena, 2001
- [4] Ni, J., Guo, Q., Zhou, Z., Wang, F., *Submodel for Predicting Slag Deposition Formation in Slagging Gasification Systems*, Energy Fuels 2011, 1004-1009
- [5] Castrejon-Pita, J.R., Betton, E.S., Kubiak, K.J., Wilson, M.C.T., Hutchings, I.M., *The dynamics of the impact and coalescence of droplets on a solid surface*, BIOMICROFLUIDICS 5, 014112, 2011
- [6] Lunkad, S.F., Buwa, V.V., Nigam, K.D.P., *Numerical simulations of impact and spreading on horizontal and inclined surfaces*, Chemical Engineering Science 62 (2007), 7214-7224, 2007
- [7] Knezević, K.H., *High-Velocity Impact of a Liquid on a Rigid Surface: The Effect of Liquid Compressibility*, Dissertation, Swiss Federal Institute of Technology Zurich, Zurich, 2002
- [8] Field J.E., Dear, J.P., Ogren, J.E., *The effects of target compliance on liquid drop impact*, J. Appl. Phys. 65 (2), 15 January 1989
- [9] Qin, C.P., Zheng, Y.G., Wei, R., *Cavitation erosion of nanocomposite Ti-Si-C-N and Ti/Ti-Si-C-N coatings deposited on 2Cr13 stainless steel using a Plasma Enhanced Magnetron Sputtering process*, Surface & Coatings Technology 204 (2010) 3530-3538
- [10] Mettin, R., Luther, S., Lindau, O., Koch, P. Lauterborn, W., *Investigation of Cavitation Bubble Dynamics by Means of Fast Cinematography*, The International Conference on Multiphase Systems Ufa, RUSSIA, June 15 17, 2000, ICMS 2000
- [11] Lohrberg, H., *Messung und aktive Kontrolle der erosiven Aggressivität der Kavitation in Turbomaschinen*, Fortschritts-Bericht VDI Reihe 8 Nr. 942 ISBN 3-18-394208-5, 2001
- [12] Farhat, M. *The Swiss Army's Shot at Science: High-Speed Impact of a Solid on a Water Jet*, Lay Language Paper of 62nd APS DFD Annual Meeting, 2009
- [13] Keil, T., Cordes, U., Pelz, P.F., Ludwig, G., *On the Transient Behavior of Cloud Cavitation and the Erosion in a Nozzle Flow*, Warwick IMRC, 3rd International Cavitation Forum 2011



## **Numerical Studies on Streaky Pattern Caused by Boundary-Layer Transition**

Ting Chen

University of Warwick

S. C. Li\*

University of Warwick

E-mail: S.Li@warwick.ac.uk

### **ABSTRACT**

In 2006, Li [1] has proposed a mechanism of cavitation inception from the boundary-layer streak breakdown for interpreting a strange pattern of damage occurring on the guide vane of the Three Gorges turbines. Since then the envisaged cavitation inception triggering process has been verified through numerical and experimental approaches (e.g. Ref. [2]).

A further step to verify the correlation of the span-wise regularity of the streaks with the damage strips spacing as proposed in [1] is essential. In this paper, we proposed a novel approach by utilizing a numerically calculated turbulence intermittency ( $\gamma$ ) for visualizing the span-wise regularity of the boundary-layer streaks. This numerical approach is firstly validated by comparing with the experimentally measured results on the NACA 16012 by Franc [7] and subsequently used to verify the parametrical evidence proposed in [1] that the coincidence of the span-wise regularity of the damage-strip with that of the streak breakdown is true.

### **NOMENCLATURE**

$Re_{\theta t}$  = momentum-thickness Reynolds number

$\widetilde{Re}_{\theta t}$  = local transition onset momentum-thickness Reynolds number

$T_u$  = turbulence intensity,  $100(2k/3)^{1/2}/U$

$\gamma$  = intermittency

$U$  = local velocity

$\mu$  = molecular viscosity

$\mu_t$  = eddy viscosity

$\mu_\tau$  = friction velocity

$y$  = distance to nearest wall

$y^+$  = distance in wall coordinates,  $\rho y \mu_\tau / \mu$

$x/C$  = axial distance over axial chord

$\omega$  = specific turbulence dissipation rate

$\rho$  = density

$\delta^*$  = the displacement thickness

$\lambda^*$  = the wavelength of Klebanoff wave

$x_{onset}$  = the location of calculated transition point

### **1. INTRODUCTION**

Many implications (e.g. Refs. [3, 7]) show that boundary-layer transition has strong influences on the onset of cavitation. However, it was until 2006 that an envisaged mechanism has been proposed [1] that was for the first time clearly relating the cavitation inception to the K-mode streak breakdown in the boundary layer with evidence gathering from damaged Three Gorges turbines. That is a strange damage on the lower surface of guide vanes of Three Gorges turbines. Having done a multidisciplinary analysis [1], all evidences are supportive to the hypothesis that this is a new type of cavitation triggered by the breakdown of boundary-layer streaks. Among them is the span-wise spacing of the damage strips complying well with the estimation of the span-wise distribution of K-mode streaks breakdown and turbulence production. For details, see Ref. [1]. To verify this piece of evidences, a numerical approach for simulating transition has been applied here for visualizing the formation of the boundary-layer streaks and their breakdown through the calculated values of the turbulence intermittency  $\gamma$ .

Transition prediction is an undoubtedly important issue, however, is not included in the majority of today's engineering CFD simulations because of a variety of influences limiting the precise prediction of the transition Reynolds number, such as free-stream turbulence and surface roughness. Currently, most industrial transition modelling methods are mainly based on two concepts [4]. The first is the use of low-Reynolds number turbulence models, where the wall damping functions of the underlying turbulence model trigger the transition onset. The second approach is the use of experimental correlations which usually relate the turbulence intensity  $T_u$  in the freestream to the momentum-thickness Reynolds number  $Re_{\theta t}$  at transition onset (e.g. Abu-Ghannam and Shaw correlation [5]). A combination of newly developed correlation-based transition model by Menter et al. [6] and modern computational fluid dynamics (CFD) approaches provides an effective and convenient tool for predicting the transition process as long as appropriate correlations can be provided. The current correlations have been formulated to cover standard bypass transition as well as flows in low free-stream turbulence environments [4].

In this paper, we will use a new correlation-based transition model combined with SST turbulence model aiming at both validating the transition model and proving that piece of evidence about the span-wise regularity of damage strips with K-mode streaks. This work has been firstly carried out on NACA 16012 foil using the same boundary conditions as in

Franc's experimental investigation [7] for the purpose of verifying the numerical model. These calculations have been performed in parallel on the high-performance computers at the Cavitation Research Group of Warwick University.

## 2. NUMERICAL METHOD

The whole calculation field is modeled as 1600 mm long, 120 mm wide and 400 mm high. The symmetrical NACA 16012 foil is set in the middle, and its chord is 10 cm; its maximum thickness at the relative abscissa 0.5 is 12 mm. The free-stream velocity is 12 m/s and the angle of attack is varied from 2° to 5°. For verifying if this approach is capable of reliably capturing the influence of free-stream turbulence that affect transition, calculation results with different turbulence intensity values have been compared. However, for the conciseness, only the cases with turbulence intensity of 0.165% at the inlet condition (except Fig. 6) are reported here.

### 2.1 Model Formulation

The transport equation for the intermittency  $\gamma$ , which can be used to trigger transition locally, is coupled with the shear stress transport (SST) turbulence model, turning on the production term of the turbulent kinetic energy downstream of the transition point [4].

The transport equation for the intermittency  $\gamma$  is:

$$\frac{\partial(\rho\gamma)}{\partial t} + \frac{\partial(\rho U_j \gamma)}{\partial x_j} = P_{\gamma_1} - E_{\gamma_1} + P_{\gamma_2} - E_{\gamma_2} + \frac{\partial}{\partial x_j} \left[ \left( \mu + \frac{\mu_t}{\sigma_f} \right) \frac{\partial \gamma}{\partial x_j} \right]$$

In addition, another transport equation is solved in terms of the transition onset momentum-thickness Reynolds number  $\tilde{Re}_{\theta t}$  for capturing the nonlocal influence of the turbulence intensity, which changes due to the decay of the turbulence kinetic energy in the free-stream, as well as due to changes in the free-stream velocity outside the boundary layer.

$$\frac{\partial(\rho \tilde{Re}_{\theta t})}{\partial t} + \frac{\partial(\rho U_j \tilde{Re}_{\theta t})}{\partial x_j} = P_{\theta t} + \frac{\partial}{\partial x_j} \left[ \sigma_{\theta t} (\mu + \mu_t) \frac{\partial \tilde{Re}_{\theta t}}{\partial x_j} \right].$$

As the essential part of the model, this equation ties the empirical correlation to the onset criteria in the intermittency equation, applying for models used in general geometries and over multiple blades, without interaction from the user.

The transition model interacts with the turbulence model as follows:

$$\frac{\partial(\rho\gamma)}{\partial t} + \frac{\partial(\rho u_j \gamma)}{\partial x_j} = \tilde{P}_k - \tilde{D}_k + \frac{\partial}{\partial x_j} \left[ (\mu + \sigma_k \mu_t) \frac{\partial k}{\partial x_j} \right],$$

$$\begin{aligned} \frac{\partial(\rho\omega)}{\partial t} + \frac{\partial(\rho u_j \omega)}{\partial x_j} &= \alpha \frac{P_k}{v_t} - D_\omega + C d_\omega + \frac{\partial}{\partial x_j} \left[ (\mu + \sigma_k \mu_t) \frac{\partial k}{\partial x_j} \right]. \end{aligned}$$

SST model [8] is formulated as follows:

$$\begin{aligned} \frac{\partial(\rho k)}{\partial t} + \frac{\partial(\rho U_j k)}{\partial x_j} &= \tilde{P}_k - \beta^* \rho k \omega + \frac{\partial}{\partial x_j} \left[ (\mu + \sigma_k \mu_t) \frac{\partial k}{\partial x_j} \right], \\ \frac{\partial(\rho\omega)}{\partial t} + \frac{\partial(\rho u_j \omega)}{\partial x_j} &= \alpha \rho S^2 - \beta \rho \omega^2 + \frac{\partial}{\partial x_j} \left[ (\mu + \sigma_\omega \mu_t) \frac{\partial \omega}{\partial x_j} \right] \\ &\quad + 2(1 - F_1) \rho \sigma_{\omega 2} \frac{1}{\omega} \frac{\partial k}{\partial x_j} \frac{\partial \omega}{\partial x_j}. \end{aligned}$$

### 2.2 Mesh Requirements

The required near wall mesh spacing,  $\Delta y$ , in terms of Reynolds number, running length and a target value, depending on the flow type and the turbulence model in use. In order to capture the laminar and transitional boundary layers correctly, the grid must satisfy  $y^+ \approx 1$ . If the  $y^+$  is too large (i.e.  $> 5$ ), then the transition onset location moves upstream with increasing  $y^+$  [4]. All simulations have been performed with a bounded second-order upwind biased discretization for the mean flow, turbulence, and transition equations.

## 3. RESULTS

### 3.1 2D Results

Results from Franc's work [7]:

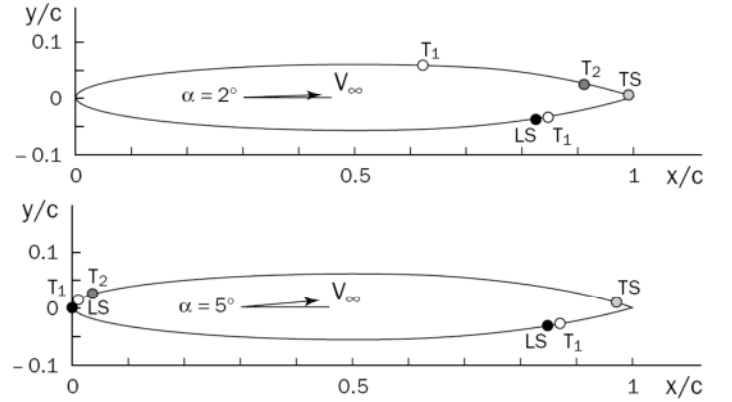
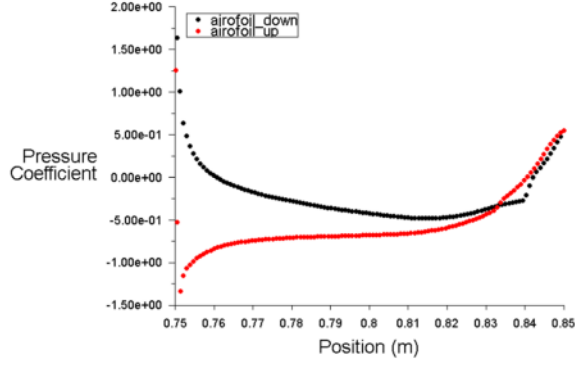


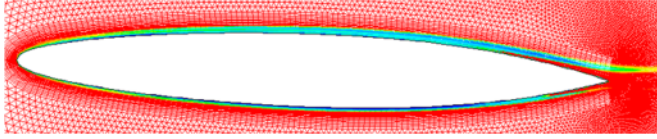
Fig 1. Boundary layer behavior on NACA16012 hydrofoil in non-cavitating conditions (chord length: 0.1 m, flow velocity: 12 m/s, turbulence intensity: 0.165%, attack angle:  $\alpha=2^\circ$  and  $5^\circ$ )

LS: laminar separation; T<sub>1</sub>: start of transition; T<sub>2</sub>: end of transition; TS: turbulent separation. Between T<sub>1</sub> and T<sub>2</sub> intermittency of the turbulence grows from zero to one. Thus, T<sub>2</sub> also refers to the beginning of the fully turbulent boundary layer flow [7].

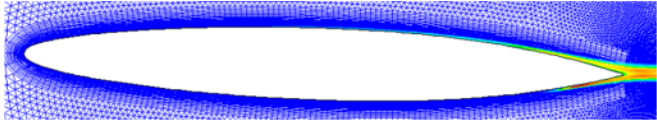
Figure 1 shows the results from Franc's experimental investigation [7] which provides a comparison for verifying our calculated results when the angle of attack is 2° and 5°. Geometrical dimensions, flow conditions and boundary conditions are all kept the same with Franc's experimental setup for comparability.



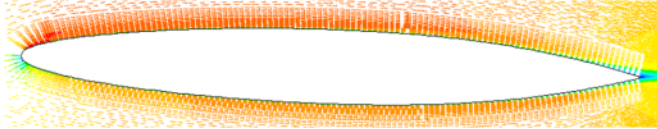
(a) pressure coefficient distribution



(b) intermittency distribution

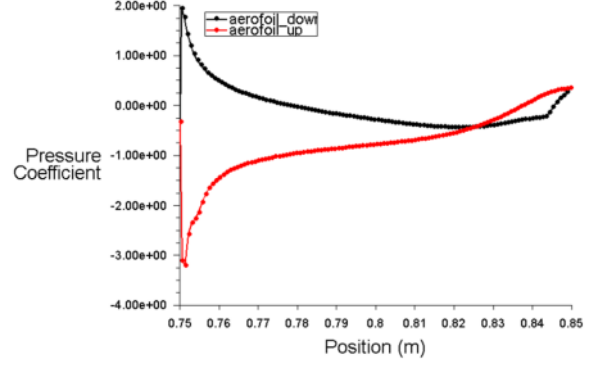


(c) turbulence intensity

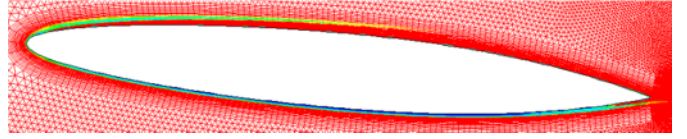


(d) velocity distribution

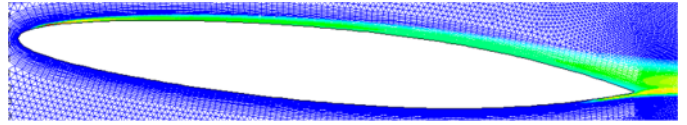
Fig 2. Calculated pressure coefficient distribution (a), intermittency distribution (b), turbulence intensity distribution (c) and velocity distribution (d) on NACA16012 foil ( $\alpha = 2^\circ$ )



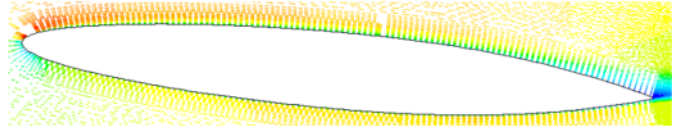
(a) pressure coefficient distribution



(b) intermittency distribution



(c) turbulence intensity



(d) velocity distribution

Fig 3. Calculated pressure coefficient distribution (a), intermittency distribution (b), turbulence intensity distribution (c) and velocity distribution (d) on NACA16012 foil ( $\alpha = 5^\circ$ )

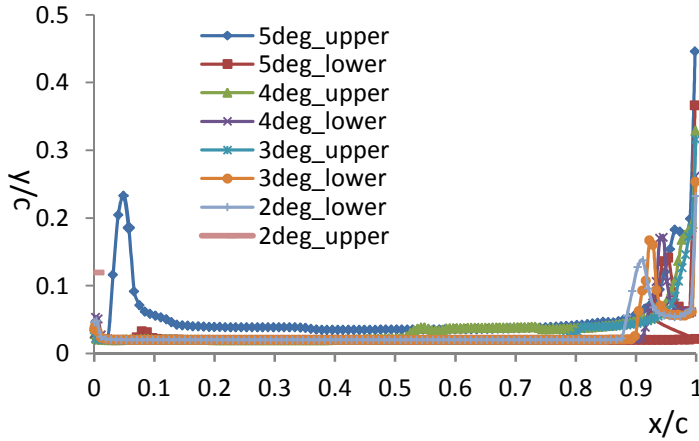


Fig 4. Calculated intermittency distribution on the lower and upper side of NACA16012 foil with different attack angles

Calculated results on pressure coefficient, intermittency, turbulence intensity and velocity distribution are shown in Figs. 2 and 3. Figure 4 summarizes the intermittency distribution along the chord direction on both surfaces with angle of attack from  $2^\circ$  to  $5^\circ$ . The onset of transition is defined at the location

where the intermittency first starts to increase due to the production of turbulent kinetic energy in the boundary layer. Combined with the results shown in Figs. 2 and 3, the location of onset and the extent of transition can be acquired for comparing with experimental results (i.e. Fig. 1). For the case with the angle of attack of  $5^\circ$ , transition starts at the location close to the leading edge on the upper surface of hydrofoil ( $0.02 x/c$ ), whereas it happened on the rear end of axis on the lower surface ( $0.75 x/c$ ). Similar results acquired on the lower surface for the case with the angle of attack of  $2^\circ$ , whereas on the upper surface, transition starts at the position a little behind the middle point of chord ( $0.55 x/c$ ) and ends at the position of  $0.9 x/c$ . With the decreasing of attack angle, the transition onset point moves from the leading edge to the rear end on the upper surface of hydrofoil. All these results are in good agreement with experimental results. However, 2D results only show the turbulence distribution across the boundary layer varying along the chord direction. In order to capture the span-wise distribution of turbulence level in the boundary layer, 3D boundary layer models have been built and calculated under the same flow conditions.

### 3.2 Intermittency Distribution on the Upper Surface

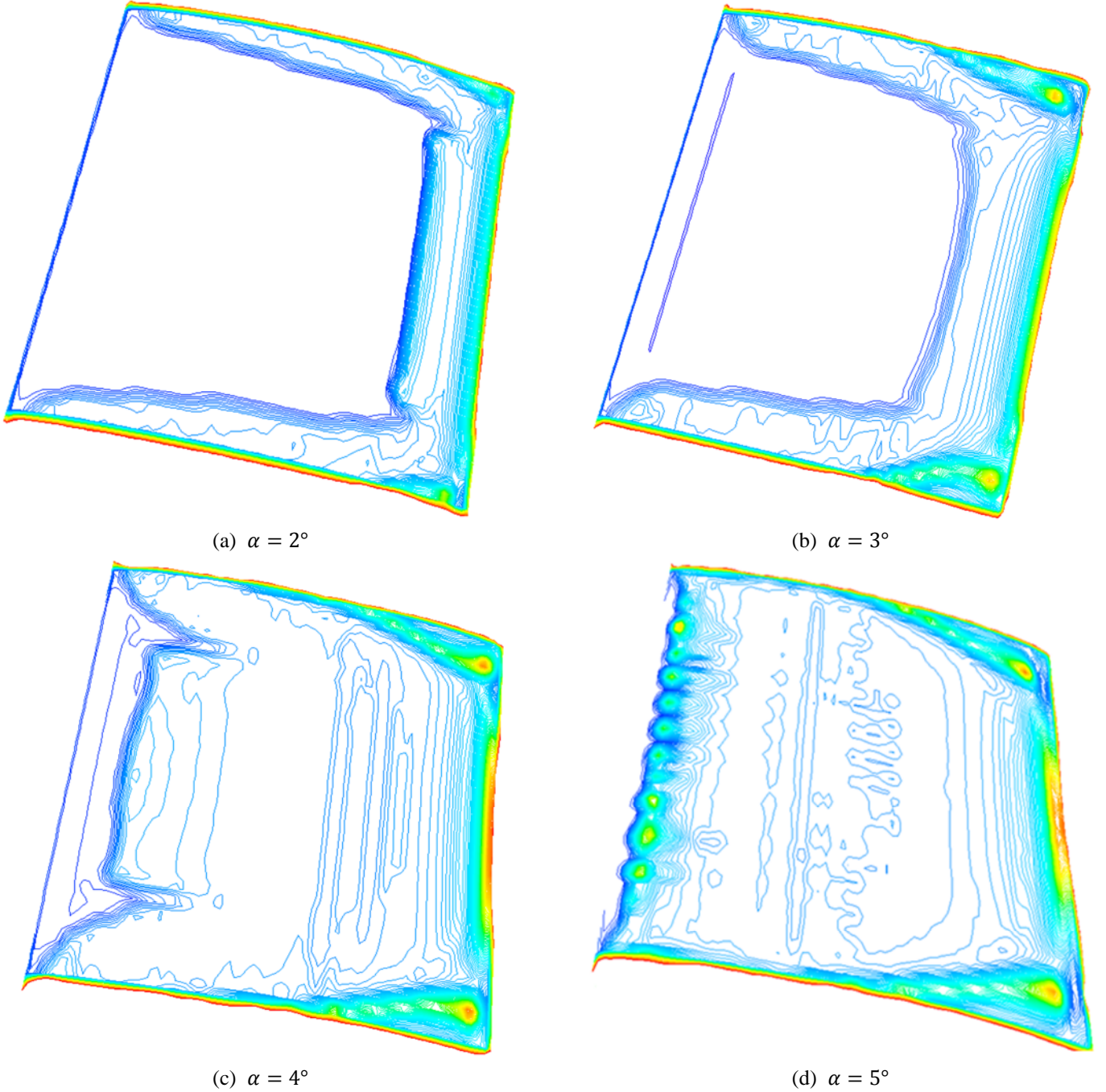


Fig 5. Calculated intermittency distribution on the upper surface of NACA 16012 foil with different attack angles

Figure 5 shows the calculated evolution of the span-wise intermittency distribution on the upper surface of NACA 16012 foil with angle of attack varying from  $2^\circ$  to  $5^\circ$ . In addition to the 2D results, the span-wise characteristics of intermittency (i.e. turbulence) for the case of the attack angle of  $5^\circ$  shows a strong span-wise wavy feature. Owing to a very low free-stream turbulence intensity (i.e. 0.165%), this feature does not appear in other cases. For comparison, case (c) with different initial turbulence intensity ( $T_u = 2\%$ ) has been calculated with the result shown in Fig. 6. This streaky characteristics of turbulence

in span-wise becomes clearer and the transition onset moves a little forward.

All these calculated information not only agree well with the experimental observations [7] but also reflect the physical nature of boundary-layer streaks appropriately. Now we are able to use this model to verify the parametric approach employed in [1] for showing the coincidence of the K-mode streaks with the damage strips in their span-wise regularity.



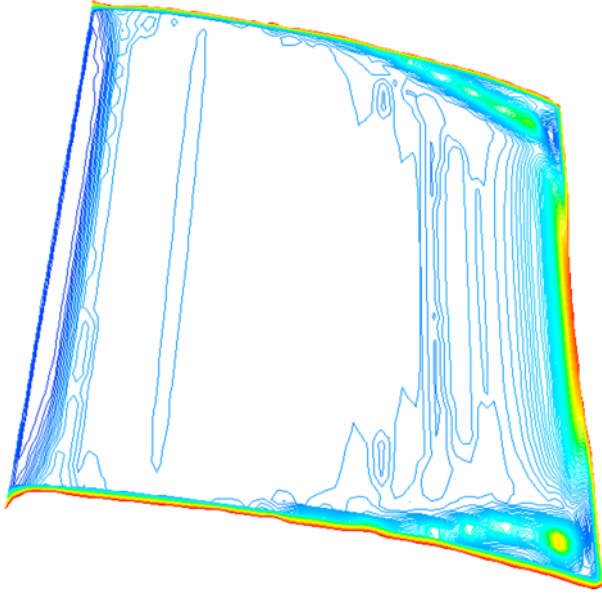


Fig. 6 Calculated intermittency distribution on the upper surface of foil (turbulence intensity:  $T_u = 2\%$ ,  $\alpha = 4^\circ$ )

#### 4. PROOF OF SPAN-WISE COINCIDENCE

If the span-wise coincidence of such calculated intermittency distribution with that K-mode streaks breakdown and turbulence production by using the parametric estimation proposed and employed in [1] can be proved for this case, then we have pushed the verification of the envisaged inception mechanism a step further. That is, the damage strip does correlate with the formation and breakdown of the boundary-layer streaks as predicted in [1].

Following the parametric approach in [1], the span-wise wavelength (spacing) of laminar streaks or Klebanoff wave,  $\lambda^*$ , can be estimated as:

$$\lambda^* = 10\delta^*$$

Here,  $\delta^*$  is the displacement thickness,

$$\delta^* = \frac{1}{3}\delta = \frac{5.49}{3} \sqrt{\frac{\nu x}{U}}$$

If  $\nu = 1.005 \times 10^{-6}$ ,  $U = 12$  m/s, when  $\alpha = 5^\circ$ , the location of calculated transition point is:  $x_{onset} = 0.003143$  m

$$\delta^* = 0.0297 \times 10^{-3} \text{ m} = 0.0297 \text{ mm},$$

$$\lambda^* = 0.297 \text{ mm}$$

The transition region is characterized by a random appearance of turbulent spots as explained in [1]. Assuming a spot generated from 20-30 such streaks, the turbulent spot spacing  $\lambda_{spot}^*$  will be:

$$\lambda_{spot}^* = 5.94 \sim 8.91 \text{ mm}$$

The width of this hydrofoil is 120 mm, at the position of laminar-turbulent transition point, there could be 10-17 streaky structures considering the 3-D effect of this foil.

The span-wise spacing of the calculated intermittency distribution on the upper surface is shown in Fig. 5d. There are

approximate 12 clearly shown streaky structures within the estimated range of K-mode streaks.

Now we have successfully demonstrated that the logic used in [1] for proving the span-wise coincidence of K-mode streaks with damage strips is correct by applying it in this experiment [7] supported numerical case.

#### 5. CONCLUSION

1. Correlation-based transition model has been adopted to study the transition process on NACA 16012 foil in non-cavitation condition. The prediction of the onset location and the extent of transition are in good agreement with experimental results proving the correctness of this approach.

2. The span-wise turbulence distribution on the upper side of hydrofoil with angle of attack varying from  $2^\circ$  to  $5^\circ$  shows how transition is affected by different incidences. A simple comparison (i.e. Fig. 5c and Fig. 6) provides a clue that the free-stream turbulence level has apparently an effect on turbulence production in the boundary layer. That is, the high free-stream instabilities enter the boundary layer, promoting the transition onset (i.e. moving it forward) through the receptivity process, as analysed for the case of the Three Gorges turbine in particular the unfavoured effect of the guide plate structure [1, 2].

3. The span-wise spacing of the calculated intermittency distribution on the upper surface of hydrofoil complies well with the estimated span-wise distribution of K-mode streaks breakdown by using the parametric approach proposed in [1]. This provides a further support to the envisaged hypothesis of cavitation inception from K-mode streaks in [1].

4. This transition model serves as a good CFD tool in engineering transition modelling.

#### ACKNOWLEDGMENTS

The financial support from the Royal Academy of Engineers (RESCM 3021), the technical and financial support from the Three Gorges authority and the PhD studentship provided jointly by the Chinese Scholarship Council (CSC) and the School of Engineering (University of Warwick) are highly appreciated.

#### REFERENCES

- [1] Li, S. C., 2006, "Challenge to Modern Turbine Technologies: Analysis of Damage to Guide Vane Surface of Three Gorges Turbine," Invited Plenary Speech at the 1st International Conference on Hydropower Technology and Key Equipment, 27-29 Oct, Beijing, pp. 96-112.
- [2] Chen T. and Li. S. C., 2011, "Numerical Investigation of Guide-Plate Induced Pressure Fluctuations on Guide Vanes of Three Gorges Turbines," J. Fluids Eng., **133**(6), pp. 1-10.
- [3] Li, S. C., 2001, Cavitation of Hydraulic Machinery, Imperial College Press, London, Chap. 2.



[4] Menter, F. R., Langtry, R. B., Likki, S. R., Suzen, Y. B., Huang, P. G., and Völker, S., 2004, "A Correlation Based Transition Model Using Local Variables Part I-Model Formulation," Vienna, ASME Paper No. ASME-GT2004-53452.

[5] Abu-Ghannam, B. J., and Shaw, R., 1980, "Natural Transition of Boundary Layers-The Effects of Turbulence, Pressure Gradient, and Flow History," *J. Mech. Eng. Sci.*, **22**(5), pp. 213–228.

[6] Menter, F. R., Esch, T., and Kubacki, S., 2002, "Transition Modelling Based on Local Variables," 5th International Symposium on Turbulence Modeling and Measurements, Mallorca, Spain.

[7] Franc J. P. and Michel J. M., 1985, "Attached Cavitation and the Boundary Layer: Experimental Investigation and Numerical Treatment," *J. Fluid Mech.* **154**, pp. 63–90.

[8] Menter, F. R., 1994, "Two-Equation Eddy-Viscosity Turbulence Models for Engineering Applications," *AIAA J.*, **32**(80), pp. 1598–1605;

## High-speed micro-scale observations of nuclei-induced sheet cavitation

M.X. van Rijsbergen\*  
Maritime Research Institute Netherlands (MARIN)

T.J.C. van Terwisga  
Maritime Research Institute Netherlands (MARIN),  
Delft University of Technology, The Netherlands

\* m.v.rijsbergen@marin.nl

### ABSTRACT

High-speed video observations were conducted on micro-scale in order to reveal detailed information on the diameter, form and trajectories of nuclei that cause sheet cavitation inception on a NACA 0015 foil. The sizes found ranged from 15 to 430  $\mu\text{m}$ . From the observed shapes and behaviour of the nuclei it is concluded that the water in the cavitation tunnel mainly contains solid nuclei. After filtering of the water also gas and fluid nuclei were observed to cause cavitation inception. Comparison of the bubble trajectories with calculated streamlines showed increasing deviations with the size of the gas nuclei. The largest bubbles showed strong deformations due to strong deceleration and acceleration.

### NOMENCLATURE

$C_{P_{\min}}$	minimum pressure coefficient	$\frac{P_{\min} - P_0}{\frac{1}{2}\rho V^2}$	-
$c$	foil chord length		m
$D$	nucleus diameter		m
$D_{\text{eq}}$	average equivalent nucleus diameter		m
$P_0$	pressure in test section		Pa
$P_{\min}$	minimum pressure on foil		Pa
$P_v$	vapour pressure of water		Pa
$Re$	Reynolds number	$\frac{Vc}{\nu}$	-
$V$	velocity in test section		m/s
$\nu$	kinematic viscosity of water		$\text{m}^2/\text{s}$
$\rho$	mass density of water		$\text{kg}/\text{m}^3$
$\sigma$	cavitation number	$\frac{P_0 - P_v}{\frac{1}{2}\rho V^2}$	-

### 1. INTRODUCTION

Sheet cavitation occurs on ship propellers and rudders, but also on pump rotors and stators. The sheet cavity is induced by a local suction peak (below the vapour pressure) at the leading edge of the object and this is also where the cavity is attached to the object. In general, the cavity is quite thin relative to its width and length and therefore it is called a sheet. But apart from a low pressure and a point of attachment, a nucleus is necessary to induce a phase transition from liquid to gas. By experiments in a

cavitation tunnel, Keller [1] has shown that both micro particles and bubbles can act as nuclei for cavitation inception. Filtering and degassing of the water had a detrimental effect on the occurrence of cavitation. In natural waters, O'Hern [2] found very high concentrations of micro bubbles and particulates, including micro plankton, causing a low tensile strength of the water.

On full scale, the combination of abundant nuclei and high Reynolds numbers cause cavitation inception to occur very close to the vapour pressure. In experiments in model facilities however, scale effects occur and often cavitation inception is delayed. In general, this is thought to be due to viscous effects (Reynolds number), but also the surface tension may play a role (Weber number). This is not only unfavourable for the study of inception itself (e.g. regarding the possibility of acoustic detection), but also for experiments aimed at assessing the risk of cavitation erosion, and experiments measuring the radiated pressure fluctuations from a cavitating propeller.

Kuiper [3] has shown that leading edge roughness can resolve this problem in a cavitation test facility. From experiments on a propeller model he concluded that no further nuclei seeding is necessary, but Van Rijsbergen et al. [4] showed that both free stream nuclei and leading edge roughness are necessary for sheet cavitation inception at model scale Reynolds numbers. A conceptual model was proposed in which scale effects caused by bubble screening, Weber and Reynolds number were taken into account. A first numerical evaluation of the model based on estimated parameter values such as nucleus diameter range and minimum pressure coefficient at a roughness element showed its potential, but a better experimental foundation was deemed necessary. Therefore, a series of micro-scale observations at high temporal and spatial resolutions were carried out to track the nuclei that cause cavitation inception. The work outlined below describes and discusses the first results of this investigation and further defines the necessary steps to be done to determine the limiting conditions for sheet cavitation inception.

### 2. TEST SET-UP

MARIN's high speed cavitation tunnel (see Figure 1) is very suitable for micro-scale experiments. In its rectangular test section of 80 mm height and 40 mm width, a velocity ( $V$ ) between 8 and 20 m/s can be reached at a cavitation number ( $\sigma$ ) of 2.0. A heat exchanger using fresh water keeps the tunnel water temperature at around 20 degrees C. The tunnel has a micro filter and deaeration system to adjust the water quality. A 2D NACA 0015 section with a chord length of 60 mm was placed in the test section at an angle of attack of 6.0 degrees.

Initially an area of about 2 by 3 mm at the leading edge was covered with carborundum roughness elements with an average grain size of 60  $\mu\text{m}$ . The test section pressure is measured 72 mm upstream of the point of rotation of the foil. The test section velocity is obtained by measuring the pressure drop over the contraction.

Two Photron Fastcam SA5 high speed cameras were used for observation, together with two 400 W HMI lamps for lighting. The SA5 has a one megapixel sensor with a pixel size of 20  $\mu\text{m}$ . The tests were carried out at a frame rate of 15 kHz and a typical resolution of 704x696 pixels. One camera was positioned with a plan view of the leading edge of the foil (designated as top camera). A Nikkor 60 mm macro lens enabled an image pixel size of 30  $\mu\text{m}$  and a field of view of about 21x21 mm, at the cost of a depth of field of about 1 mm. Due to limitations in the positioning of the lighting, at least a shutter time of 9  $\mu\text{s}$  had to be used, causing some motion blur over 3 pixels for a nucleus moving at a speed of 10 m/s. The other camera was positioned with a section view of the foil's leading edge (designated as side camera). An Infinity K2 long distance microscope generated an image pixel size of 5  $\mu\text{m}$ , a field of view of about 3.5x3.5 mm and a depth of field of about 10  $\mu\text{m}$ . Using shadowgraphic lighting, a shutter time of 1  $\mu\text{s}$  could be used, causing motion blur over 2 pixels for a nucleus moving at a speed of 10 m/s.

Hoekstra et al. [5] calculated a  $-C_{pmin}$  of 2.08 on this foil at the same angle of attack in a similar 3D set-up. With a correction of the position of the reference pressure this becomes 2.22, so the cavitation inception number was expected to be about 2.2.

The test procedure was as follows. The side camera was focussed on the largest roughness element in the area. The cameras were synchronized and using the circular memory buffer, the trigger mode was set at the end of a 0.8 s recording time. Synchronized tunnel pressure and velocity measurements were made at the same frame rate and pre-trigger time as the cameras using an Acquitek PCI card in a PC. The tunnel was set at  $V = 10$  m/s and  $\sigma = 4$ . Then, the pressure was reduced. As soon as cavitation inception was observed by the top camera, the recording as well as the pressure decrease were stopped. If the side camera was focussed on the right roughness element where inception started, also the nuclei causing this was captured on 5 to 15 frames. During the tests, the roughness distribution and water quality was further optimized. Figure 2 shows the four roughness distributions that were used. In the first test series, 9 out of 10 of the inception events were caused by solid particles. Further, in many cases, cavitation inception did not occur on the roughness element in focus of the side camera. Two actions were taken: the water was filtered and the roughness area was made smaller by mechanically removing half of the roughness elements. In the next series, relatively more gas nuclei were observed and they were better in focus. Because already many solid nuclei were observed, and still some of the nuclei were out of focus, the water was filtered again and a new strip of roughness elements was applied. These roughness elements had an average size of 120  $\mu\text{m}$ . Furthermore, some large roughness elements of about 3 mm were placed at the midchord position at the sides of the foil to generate gas nuclei in the tunnel at low cavitation numbers. Apart from this action, no particular seeding with solid or gas nuclei was performed. With this configuration many in-focus nuclei were observed. However, because most of

the inception events were recorded at relatively high cavitation numbers, it was concluded that the 120  $\mu\text{m}$  roughness elements on the leading edge were too large. Therefore a single roughness element was taken from the standard (60  $\mu\text{m}$ ) roughness distribution. Once glued to the leading edge at the position of the calculated minimum pressure, the element turned out to have a height above the surface of 80  $\mu\text{m}$ . The dissolved gas content was kept at about 30 % by deaerating the water after every replacement of the foil.

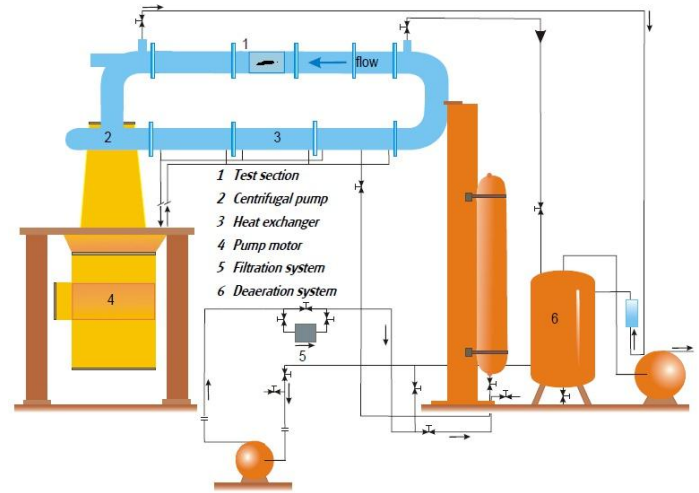


Figure 1: MARIN's high speed cavitation tunnel

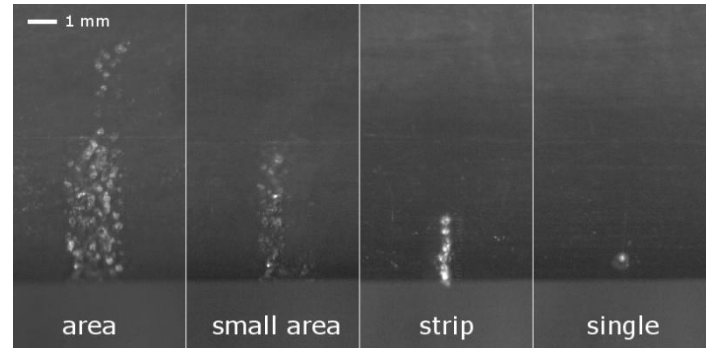


Figure 2: Roughness distributions on leading edge of foil

### 3. IMAGE PROCESSING

To enable a quantitative analysis of the images obtained by the side camera, the images of each test were manually fitted with respect to position and size to a reference image. Since it was envisaged that eventually the deviation of the nuclei trajectories from streamlines could be determined by this data, the computational data set as determined by Hoekstra et al. [5] was taken as a reference. Using a MATLAB script, the images with nuclei were subtracted from a background image and subsequently thresholded and filtered to obtain the equivalent diameter and position (centre of mass) of the nuclei. It should be noted that the diameters determined by this optical technique are strictly speaking minimum values because of the very small depth of field of the microscope. The images of the same nuclei at subsequent time steps were projected on the original camera background (see e.g. Figure 3) and the computational data (see e.g. Figure 9). In this paper, a total of 16 tests were analysed. A subset of 6 cases is described in more detail in the next section.

## 4. RESULTS

Figures 3 to 8 show 6 cases of cavitation inception. Each figure gives a series of “photo finish” images from the top camera on the left and on the right a combined image of the nucleus observed at several time steps by the side camera. Length scales of 1 mm are projected for reference purposes. In 5 of the 6 figures, two vertical white lines between the top camera images indicate the time steps in which the same nucleus is observed by the side camera. The average equivalent diameter ( $D_{eq}$ ), cavitation number and velocity are given below the figure for each event. The Reynolds numbers vary between  $4.7$  and  $6.3 \cdot 10^5$  for these cases.

Figure 3 (case 1) shows a spherical nucleus with  $D_{eq} = 165 \mu\text{m}$  causing inception on a roughness element. Detailed observation of the side camera images show that the nuclei surface contains several irregularities which look like small hairs. The nucleus is not transparent but it does reflect sufficient light to be clearly visible on the top camera images before and after inception. Unfortunately in this case, a roughness element 1 mm to the left already cavitated, so the inception event on the top images is not so clear.

Figure 4 (case 2) shows a spherical nucleus with  $D_{eq} = 176 \mu\text{m}$  causing inception on another roughness element. The cavitation number is much lower, so the sheet that develops is significantly larger. To show the full width of the turbulent streak, the individual top camera images are twice as wide as in case 1. Consequently fewer images can be shown before inception occurs. But even though the nucleus is transparent, it does not reflect sufficient light to be visible on the top camera images.

Figure 5 (case 3) shows a spherical nucleus with  $D_{eq} = 66 \mu\text{m}$  causing inception on yet another roughness element. This nucleus comes very close to the stagnation point of the foil. Therefore it is visible from the top on the first 3 to 5 images only.

The nuclei of cases 1, 2 and 3 have the following characteristics in common: they neither visibly deform nor change in diameter and can be distinguished from the generated cavity at the moment of inception. Furthermore, they do not visibly decelerate near the stagnation point, but they all accelerate towards the point of minimum pressure.

Figure 6 (case 4) shows the largest nucleus ( $D_{eq} = 433 \mu\text{m}$ ) observed in the current data set that causes inception on a roughness element. It is clearly visible on the top camera images upstream of the foil and after inception it leaves a gaseous cavity that sheds gas bubbles continuously. It enters the field of view of the side camera already heavily deformed into a disk because of the deceleration. It is deflected by the stagnation point and clearly follows a much higher path than previous nuclei. Then, it is accelerated as can be seen from the formation of a torpedo shape and the larger distances between the images.

Figure 7 (case 5) shows a nucleus with  $D_{eq} = 85 \mu\text{m}$  causing inception on the single roughness element now on the leading edge. The top camera images clearly show that the nucleus is decelerated upstream of the leading edge. The side camera images show the deceleration, but also the acceleration in vertical direction and deformation in the two frames before inception. Further analysis of the top camera images shows that the nucleus does not hit the roughness element in the centre but more on the right. Remarkably, the nucleus seems to stay intact while it passes the cavity and continues downstream.

Figure 8 (case 6) shows a nucleus with  $D_{eq} = 34 \mu\text{m}$  causing inception on the single roughness element. Because the size of the nucleus is now about the pixel size of the top camera image, it cannot be discerned on these images, except for the frame just before inception. Here the nucleus expands to about  $60 \mu\text{m}$ , which can be seen on the top camera image as a faint line. Again the nucleus passes on the right hand side and seems to cause a local bulb in the streak of cavitation.

The trajectories of the experimentally observed nuclei can also be compared with the computational data obtained by Hoekstra et al. [5]. Figures 9 and 10 show the streamlines and the local velocity normalized with the inflow velocity. The field of view of the side camera, the roughness outside the computational foil and the observed nuclei are projected on the CFD data. The figures show that quite different parts of the leading edge were observed in cases 2 and 4. Also the differences in the trajectories of a solid nucleus and a gas nucleus becomes more clear. Figure 9 shows that the nucleus in case 2 tends to go to a more inward streamline. The nucleus of case 4 in Figure 10 is pushed to a more outward streamline, but when close to the point of minimum pressure, it is directed again towards the foil.

For comparison of the trajectories of all 16 nuclei, a series of figures is made in which the trajectories are plotted as lines with round markers. For clarity, the nuclei are sorted in four groups: non-deformed nuclei and deformed nuclei with  $D_{eq}$  up to 40, 100 and  $500 \mu\text{m}$  respectively. The distinction between non-deformed and deformed nuclei is made on the basis of the side camera images, as described for the cases above. The marker size is proportional to  $D_{eq}$ , but the scale factor is adapted for each figure to remain good visibility of the nuclei positions. Figures 11 to 14 show the following:

- The non-deformed nuclei with  $D_{eq}$  above  $130 \mu\text{m}$  and the deformed nuclei with  $D_{eq}$  below  $50 \mu\text{m}$  move to more inward laying streamlines.
- The non-deformed nuclei with  $D_{eq}$  between  $57$  and  $67 \mu\text{m}$  follow the streamlines quite well.
- All deformed nuclei with  $D_{eq}$  between  $50$  and  $430 \mu\text{m}$  move to more outward laying streamlines near the stagnation point, but move inward near the point of minimum pressure.
- The deflections of the nuclei from their original streamlines are approximately proportional to their equivalent diameter.
- The layer from which nuclei can reach the point of minimum pressure on this foil is roughly 1 mm wide. This is about 10% of the thickness of the foil.

## 4. DISCUSSION

Various types of cavitation nuclei were observed with different appearances and trajectories. By combining the available information, the phase of the nuclei (solid, liquid or gas) may be determined.

- The nuclei in cases 1, 2 and 3 do not deform and continue after inception. As the largest ones move to more inward laying streamlines, their density is probably higher than that of water. All three are therefore considered to be solid particles, with the following distinctions:
  - The nucleus in case 1 is completely black, while a gas nucleus would have a bright spot in the centre because of reflections of the light.
  - The nucleus in case 2 is transparent, so it may be made of plastic or glass.

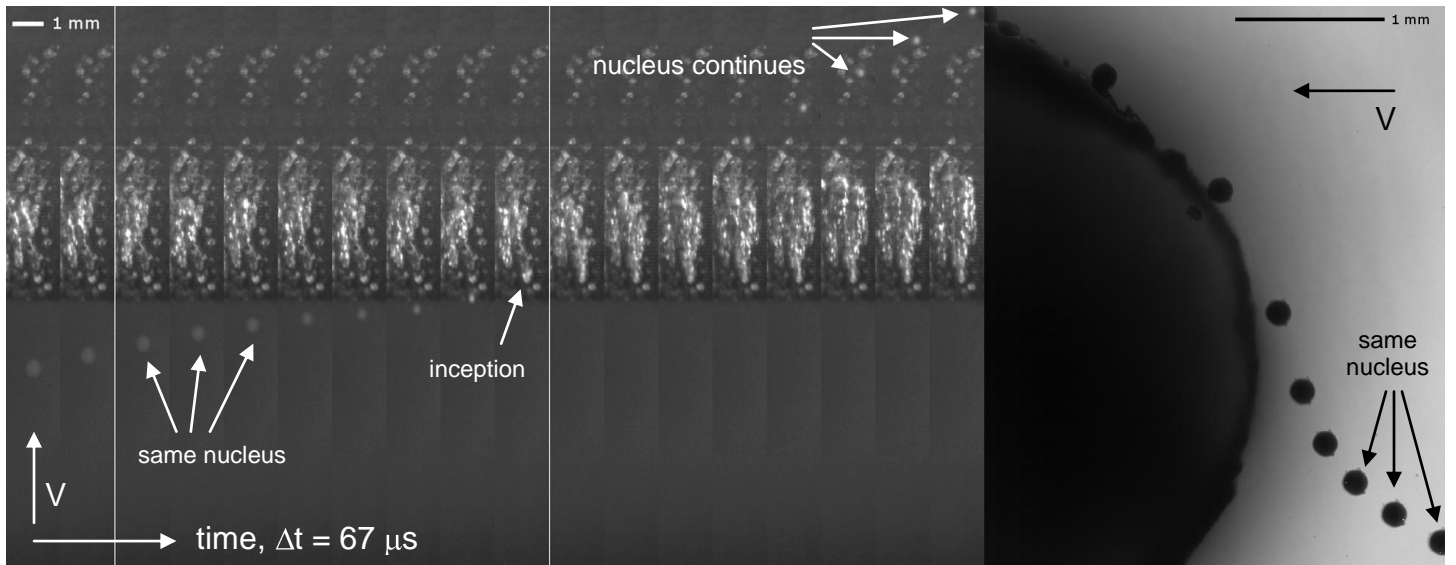


Figure 3: Case 1,  $D_{eq} = 165 \mu\text{m}$ ,  $\sigma = 2.27$ ,  $V = 10.0 \text{ m/s}$ , original roughness area

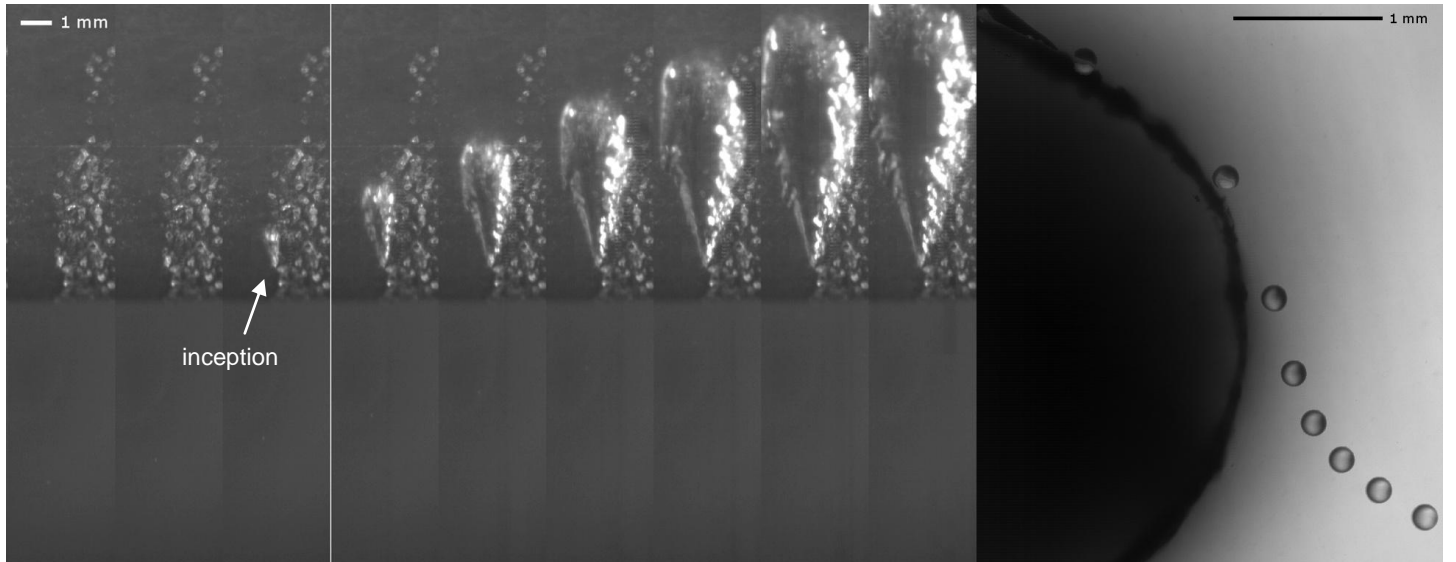


Figure 4: Case 2,  $D_{eq} = 176 \mu\text{m}$ ,  $\sigma = 1.82$ ,  $V = 10.2 \text{ m/s}$ , original roughness area

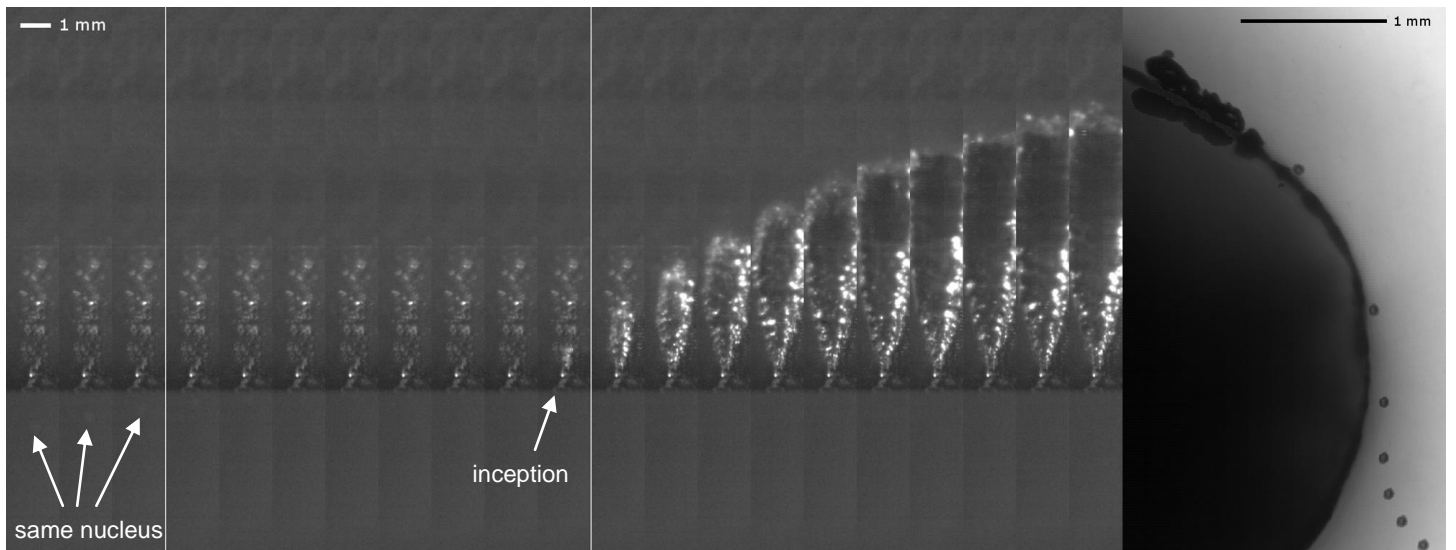


Figure 5: Case 3,  $D_{eq} = 66 \mu\text{m}$ ,  $\sigma = 2.10$ ,  $V = 10.0 \text{ m/s}$ , small roughness area



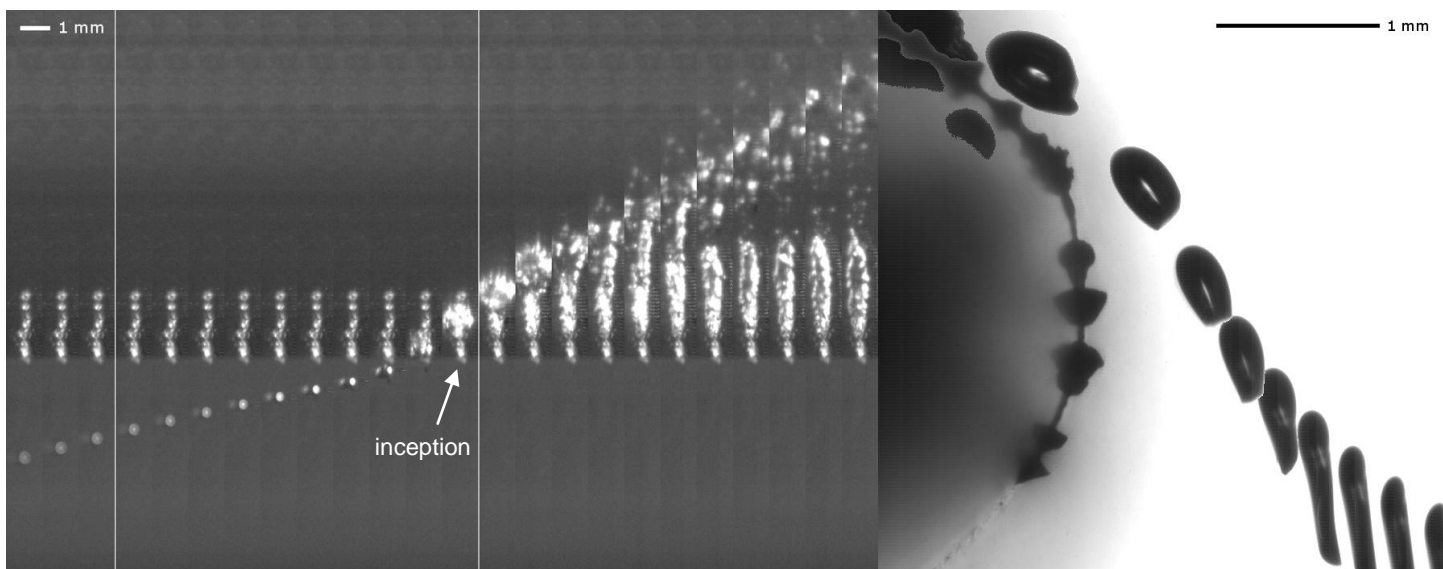


Figure 6: Case 4,  $D_{eq} = 433 \mu\text{m}$ ,  $\sigma = 2.50$ ,  $V = 8.0 \text{ m/s}$ , roughness strip

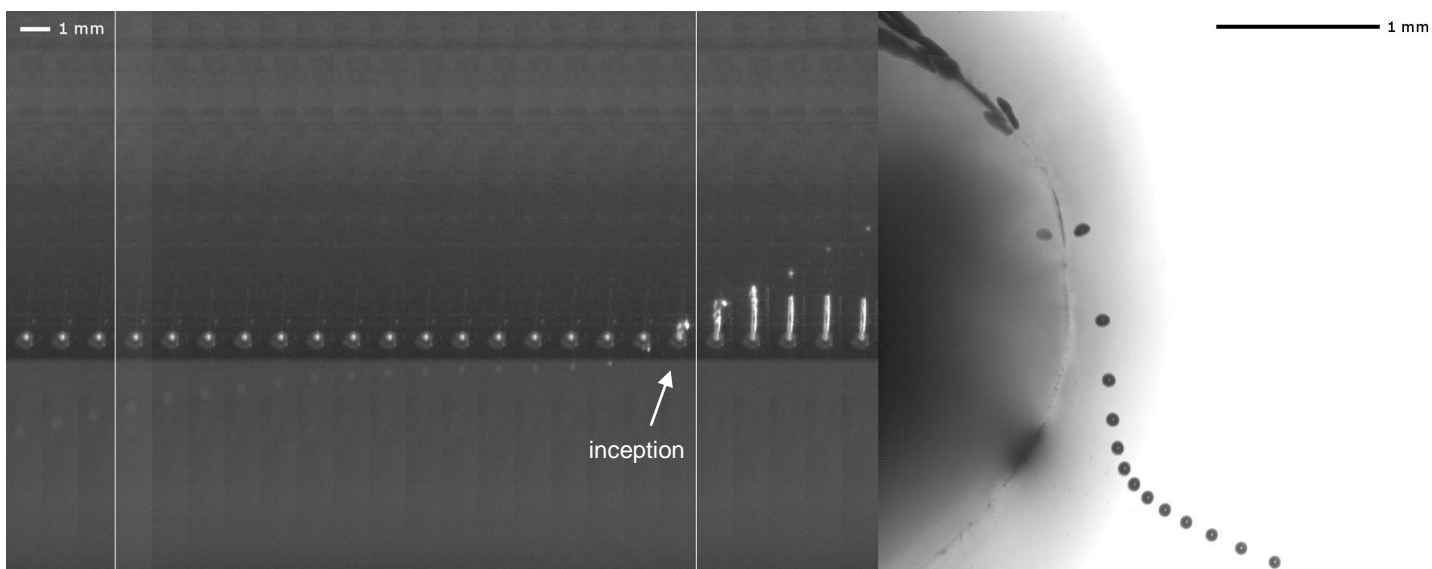


Figure 7: Case 5,  $D_{eq} = 85 \mu\text{m}$ ,  $\sigma = 2.15$ ,  $V = 7.9 \text{ m/s}$ , single roughness element

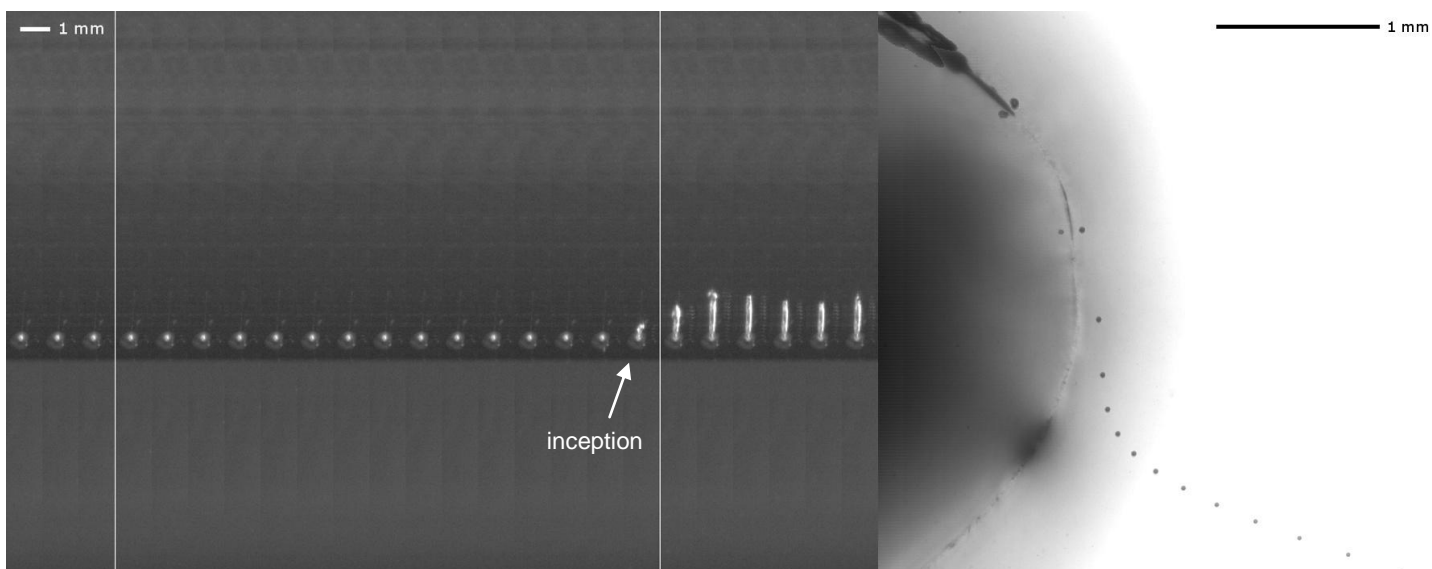


Figure 8: Case 6,  $D_{eq} = 34 \mu\text{m}$ ,  $\sigma = 2.03$ ,  $V = 8.5 \text{ m/s}$ , single roughness element

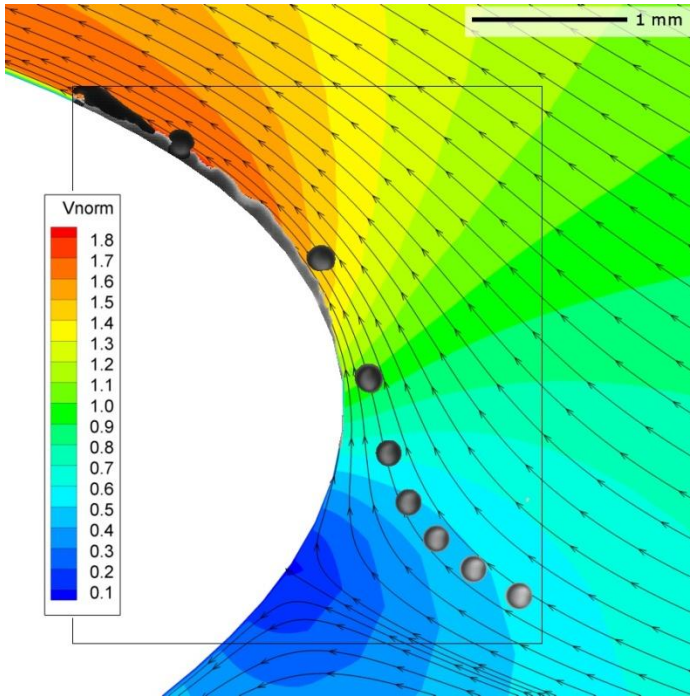


Figure 9: Combination of CFD and experimental data for case 2

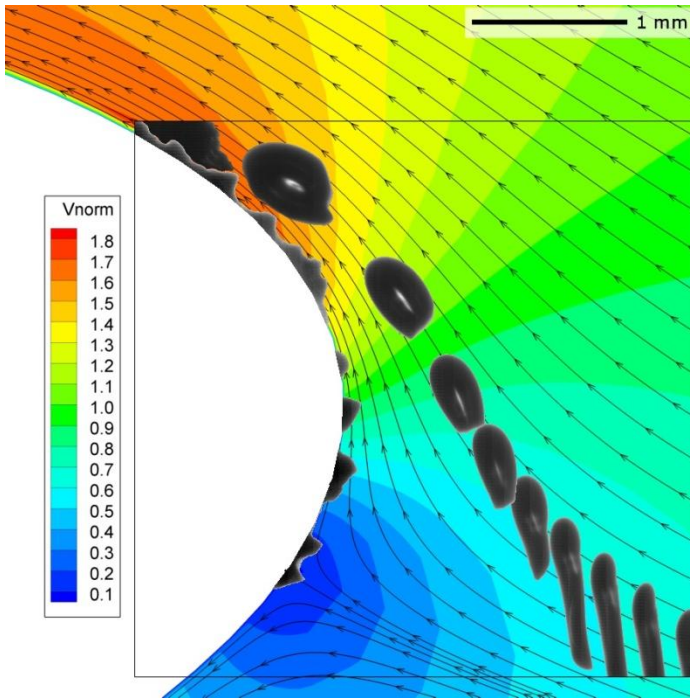


Figure 10: Combination of CFD and experimental data for case 4

- The nucleus in case 4 deformed heavily, it is deflected from the stagnation point and attracted to the point of minimum pressure. Furthermore, it left a relatively large cavity at the roughness strip. These observations lead us to the conclusion that it is a gas bubble.
- The nuclei in cases 5 and 6 deform, but seem to continue after inception. Therefore, it is thought that these nuclei are liquid (most likely oil) droplets, with a density smaller than water.

Figure 11 shows that in the present data set all non-deformed (solid) nuclei either follow the streamlines or move to more inward laying streamlines. These are therefore very effective nuclei for cavitation inception. All deformed nuclei, larger than  $50 \mu\text{m}$  (gas or liquid, see Figures 13 and 14) have a risk of being screened from the leading edge because they are deflected from the stagnation point. The attraction to the point of minimum pressure however balances this up to  $D_{eq} = 430 \mu\text{m}$  at  $V = 8.0 \text{ m/s}$ . The last bubble image before inception in Figure 10 shows that in this case, the large roughness size may be the reason for attachment to the foil surface.

Before extensive filtering of the water, the ratio between solid and gas nuclei was about a factor 10. Mees et al. [6] have found a similar ratio in the GTH by comparison of results obtained from several nuclei measurement techniques. Apparently this is typical for cavitation tunnels.

The results as outlined above are favourable for cavitation inception event rates in cavitation tunnels. Inception is caused either by a solid nucleus or a bubble up to  $430 \mu\text{m}$ . According to the measurements by Mees et al. [6], this is practically 99% of the nuclei spectrum. In a depressurized towing tank however, where gas nuclei rise, solid nuclei sink and velocities are a factor two to three lower, the situation is thought to be more critical. Therefore, future experiments and computations should focus on the determination of critical bubble diameters at lower free stream velocities.

From the total set of observations, an upstream layer thickness of about 1 mm is estimated from which nuclei are effective in causing cavitation. Using this layer thickness, a minimum free stream nuclei concentration, necessary for cavitation inception, can be estimated. For example, if a propeller blade passes through a wake peak, cavitation inception should occur on model scale within 5 degrees rotation for a propeller model with a diameter of 0.26 m at a relative radius ( $r/R$ ) of 0.9. The leading edge travels then about 10 mm. This should occur at a range of radii, every 1 mm. So there should at least be one nucleus in  $0.01 \text{ cm}^3$ , or 100 nuclei per  $\text{cm}^3$ . This corresponds roughly with the concentrations as measured by Mees et al. [6].

#### 4. CONCLUSIONS AND RECOMMENDATIONS

The micro-scale high-speed video observations as presented in this paper provide a unique experimental data-set on the shape and trajectories of nuclei that induce sheet cavitation inception on a NACA 0015 foil. More specifically, for the current test set-up and the tested conditions, the following conclusions can be drawn.

- Solid micro particles are very effective cavitation nuclei. Without filtering, the tunnel water contained mainly solid nuclei.
- After filtering, more inception events were observed to be caused by gas and fluid nuclei. Dependent on size and density these deform and deflect because of strong pressure gradients at the leading edge of the foil.
- At a velocity of 8 m/s, almost all free stream nuclei of a realistic nuclei spectrum can cause sheet cavitation inception.
- Future experiments and computations should focus on the determination of critical bubble diameters at lower velocities.



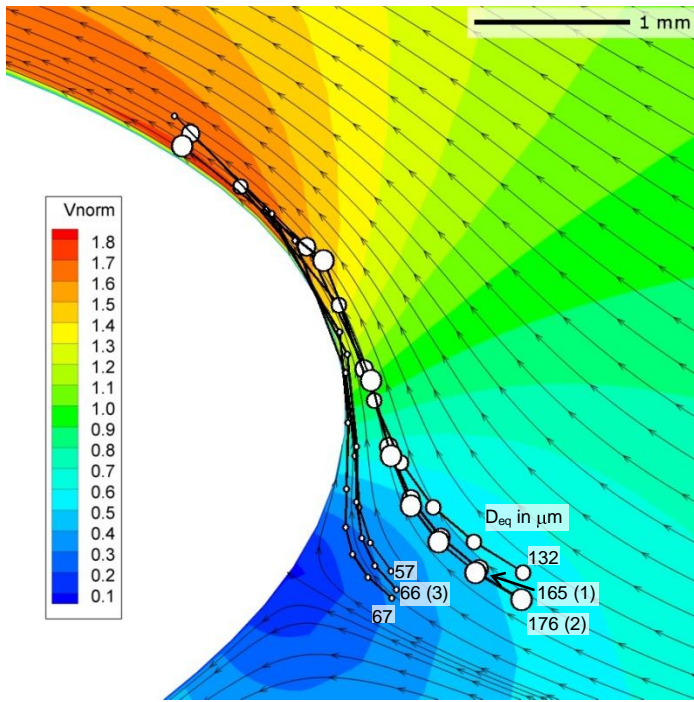


Figure 11: Positions and  $D_{eq}$  of non-deformed nuclei combined with CFD velocity data, case numbers between brackets.

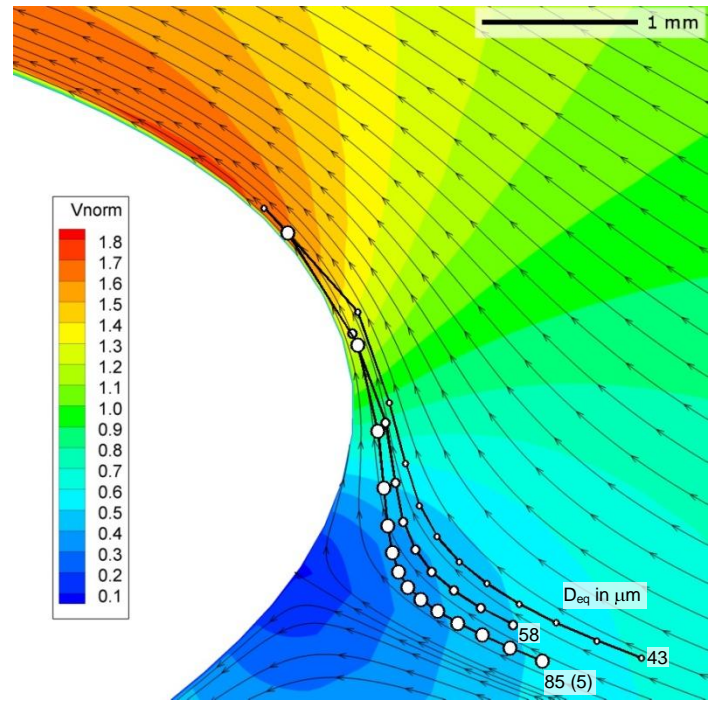


Figure 13: Positions and  $D_{eq}$  of deformed nuclei up to 100  $\mu\text{m}$  combined with CFD velocity data, case number between brackets.

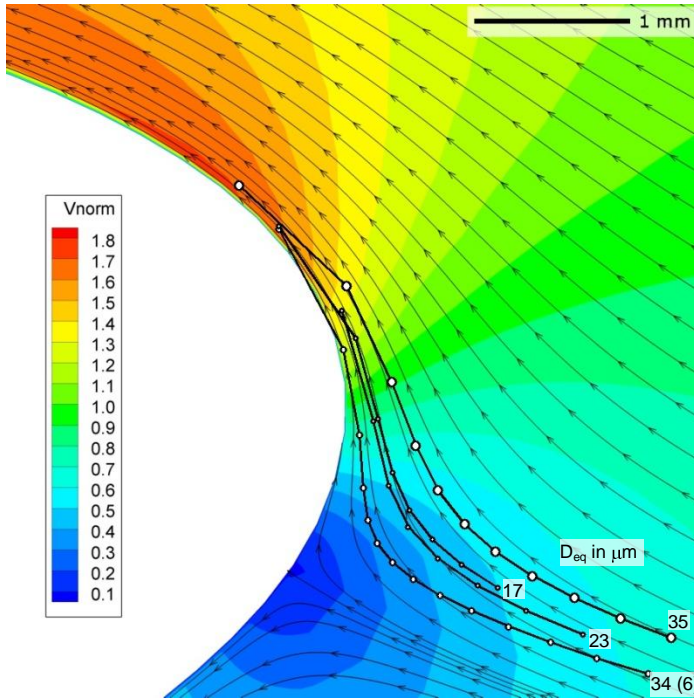


Figure 12: Positions and  $D_{eq}$  of deformed nuclei up to 40  $\mu\text{m}$  combined with CFD velocity data, case numbers between brackets.

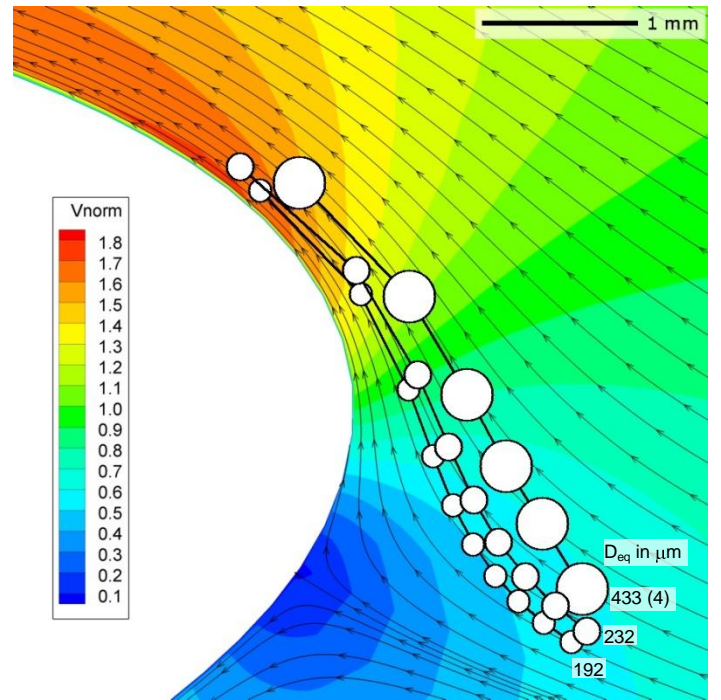


Figure 14: Positions and  $D_{eq}$  of deformed nuclei up to 500  $\mu\text{m}$  combined with CFD velocity data, case numbers between brackets.

## REFERENCES

- [1] Keller, A.P., Investigations concerning scale effects of the inception of cavitation, Proceedings Conference on Cavitation, Institute of Mechanical Engineers, Edinburgh, Scotland, pp. 109-119, 1974
- [2] O'Hern, T.J., Cavitation inception scale effects: Nuclei distributions in natural waters, Cavitation inception in a turbulent shear flow, Ph. D. Thesis, California Institute of Technology, 1987
- [3] Kuiper, G., Cavitation inception on ship propeller models, Ph. D. Thesis, Netherlands Ship Model Basin, Wageningen, 1981
- [4] Van Rijsbergen, M.X., Van Terwisga, T.J.C., Water Quality Effects on Sheet Cavitation Inception on a Ship Propeller Model, 7th International Conference on Multiphase Flow, Tampa, Florida, 2010
- [5] Hoekstra, M., Vaz, G., The partial cavity on a 2D foil revisited, CAV2009, Ann Arbor, Michigan, 2009
- [6] Mees, L., Lebrun, D., Allano, D., Walle, F., Lecoffre, Y., Boucheron, R., Frechou, D., Development of interferometric techniques for nuclei size measurement in cavitation tunnel, 28<sup>th</sup> Symposium on Naval Hydrodynamics, Pasadena, California, 2010

## Cloud Cavitation and Cavitation Erosion in Convergent Divergent Nozzle

T. Keil, P. F. Pelz\*, U. Cordes, G. Ludwig  
Technische Universität Darmstadt  
Chair of Fluid Systems Technology  
Magdalenenstraße 4, 64289 Darmstadt  
Germany

Peter.Pelz@fst.tu-darmstadt.de

### ABSTRACT

The influence of flow parameters such as cavitation and Reynolds number on the cavitating cloud behaviour and their aggressiveness are analysed in an experimental work.

The geometry under focus is a convergent-divergent nozzle with a given radius of curvature at the minimum cross section. By means of a high-speed camera the kinematics of cloud cavitation is visualized. The aggressiveness of the cloud is quantified by using soft metal layers adapted on the nozzle geometry. The interpretation of the plastic deformation, called pits, is done via a 2-dimensional optical measurement system, which is developed to scan large and curved surfaces. By doing this damage maps are gained.

Consequently dimensional analysis is used, to analyse and generalize the experimental findings. Thus a critical Reynolds number is found for the transition from sheet to cloud cavitation. Further an upper limit for the Strouhal number is found for the given geometry.

### NOMENCLATURE

letter		
$E$	plastic deformation energy	$ML^2T^{-2}$
$f$	frequency	$T^{-1}$
$H$	channel height	$L$
$h$	nozzle height	$L$
$L$	sheet length	$L$
$L_m, l_m$	material length	$L$
$p$	pressure	$ML^{-1}T^{-2}$
$Q$	volume flow	$L^3T^{-1}$
$R$	radius	$L$
$Re$	Reynolds number	-
$St$	Strouhal number	-
$U$	velocity	$LT^{-1}$
$x$	coordinate	$L$
$\Gamma$	circulation	$L^2T^{-1}$
$\sigma$	cavitation number	-
$\rho$	density	$ML^{-3}$
$\lambda$	non-dim. sheet length	-
$\gamma$	non-dim. Circulation	-
$\pi$	non-dim. damage energy	-
$\vartheta$	yield stress	$ML^{-1}T^{-2}$

$\kappa$	geometry parameter	-
$\nu$	kinematic viscosity	$L^2T^{-1}$

### indices

$E$	inlet
$A$	outlet
$V$	vapor
$+$	dimension less

### 1. INTRODUCTION

One of the more aggressive cavitation forms is cloud cavitation which is observed above a critical Reynolds number as will be shown within this paper. The high aggressiveness of cloud cavitation was reported by several researchers (e. q.

[1], [2] and [3]). It is now understood that the cloud plays a key role in **the temporal and special energy focusing cascade** which is essential for the cavitation erosion process. The stationary energy flux of the incoming flow is concentrated in time and space in the form of clouds. As a single bubble the cavitation cloud becomes unstable when it reaches a critical size. The critical size depends on the growth rate, the initial size and the initial vapor content of the cloud [15]. When the cloud collapses the second energy focusing process starts: Like a single bubble when collapsing the cloud imposes a sink flow and focuses the kinetic energy of the surrounding fluid in its center.

The intensity of the collapse and thus the aggressiveness is determined by the dynamic behavior and by the type of the occurring structures.

Konno and Kato [3] employed a numerical model to describe the dynamic behavior of a cloud cavitation floating off from a hydrofoil. Similar investigations on a cavitating nozzle flow have been conducted by Wang [5].

The results of our experimental work presented in this paper the cloud kinematics is analyzed by using a high-speed camera. In addition, the aggressiveness of cavitation erosion is assessed by using soft metal layers, used as a material sensor. This approach offers the possibility to evaluate damage distributions and damage intensities. To quantify the effective damage energy a developed so-called pit-count measurement system is used, which detects the size and the position of each pit on the



damaged surface. The effective damage energy and thereby the cavitation aggressiveness is evaluated by a here introduced dimensionless damage function.

## 2. EXPERIMENTAL SET UP AND PARAMETER

The necessary requirements for the test rig are (i) an excellent optical accessibility, (ii) the possibility to vary the geometries curvature, and (iii) to provide an installation-opportunity for soft metal layers which serve as material sensors.

The optical access (i) is realized by a channel having rectangular cross section and walls completely made of acrylic glass. The high-speed observations are illuminated with a stroboscope for the top view perspective, for the side view perspective a laser light sheet is used. The adaptation of the copper layer (iii) is implemented directly behind the narrowest cross-section area. To initiate evenly the cavitation over the whole nozzle width, a wire with rectangular cross section seen in Fig. 1 is placed in the smallest cross section area. By doing this every side wall friction influences due to surface roughness are small in comparison to the wire influence and such not visible in the experiments.

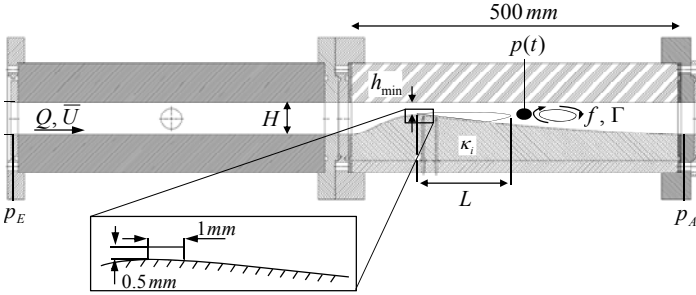


Fig. 1: Nozzle test rig at the Chair of Fluid Systems Technology.

The nozzle shape is given by the dimensionless function

$$h_+(x_+) = \frac{\text{const.}}{\exp\left(\frac{x_+}{\kappa_1}\right) + \exp\left(\frac{x_+}{\kappa_2}\right)}, \quad (1)$$

where the height  $h$  and the axial length  $x$  are made dimensionless by the channel height  $H$ . Within this paper we present and discuss only one radius of curvature  $R_+ = 2.5$  determined by the two free parameters  $\kappa_1$  and  $\kappa_2$ . The influence of both free parameters on the radius of curvature in the smallest cross section is shown in Fig. 2. The filled circle indicates the geometry being under research.

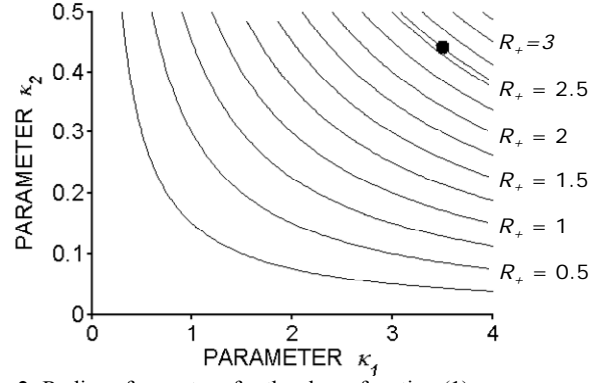


Fig. 2: Radius of curvature for the shape function (1).

The cavitation behavior is influenced by variation of the cavitation number and the Reynolds number, respectively the outlet pressure  $p_A$  and the cross section averaged flow velocity  $\bar{U}$  (see Fig. 1):

$$\sigma = \frac{p_A - p_v}{\frac{\rho \bar{U}^2}{2}}, \quad (2)$$

$$\text{Re} = \frac{\bar{U} H}{\nu}, \quad (3)$$

where  $\nu$  is the kinematic viscosity,  $\rho$  the density and  $p_v$  the vapor pressure of water.

For cloud cavitation the most relevant physical parameters are the shedding frequency  $f$  of the cavitation cloud, the typical size  $L$  of the sheet and the circulation  $\Gamma$  of the cloud. The associated dimensionless relations

$$\frac{fH}{\bar{U}} = \text{St}(\text{Re}, \sigma, \kappa_i), \quad (4)$$

$$\frac{L}{H} = \lambda(\text{Re}, \sigma, \kappa_i), \quad (5)$$

$$\frac{\Gamma}{\bar{U} H} = \gamma(\text{Re}, \sigma, \kappa_i), \quad (6)$$

are measured.

With (4), (5), (6) the largest scales of the periodic cavitation process are given. In fact cloud cavitation is similar to vortex shedding in the wake of a body. Only the physical mechanism is different. The vorticity and hence the circulation have their origin in the baroclinic source term of the vorticity equation where for vortex shedding the vorticity has its origin in the diffusion term on the right hand side of the vorticity equation.

### 3. EXPERIMENTAL RESULTS

#### High-Speed Observation

The high-speed images from the top view (Fig. 3) show a cavitation cloud formed from a cavitation sheet. The process is evaluated by a software tool detecting the front edge of the sheet and of the cloud.

The periodic process starts by the growth of the cavitation sheet to its maximum sheet length  $L$ . While the sheet grows, the so-called ‘re-entrant jet’ flows underneath the cavitation sheet from its trailing to its leading edge. The up breaking cavitation volume forms a cavitation cloud showing a circulation which is determined by the developing process. After the cloud has separated the process starts again.

During the growth process, the furled cloud is observed in Fig. 3 a), b) and c) marked with the white lines. The cloud remains in the wake of the growing sheet cavitation, which can be seen by the stagnation of the rolled-up cloud. During this time period, the cloud is embossed a circulation.

The lower pressure in the vortex core leads to a decreasing of the static pressure, which is measured by a fast scanning pressure sensor installed at the channel wall 65 mm downstream of the smallest cross section area. On the other site the cloud collapse produces a pressure peak, which is also recorded and qualitatively shown in Fig. 3 f).

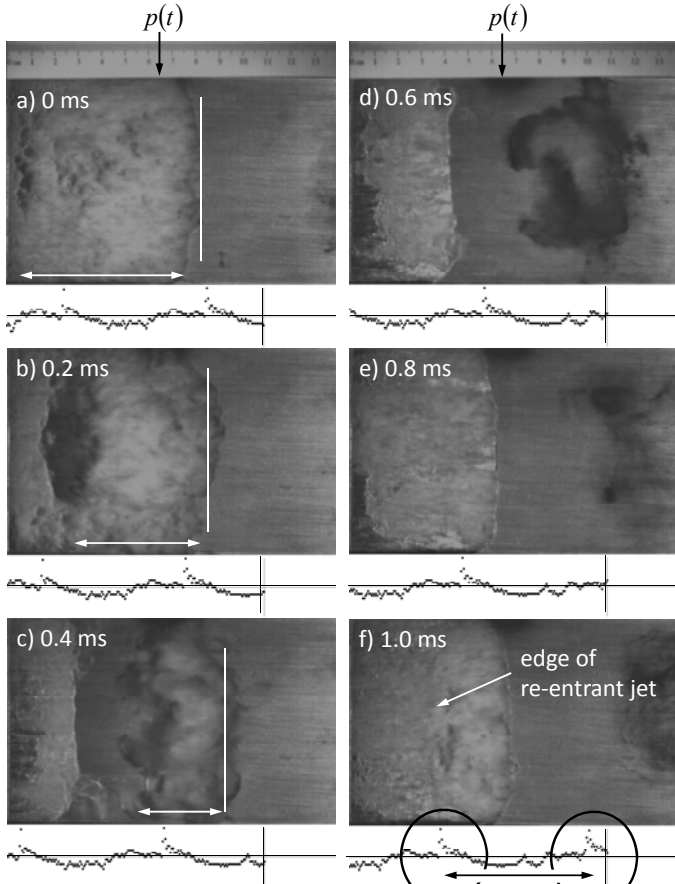


**Fig. 3:** High speed visualization for  $Re = 3.13e5$  and  $\sigma = 5.7$ . The actual pressure signal is shown in the diagram below the pictures.

The periodic behavior of the flow is visible from the pressure timeline shown in Fig. 3.

The Fourier transform of both time histories, i.e. position of the front and pressure, are shown in Fig. 4.

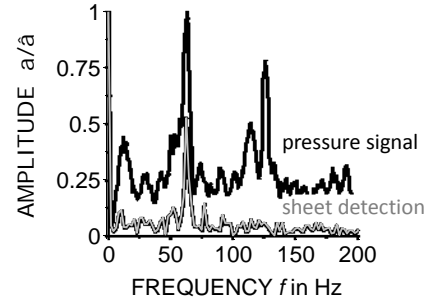


**Fig. 4:** -Fourier transform of the pressure history and the position of the sheet front.

The analysis of both signals show a clear typical frequency associated with the cloud shedding.

# Strouhal Number vs. Reynolds and Cavitation Number

Fig. 5 shows the Strouhal number (4) as a function of cavitation and Reynolds number.

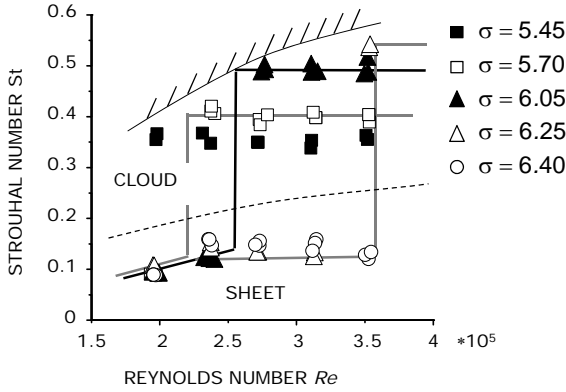


**Fig. 5:** Transition from sheet to cloud cavitation.

There are two characteristic flow regimes (shown in Fig. 5 and Fig. 6). For a given cavitation number there is a critical Reynolds number. (i) for Reynolds number smaller that critical value we observe sheet cavitation without cloud shedding. (ii) above that critical Reynolds number we observe cloud cavitation. The Strouhal number is in that case independent of the Reynolds number. Hence there should be no dependence on the size of the device in that flow regime.

A critical velocity was first described by Arndt [6]. Here we have the velocity made dimensionless by the kinematic viscosity and the channel height (i.e. Reynolds number).

For the highest cavitation number of 6.4 we could not observe a critical Reynolds number. (But there might be such a number outside the operation range of our test rig.)

By reducing the cavitation number at a given Reynolds number the sheet length increases until again a stability limit is reached. The transition is associated with a sudden increase of the Strouhal number to its maximum value at a given Reynolds number. The limiting curve is roughly indicated in Fig. 5 by the most upper line. A further reduction of the cavitation number leads to an enlargement of the sheet length and thus to a reduction in the Strouhal number. The decrease of the cavitation number finally leads to full cavitation (flashing) just above the dotted line in Fig. 5. The Fig. 6 shows the dependence of the Strouhal number on the cavitation number.

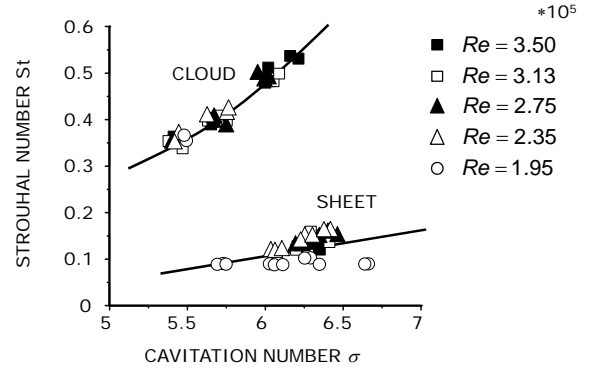


**Fig. 6:** Strouhal number vs. cavitation number.

Of course all the findings depend on the shape of the nozzle. Presumably on mayor parameter is the minimal radius of surface curvature, which is the main parameter to be changed for our future research.

## Sheet Length and Circulation of the Cloud

Fig. 7 shows the maximum sheet length  $L$  and Fig. 8 typical velocities characterized by the sheet cavitation as a function of the cavitation number. The Reynolds number has for cloud cavitation no influence as again Fig. 7 and Fig. 8 indicate.

These general results justify model test of pumps or turbines with respect to cloud cavitation!

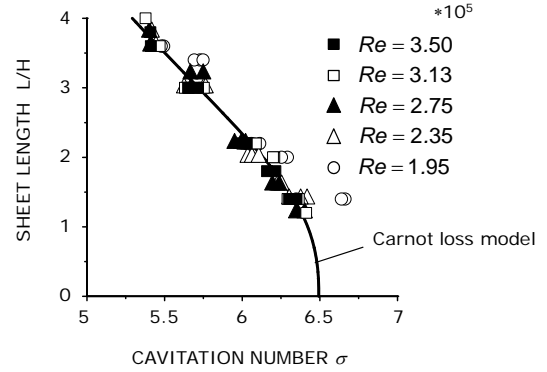


**Fig. 7:** Sheet length vs. cavitation number. The Reynolds number has no influence on the sheet length. The solid line indicates a Carnot loss model.

The growing size of the cavitation sheet for a decrease of the cavitation number causes a throttling of the flow. A simple fluid mechanical model based on Carnot's shock loss is sufficiently accurate to predict the experimental results (solid line in Fig. 7).

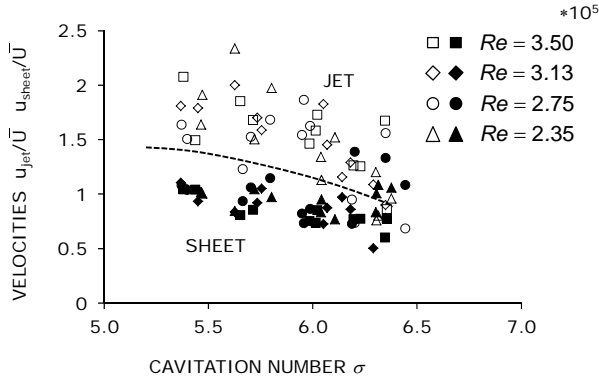


**Fig. 8:** Mean velocity of the growing sheet cavitation and the velocity of the re-entrant jet.

Fig. 8 shows the mean velocities of the sheet growth  $u_{\text{sheet}}/\bar{U}$  and of the re-entrant jet  $u_{\text{jet}}/\bar{U}$ .

The sheet and jet velocities are determined by means of the optical measurements and are time averaged velocities. As Fig. 8 shows, the velocities do not depend on the Reynolds number.

A second point to mention is the difference in the velocities. The difference cannot be explained by classical free-streamline theory. A third point to mention is the mean sheet velocity, being close to the velocity of the incoming flow. The mean flow velocity at the minimal cross section is by a factor of 2.5 higher than the sheet velocity. Again this difference is surprisingly large from a classical fluid mechanics point of view: We expected a sheet velocity of roughly 2.5.

To quantify the circulation, the closed integral over the sheet is evaluated by using the mean values of the determined velocities  $u_{\text{sheet}}$  and  $u_{\text{jet}}$ .

$$\gamma = \frac{\Gamma}{UH} = \frac{L}{H} \frac{u_{\text{sheet}} + u_{\text{jet}}}{U}. \quad (7)$$

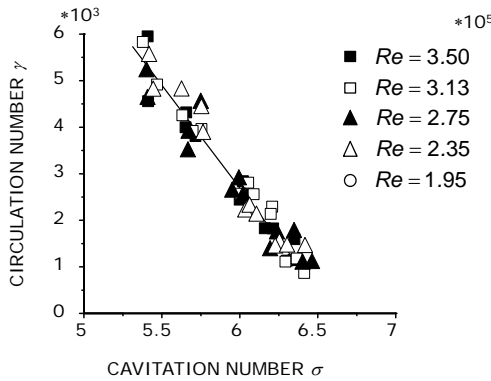


**Fig. 9:** Dimensionless circulation number vs. cavitation number.

An increased cavitation length, i.e. decreased cavitation number, results in an increased circulation numbers as shown in Fig. 9.

To summarize the results gained so far: As soon a critical Reynolds number is reached, there is a periodic cloud shedding

and the Reynolds number vanishes on the right hand side of (4), (5), (6):  $f\bar{U}/H = St(\sigma, \kappa_i)$ ,  $L/H = \lambda(\sigma, \kappa_i)$ ,  $\Gamma/\bar{U}H = \gamma(\sigma, \kappa_i)$ .

It is important to mention:

Our results justify the model test for pumps and turbines. Only the Reynolds number has to be for the model above the critical Reynolds number.

#### 4. PLASTIC DEFORMATION OF SOLID SURFACE DUE TO CLOUD CAVITATION

##### Automated Pit-Count System

Pit-count is a measurement principle to detect plastic deformations on polished metal surfaces developed at the Chair of Fluid Systems Technology by Lohrberg [9]. Curved surfaces are scanned by an all-in-focus algorithm. The surface is scanned before and after a cavitation experiment. By comparing the two scans, a filter algorithm is implemented to distinct between materials defects from pits, which are the result instable cavitation bubbles. Such a pit is shown in Fig. 10.

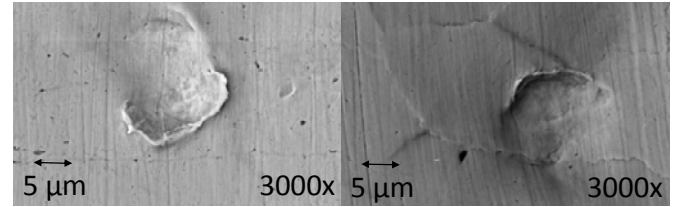


**Fig. 10:** Plastic deformations of a copper surface after 30 min and dislocation movements of gains after 300 min,  $\sigma = 0.112$

The pit-count software gives finally a damage map of the curved surface.

The creation of damage maps with a local damage distribution with known radius and position of all plastic deformation are possible. The damage energy can be calculated by using an empirical relationship developed and used by Lohrberg [9].

$$E = 9L_m^3 \sum \left( 1 + \frac{R_i}{l_m} \right)^3, \quad (8)$$

where  $\vartheta$  is the yield stress of the material,  $L_m$  and  $l_m$  are two material typical lengths.  $R_i$  is the pit radius.

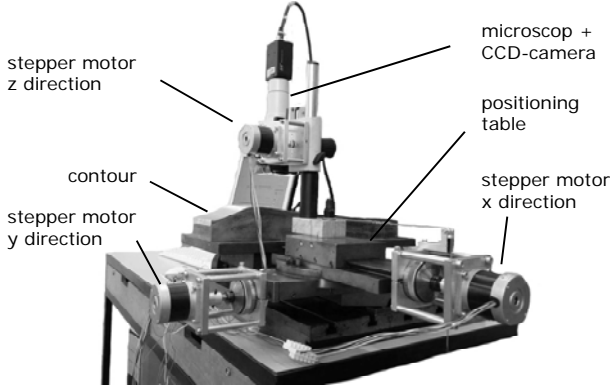


**Fig. 11:** Fully automated pit-count system at the Chair of Fluid Systems Technology.

#### Damage Maps

Pit count measurements are carried out for Reynolds numbers  $2.75e5$  and  $3.5e5$  and the cavitation numbers  $5.45$ ,  $5.7$ ,  $6.05$ . Fig. 5 shows those operation points to lay complete within the cloud regime.

Fig. 12 shows the damage maps for a Reynolds number of  $2.75e5$  and the three named cavitation numbers  $5.45$ ,  $5.7$ ,  $6.05$ . The exposure time  $T = 90\text{min}$  is made dimensionless by the shedding frequency. Thus  $fT$  gives the load cycles on the surface. The number of load cycles is given for each experiment in Fig. 12 (and Fig. 13).

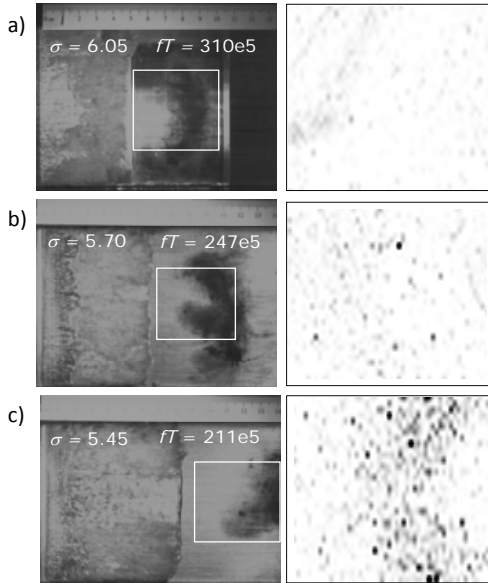


**Fig. 12:** Damage maps for the cavitation numbers  $5.45$ ,  $5.7$ ,  $6.05$  at a small Reynolds number of  $2.75e5$ .

As expected, a smaller cavitation number results in an increased cavitation zone and thus an increased damage during exposure time.

Fig. 13 shows the experimental results for the larger Reynolds number of  $3.5e5$ . The load cycles are again given within the pictures.

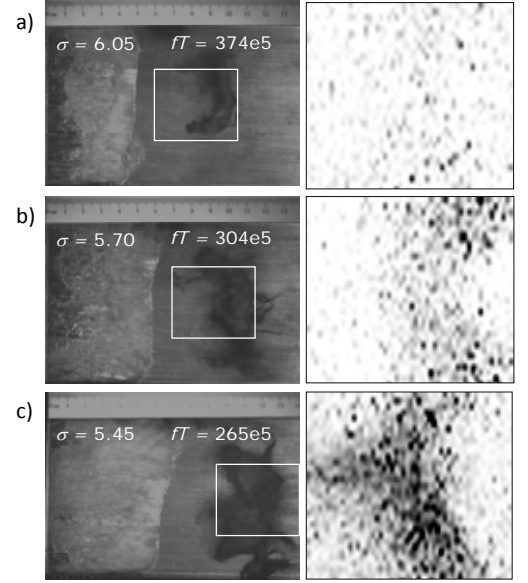


**Fig. 13:** Damage maps for the cavitation numbers  $5.45$ ,  $5.7$ ,  $6.05$  at a small Reynolds number of  $3.5e5$ .

To compare the experimental results the deformation energy is accumulated for the whole polished surface using the empirical relation (8) is calculated.

To make different flow conditions comparable, it has shown to be use full to normalize the deformation energy (9) as:

$$\frac{E}{\rho U^2 H^3 f T} = \pi(Re, \sigma, \kappa_i). \quad (9)$$

In order to compare the aggressiveness of operating points, the non-dimension energy is based on the number of damage cycles  $fT$  in Eq. (9). The result is shown in Fig. 14, were the accumulated dimensionless damage energy per cycle is given as a function of the cavitation number.

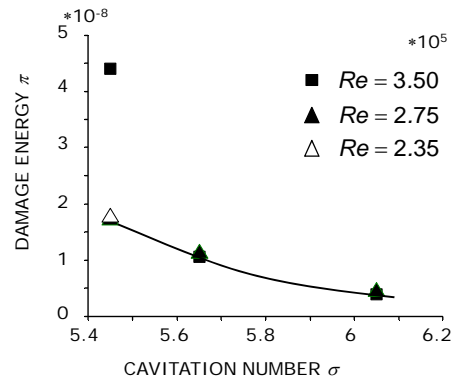


**Fig. 14:** Dimensionless damage energy per damage cycle.



Up to the point  $Re=3.5e5$  at the lowest cavitation number (see damage map shown in Fig. 13. c)), all results are on one line. To show the influence of the Reynolds number for small cavitation numbers an operating point for a Reynolds number at  $2.35e5$  is added in the measurement program.

Fig. 15 shows the first moment of the damage maps given in Fig. 12 and 13 normalized with the channel height.

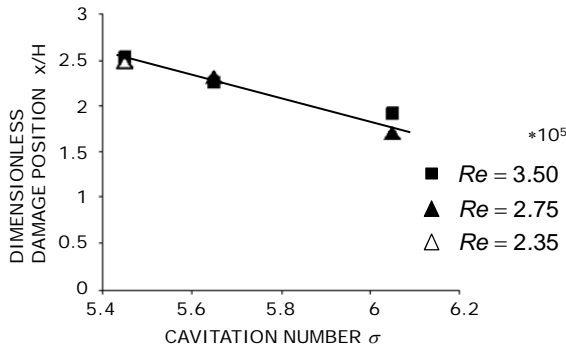


**Fig. 15:** Dimensionless damage position is independent of the Reynolds number but depends on cavitation number.

The damage position is primarily influenced by the cavitation number and thus by the sheet length.

## 5. CONCLUSIONS

For a convergent divergent nozzle, a critical Reynolds number is determined. For Reynolds numbers below that critical value sheet cavitation is observed. For Reynolds number above that critical value cloud cavitation is observed. The nozzle geometry is such, that the minimal radius of curvature can easily be changed. Up to now the radius of curvature was set to 2.5 times the channel height.

By optical measurements the largest scales of the cavitation phenomena were determined.

An upper limit for the Strouhal number was observed. That upper limit is dependent on the Reynolds number.

For the first time the circulation of clouds was determined.

Within the cloud regime there is no influence on the Reynolds number, which justifies model test of pumps and turbines.

A dimensionless damage function was defined and the plastic deformation of the material surface was determined as a function of cavitation number.

## ACKNOWLEDGMENTS

The presented results were obtained within the research project No. 16054 N/1, funded by budget resources of the Bundesministerium für Wirtschaft und Technologie (BMWi) approved by the Arbeitsgemeinschaft industrieller Forschungsvereinigungen "Otto von Guericke" e.V. (AiF).

## REFERENCES

- [1] Ida, M., *Investigation of transition frequencies of two acoustically coupled bubbles using a direct numerical simulation technique*, J. Phys. Soc. Jpn., 2004
- [2] Ida, M., *Multibubble cavitation inception*, J. Phys. Soc. Jpn., 2009
- [3] Konno, A., Kato, H., Yamaguchi, H., Maeda, M., *On the collapsing behavior of cavitation bubble clusters*, JSME International Journal, Series B, Vol. 45, No. 3, 2002
- [4] Kubota, A., Kato, H., Yamaguchi, H., *A new modelling of cavitating flows: a numerical study of unsteady cavitation on a hydrofoil section*, J. Fluid Mech. (1992), vol. 240, pp 59-96, 1992
- [5] Wang, Y.-C., *Shock Waves in bubbly cavitating flows; (Part I.) Shock Waves in Cloud Cavitation; (Part II.) Bubbly cavitating flows Through a converging-diverging nozzle*, California Institute of Technology Pasadena, California, 1996
- [6] Arndt, R.E.A., Hambleton, W.T., Kawakami, E., *Creation and maintenance of cavities under horizontal surfaces in steady and gust flows*, Journal of Fluid Engineering, Nov. 2009, Vol 131 /111301-1, 2009
- [7] Kawanami, Y., Kato, H., Yamaguchi, H., Maeda, M., Nakasumi, S., *Inner Structure of Cloud Cavity on a Foil Section*, JSME International Journal, Series B, Vol. 45, No 3, 2002
- [8] Jousellin, F., Delannoy, Y., Sauvage-Boutar, E., Goirand, B., *Experimental Investigations on Unsteady Attached Cavities*, Proc. ASME FED, Vol. 116 (1991), pp. 61-66
- [9] Lohrberg, H., *Messung und aktive Kontrolle der erosiven Aggressivität der Kavitation in Turbomaschinen*, Fortschritts-Bericht VDI Reihe 8 Nr. 942 ISBN 3-18-394208-5, 2001
- [10] Schmid, P.J., *Dynamic mode decomposition of numerical and experimental data*, J. Fluid Mech. (2010), vol. 656, pp. 5-28, 2010
- [11] Schmid, P.J., Li, L., Juniper, P., O., *Applications of the dynamic mode decomposition*, Theor. Comput. Fluid Dyn., DOI 10.1007/s00162-010-0203-9, 2009
- [12] Van Terwisga, Fitzsimmons, P.A., Ziru, L., Foeth, E.J., *Cavitation Erosion – A review of physical mechanisms and erosion risk models*, Proc CAV2009 – 7th International Symposium on Cavitation, Ann Arbor, 2009
- [13] Fortes Patella, R., Reboud, J.L., *Interaction between pressure waves and spherical cavitation bubbles: Discussion about cavitation erosion mechanism*, Proc. Of the 2000 ASME Fluids Engineering Summer Conference, Boston, Massachusetts, 2000
- [14] Fortes Patella, R., Challier, G., Reboud, J.L., Archer, A., *Cavitation erosion mechanism: numerical simulations of the interaction between pressure waves and solid boundaries*, Proc. CAV2001 International Symposium on Cavitation, Pasadena, 2001
- [15] Pelz, P., Keil, T., Bottenbender, J., *On the transient behavior of cloud cavitation*, SHF conference on Cavitation and Hydraulic Machines, Lausanne workshop, May 26-27 2011

## Simulation of Water Quality Effects for Cavitating Engineering Flows

Thierry Maquil\*  
Bahaddin Cankurt  
Thomas Rung

Institute for Fluid Dynamics and Ship Theory,  
Hamburg University of Technology, Germany

\*[thierry.maquil@tu-harburg.de](mailto:thierry.maquil@tu-harburg.de)

Moustafa Abdel-Maksoud  
Patrick Schiller  
Sergey Yakubov

[www.tu-harburg.de/fds](http://www.tu-harburg.de/fds)

Schwarzenbergstrasse 95, D-21073 Hamburg

### ABSTRACT

The paper is concerned with modelling water-quality effects in numerical simulations of cavitating engineering flows. Numerical cavitation predictions mostly employ mass-transfer models in the framework of VOF-based Euler-Euler simulations. Such cavitation models are restricted to a few global water properties and a simplified bubble dynamics. Additionally, they inhere empirical parameters which might be useful to support the predictive accuracy but are difficult to generalise. On the contrary, coupled Euler-Lagrange approaches allow to compute the evolution of the individual vapour bubble and offer enhanced prospects to mimic water-quality effects by means of the nuclei distribution in the approach flow. Moreover, the release of dissolved gas can be of importance for the generation of cavitation nuclei. The paper reports an attempt to analyse water-quality effects and compares results of Euler-Euler and Euler-Lagrange techniques against experiments for a NACA66(2)-415  $a = 0.8$  hydrofoil featuring constant chord. Examples included demonstrate the benefits of a more detailed Euler-Lagrange cavitation model.

### Nomenclatur

$\alpha$	vapour-volume fraction
$\rho, \mu$	density, viscosity
$\mathbf{u}, \mathbf{v}$	velocity vectors of the Euler & Lagrange phase
$p, p_{vap}$	pressure, vapour pressure
$l, v$	subscript referring to liquid, vapour
$R, D_b$	bubble radius, diameter
$\sigma$	cavitation number
$Re$	Reynolds number

### 1. INTRODUCTION

The influence of the water quality on cavitation inception and the behaviour of cavitating flows is of great importance for the interpretation of model tests and their extrapolation to full-scale. Water-quality aspects also occur when comparing model-scale results. Measurements of cavitation behaviour on the same model performed in different test facilities under identical hydrodynamic conditions can produce significantly different results [1,2]. The discrepancy can be attributed to the different water quality, i.e. the nuclei spectrum and the dissolved gas content of the approach flow, which is the focal point of the paper.

Engineering cavitation simulations using viscous CFD approaches are usually based on VOF-related Euler-Euler techniques [3]. VOF-methods are fairly popular for their efficiency. They consider the two-phase flow as a mixture of a liquid and vapour phase which share the kinematic field. The local vapour fraction is obtained from a transport equation conveying the immiscible properties of the involved phases. Cavitation physics is reduced to a modelled mass-transfer rate between water and vapour that occurs as a source in the volume-conservation equation. Such approaches do not take into account local (inhomogeneous) water properties and are restricted to simplified vapour-bubble dynamics. The mass-transfer models rely on empirical assumptions casted into the model parameters, e.g. vaporization and condensation coefficients. The respective parameter values are unfortunately not case-independent and interact with the employed computational scheme. Therefore, more sophisticated cavitation simulation techniques are of interest.

The current work reports the development of an improved cavitation-simulation model. Emphasis is given to the assessment of a two-way coupled Euler-Lagrange approach. Supplementary to an Eulerian mixture phase, separate equations for the size and the momentum are solved for a large number of cavitation nuclei/bubbles, composing the discrete vapour phase [4]. The Euler-Lagrange model has been implemented into an unstructured finite-volume Navier-Stokes solver and parallelised using an efficient hybrid MPI-OpenMP algorithm. The novelty of the present approach refers to the application of fully-coupled Euler-Lagrange technique to turbulent engineering flows. The strategy allows to account for inhomogeneous and transient water-quality effects such as nuclei spectra and variable non-condensable gas content.

The work forms part of the numerical and experimental research initiative KonKav-I. It involves two universities (University of Rostock, TUHH) and two model basins (SVA Potsdam, HSVA Hamburg) and aims at the investigation of water-quality influences on cavitating flows. Displayed comparisons between computed and measured results refer to experimental studies jointly performed by SVA Potsdam, HSVA Hamburg and the University of Rostock for constant chord (2D) variants of a NACA66(2)-415  $a = 0.8$  hydrofoil.

## 2. COMPUTATIONAL MODEL

Results of the present study were obtained from the Navier-Stokes procedure FreSCo+ [5] which is jointly developed by Hamburg Ship Model Basin (HSVA) and the Institute for Fluid Dynamics and Ship Theory (FDS) at Hamburg University of Technology (TUHH). The procedure uses a segregated algorithm based on the strong conservation form of the momentum equations. It employs a cell-centred, collocated storage arrangement for all transport properties. Structured and unstructured grids, based on arbitrary polyhedral cells or hanging nodes, can be used. The implicit numerical approximation is second-order accurate in space and time. Integrals are approximated using the conventional mid-point rule. The solution is iterated to convergence using a pressure-correction scheme. Various turbulence-closure models are available with respect to statistical (RANS) or scale-resolving (LES, DES) approaches. Two-phase flows are addressed by interface-capturing methods based upon the Level-Set or Volume-of-Fluid (VOF) technique. Since the data structure is generally unstructured, suitable pre-conditioned iterative sparse-matrix solvers for symmetric and non-symmetric systems (e.g. GMRES, BiCG, QMR, CGS or BiCGStab) can be employed. Cavitation is modelled using either mass-transfer models – i.e. Sauer [3], Zwart et al. [6], Singhal et al. [7], Senocak [8], Wu et al. [9] – or two-way coupled Euler-Lagrange approaches. The method is parallelised using a domain-decomposition technique based on a Single Program Multiple Data (SPMD) message-passing model. Inter-processor communication employs the MPI communications protocol. For Euler-Lagrange simulation a hybrid MPI/OpenMP parallelisation strategy is applied. Load balancing is achieved using ParMETIS partitioning software. The dynamic decomposition of the particles follows the Eulerian background phase.

### 2.1. EULERIAN MIXTURE PHASE

The Eulerian mixture phase is described by the standard Navier-Stokes equations

$$\begin{aligned} \frac{\partial \rho}{\partial t} + \nabla \cdot (\rho \mathbf{u}) &= 0, \\ \frac{\partial \rho \mathbf{u}}{\partial t} + \mathbf{u} \cdot \nabla (\rho \mathbf{u}) &= -\nabla p + \nabla \boldsymbol{\tau} + \mathbf{f}, \end{aligned}$$

whereby  $\rho$  denotes the density of the mixture,  $\mathbf{u}$  the mixture-velocity vector,  $p$  the pressure and  $\boldsymbol{\tau}$  the viscous stress tensor which is composed from modelled turbulent and laminar contributions. The mixture is composed from two incompressible immiscible phases. The mixture state is computed from the volume fraction. For a two-phase flow with water ( $l$ ) and vapour ( $v$ ), the vapour-volume fraction yields

$$\alpha = \frac{V_v}{V_v + V_l} \in [0,1].$$

Hence,  $\alpha = 0$  [1] denotes to a control volume filled with water [vapour]. Notice that values outside  $\alpha \in [0,1]$  describe non-physical situations. The mixture properties are computed as a weighted sum of the partial properties of the different phases, viz.

$$\rho = \alpha \rho_v + (1 - \alpha) \rho_l, \quad \mu = \alpha \mu_v + (1 - \alpha) \mu_l.$$

A modified SIMPLE pressure-correction method as described by Sauer [3] is used for the Eulerian mixture phase in cavitating flows. The algorithm is sensitized to non-realizable vapour-

volume fractions and aims to drive the vapour fraction back into its admissible bounds. Two strategies are employed to determine the mixture fraction, i.e. Euler-Euler and Euler-Lagrange approaches.

### 2.2. EULERIAN VAPOUR PHASE

Within the Euler-Euler approach, the vapour-volume fraction is computed from an additional transport equation, viz.

$$\frac{\partial \alpha}{\partial t} + \nabla \cdot (\alpha \mathbf{u}) = S_{cav}.$$

The source term describes the volume transfer between liquid and vapour and inheres the modelling part. Several (similar) models for the source term have been published, among other Zwart [6] proposes the following formula

$$S_{cav} = \begin{cases} F_{vap} \frac{3\alpha_{nuc}(1-\alpha)}{R_0} \dot{R} & \text{(vaporisation)} \\ F_{cond} \frac{3\alpha}{R_0} \dot{R} & \text{(condensation)} \end{cases},$$

whereby  $R$  denotes the radius of a representative spherical vapour bubble and  $F_{vap}$  &  $F_{cond}$  are two empirical constants. The nucleation site volume fraction  $\alpha_{nuc}$  and the corresponding nucleation site radius  $R_0$  are two water-quality parameters which have to be assigned to constant values. The rate of change of the bubble radius is generally defined via a simplified Rayleigh-Plesset (R.-P.) equation. The latter only considers the most crucial contribution to vaporization and condensation, i.e. the pressure difference between local and vapour pressures

$$\dot{R} = \sqrt{\frac{2}{3} \frac{p - p_{vap}}{\rho_l}}.$$

Singhal [7] proposes several corrections to improve the model in line with turbulence and non-condensable gas. The influence of turbulence is considered via an increase of the vapour pressure due to turbulence energy ( $p_{vap}^* = p_{vap} + 0.2 \rho k$ ). Non-condensable gas influences can be considered through a constant free-air fraction. The mixture is henceforth composed from three phases and the properties are determined accordingly, e.g.

$$\rho = \alpha_v \rho_v + \alpha_l \rho_l + \alpha_g \rho_g.$$

A further improvement of the Euler-Euler approach is to consider a variable (inhomogeneous) state of the non-condensable gas ( $NCG$ ). Accordingly, the  $NCG$  is sub-divided into dissolved and free gas

$$\rho_{NCG} = \rho_{dis} + \rho_g.$$

When no additional gas can enter or leave the system, the amount of non-condensable gas is conserved and only one additional transport equations is necessary, e.g. for the free-gas fraction

$$\frac{\partial \alpha_g}{\partial t} + \nabla \cdot (\alpha_g \mathbf{u}) = S_{sorp},$$

$$S_{sorp} = \begin{cases} C_{abs} \frac{\Delta p}{p_{\infty} t_{\infty}} \left( f_{NCG} \frac{\rho}{\rho_{NCG}} - \alpha_g \right) \alpha_{dis} & \text{(absorption)} \\ C_{des} \frac{\Delta p}{p_{\infty} t_{\infty}} \left( f_{NCG} \frac{\rho}{\rho_{NCG}} - \alpha_{free} \right) \alpha_g & \text{(desorption)} \end{cases},$$

whereby the source term describes the transfer between the dissolved- and free-gas fraction. This source term is mainly driven by the pressure difference between the local and the equilibrium pressures determined by Henry's law [10].

### 2.3. LAGRANGIAN VAPOUR PHASE

The Euler-Lagrange approach determines the vapour-volume fraction  $\alpha$  from the bubbles residing inside a control volume. The vapour bubbles are assumed to be spherical. The trajectory of a bubble can be described by the equations of motion [11]

$$\begin{aligned} \frac{d \mathbf{x}}{d t} &= \mathbf{v} , \\ m_b \frac{d \mathbf{v}}{d t} &= (m_b - m_f) \mathbf{g} + m_f \frac{d \mathbf{u}}{d t} \\ &\quad - 0.5 m_f \left( \frac{d \mathbf{u}}{d t} - \frac{d \mathbf{v}}{d t} \right) + \mathbf{F}_D + \mathbf{F}_L + \mathbf{F}_V , \end{aligned}$$

whereby  $m_b$  is the bubble mass,  $m_f$  is the equivalent mass of the mixture phase. The Euler-Lagrange approach features two velocity fields, i.e. the bubble velocities  $\mathbf{v}$  and the mixture velocities  $\mathbf{u}$  (interpolated to the present centre of the bubble). The terms on the right-hand side refer to the forces due to buoyancy, fluid acceleration and added mass. The three last terms  $\mathbf{F}_D$ ,  $\mathbf{F}_L$ ,  $\mathbf{F}_V$  denote to the drag, lift and volume variation forces.

The Rayleigh-Plesset equation is used to compute the diameter and allows to determine the transient evolution of the bubble diameter. Hsiao [12] proposes an extended R.-P. equation accounting the effect of the slip velocity between the bubble and the Euler phase

$$R\ddot{R} + \frac{3\dot{R}^2}{2} = \left[ \frac{p_{vap} + p_g - p_\infty}{\rho_f} - \frac{2\sigma + 4\mu\dot{R}}{\rho_f R} \right] + \frac{(\mathbf{u} - \mathbf{v})^2}{4} .$$

In this equation  $\sigma$  refers to the surface tension and  $\mu$  to the dynamic viscosity. The Euler-Lagrange simulations are computationally demanding due to the large number of required nuclei. Computations are greatly supported by high-performance computing hardware which required the introduction of hybrid MPI/OpenMP parallelization strategies [13]. Mind that the bubbles do not interact with each other but with the Eulerian mixture field. Thus, thread-parallel structures are used to speed up the Lagrangian part for each MPI process and the decomposition of the bubbles is governed by their location.

### 2.4. EULER-LAGRANGE COUPLING

The solution advances in time by alternating between the two building blocks, i.e. Eulerian mixture phase and discrete Lagrangian vapour phase, in a symplectic manner. Due to the explicit coupling in time, the Eulerian time step is restricted to Courant numbers below one, even though the Eulerian part is fully implicit. Moreover, the fully explicit Lagrangian part is itself restricted to much smaller time steps, since the respective time-step limitations from the various right-hand side terms are more severe. The time step of the Lagrangian scheme usually falls two orders of magnitude below the Eulerian time steps, thus the bubbles are advanced in time for a couple of hundred subsequent Lagrangian steps after the Eulerian field is advanced. Cavitation nuclei – which need to be initialised – are continuously introduced to the Eulerian field at each Eulerian time steps in release planes upstream of the cavitation zones.

Another aspect refers to load unbalancing due to severe clustering of rather small bubbles in Eulerian sub-domains, e.g. in recirculation regimes. Accordingly, bubbles are grouped if the respective control volumes are overcrowded.

A mapping routine is employed to project the bubbles into the Eulerian grid. Moreover, a smoothing operation based upon a normalized, compact-support smoothing function  $W$  is utilized to obtain smoothed mapping of the Lagrangian bubble volumes  $V_b$  to the Eulerian vapour volume  $V_v$  in line with suggestions of [14]

$$V_v = \frac{\int V_b(r) W(r) dr}{\int W(r) dr} .$$

Here  $r$  denotes the distance between the bubble centre and the centre of the control volume. The smoothing function  $W$  is a typical bell-shaped kernel function, for example a clipped Gaussian. Subsequently, a redistribution of excessive vapour content to the neighbouring cells is performed for all cells – where each neighbour receives the same contribution – and the resultant vapour content is clipped to the admissible limits.

### 3. INVESTIGATED TEST CASE

Results of the present study refer to hydrofoil investigations performed in the K15a cavitation tunnel of SVA Potsdam and the K22 tunnel of HSVA Hamburg. The constant chord (2D) hydrofoil uses the base profile of a 3D hydrofoil introduced by Arndt [1]. The section shape corresponds to a NACA66(2)-415 with  $a = 0.8$  profile. The foil has a chord of  $c = 0.2025$  m and the span extends over the whole lateral width of the tunnels. A key aspect of the KonKav-I initiative is the acquisition of experimental benchmark data for reference geometries in different cavitation tunnels.

Measured data should facilitate the establishment of correlations between cavitation behaviour and water-quality aspects. Accordingly, hysteresis loops for incidence angles and cavitation numbers were measured for three different air contents. Supplementary, Reynolds number effects are investigated for fixed cavitation numbers at different velocities. The present study is however restricted to the analysis of one case at the following hydrodynamic conditions:  $10^\circ$  angle of attack at a cavitation number of  $\sigma = 3.0$  and a Reynolds number of  $Re = 0.89 \cdot 10^6$ . Next to numerical aspects, the research also involves an improvement of optical measurement techniques to assess the water quality and the cavitation behaviour with high precision, which is beyond the scope of the paper.

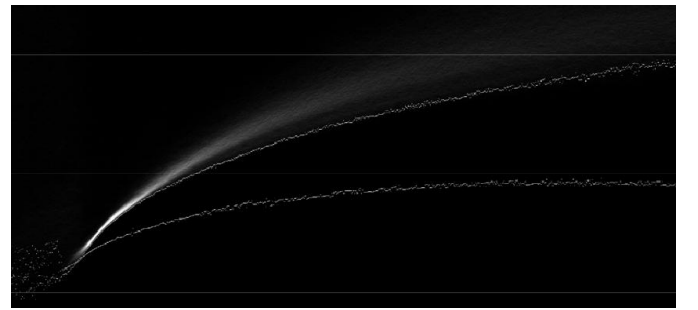


Fig.1 Result of the shadow-imaging technique for a longitudinal section of the investigated cavitating hydrofoil provided by University of Rostock. ( $AoA = 10^\circ$ ,  $\sigma = 3.0$ ,  $Re = 0.89 \cdot 10^6$ ).

Computational results are compared with experimentally observation of the cavitation thickness and the cavitation extent as displayed by shadow-imaging methods. Figure 1 shows an example of the experimental results. The white dots mark the

position at which sharp edges (bubble is this plane) are located, the lower thin line represents the shape of the profile and the upper thin line defines the upper bound of the experimentally observed vapour regime.

The water quality is defined by the bubble distribution and the measured value of the oxygen content. The latter is commonly labelled air content and measured with dissolved oxygen sensor. The bubble distribution is determined by Phase-Doppler (PD) [15] measurements. Bubble sizes with a diameter between 10  $\mu\text{m}$  and 500  $\mu\text{m}$  can be identified. The phase Doppler technique assumes spherical bubbles. Because of few non-spherical bubbles and solid particles, the measured size distributions have to be corrected. For a reliable estimation of the bubble size distribution a new correction procedure was developed by the Institute of General Electrical Engineering from University of Rostock and applied to the phase Doppler raw data.

### 3.1. COMPUTATIONAL SET-UP

Transient simulations were performed using a time step which restricts the Courant number for the Eulerian part of the Euler-Lagrange method below one. The same time step has also been used for the Euler-Euler approach for the sake of consistency. Cavitating simulations are started from the results of a converged non-cavitating simulation. The Wilcox  $k\text{-}\omega$  turbulence model [16] is used to model turbulence. Convective fluxes were approximated using monotonicity preserving third-order upwind-biased face interpolations for all transport properties. In conjunction with the Euler-Euler approach the mass-transfer models of Zwart [6] and Sauer [3] were employed. Accordingly different parameter variations were analysed. The Euler-Lagrange simulations were performed with different nuclei distributions.

A structured, two-dimensional mesh around the investigated hydrofoil (cf. Figure 2) was generated using the ICEM CFD mesh generation software. The computational domain spans 3 chords upstream of the hydrofoil and 6 chords in downstream direction. The height of the domain corresponds to the height of both employed cavitation tunnels ( $h = 600 \text{ mm}$ ). The blocking structure of the  $80 \cdot 10^3$  cells mesh uses a C-grid around the hydrofoil embedded in H-blocks for the far field. The hydrofoil surface is resolved by 230 cells using a local refinement at the leading edge.

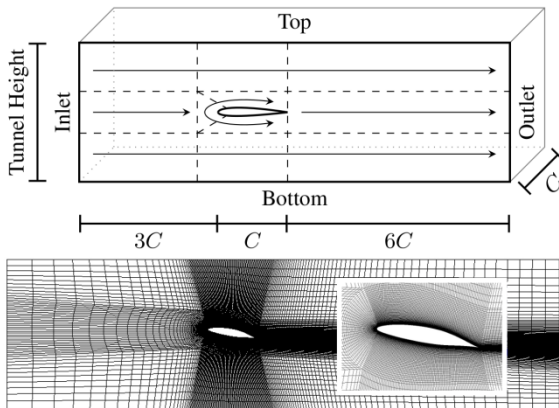


Fig.2 Blocking strategy and details of the employed computational mesh.

A uniform velocity is used at the inflow boundary. The inlet velocity is assigned to 5.5 m/s. At the outlet boundary a uniform pressure was specified matching the given cavitation number. The vapour pressure is set to  $p_{\text{vap}} = 2340 \text{ Pa}$ . The grid was built for the use of wall functions with  $Y^+ \approx 30$  around the hydrofoil. Supplementary, slip-wall boundary conditions were used along the tunnel walls (top/bottom) and symmetry boundary conditions were applied on the lateral sides. The water properties were assigned to  $\rho = 1000 \text{ kg/m}^3$  and  $\mu = 8.9 \cdot 10^{-4} \text{ Pa} \cdot \text{s}$ . The respective vapour properties were  $\rho = 0.026 \text{ kg/m}^3$  and  $\mu = 1.0 \cdot 10^{-5} \text{ Pa} \cdot \text{s}$ .

### 3.2. CAVITATION NUCLEI SPECIFICATION

A key aspect of the cavitation predictions of the Euler-Lagrange model is the number and initial size of the introduced nuclei per time unit. Moreover the nuclei-release location is of significance. FreSCo+ offers the possibility to continuously introduce spherical nuclei in a predefined area. The released nuclei feature either a constant radius or a radius defined by a predefined/measured distribution. The exact location at which the bubbles are released inside the release area is randomly computed. For the positioning of the nuclei-release area, the non-cavitating simulation is analysed and streamlines passing through pronounced low-pressure regions are traced upstream. The release area is positioned at a certain upstream distance in a high-pressure regime. In 2D cases the area is restraint to a line, in 3D cases the area consists of a surface. Figure 3 shows the scenario for the investigated hydrofoil case. The bubbles are released along a line which is 0.025 chords long. The line is positioned roughly 0.1 chords ahead the hydrofoil's leading edge. The initial velocity of the nuclei is assigned to the local Eulerian flow speed.

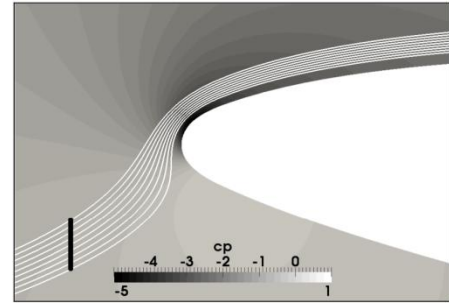


Fig.3 Illustration of the nuclei-release area.

The analysis of the water-quality influence follows two major routes: firstly, the released vapour-volume rate is kept constant and the bubble distribution by means of the released nuclei per time unit  $n$  and their diameter  $D_b$  is varied. Secondly, the released vapour volume is changed by increasing or decreasing the number of released nuclei maintaining a constant average initial diameter  $D_b$ . A typical size distribution for the bubble diameter measured in the K22 tunnel of HSVA is depicted by Figure 4 and serves as reference. The distribution was measured in an empty tunnel at a bulk velocity of 5.5 m/s and  $\sigma = 3.0$ . It is seen that the bubble diameter varies between 10 and 250  $\mu\text{m}$ , whereby the bubble number increases for smaller bubbles.



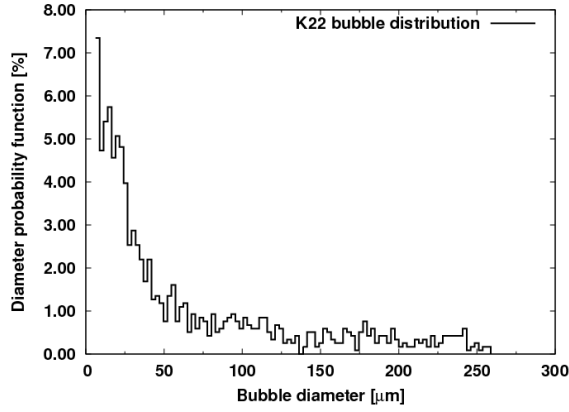


Fig.4 Bubble diameter probability distribution (K22 tunnel,  $\sigma = 2.00$ ,  $Re = 0.89 \cdot 10^6$ ).

#### 4. RESULTS

The hydrofoil is computed with Euler-Euler and Euler-Lagrange cavitation models. Different bubble initialisations were investigated for the Euler-Lagrange model. Table 1 summarises the different nuclei-release rates and initial diameters analysed by the Euler-Lagrange model.

Table 1. Summary of initial parameters and predicted cavitation extent for the investigated Euler-Lagrange cases.

Case	$n$ [1/s]	Vapour-vol. rate	$D_b$ [ $\mu\text{m}$ ]	Cavitation extent [mm]
E.L.(a)	10000	$\dot{V}_1$	158.4 (const.)	38.0
E.L.(b)	30000	$\dot{V}_1$	91.5 (const.)	18.0
E.L.(c)	100000	$\dot{V}_1$	50.1 (const.)	30.0
E.L.(d)	300000	$\dot{V}_1$	28.9 (const.)	4.5
E.L.(e)	30000	$\dot{V}_1$	Distribution1	37.0
E.L.(f)	10000	$\dot{V}_1$	Distribution1	34.0

Euler-Euler computations were performed with the Sauer [3] and Zwart [6] models. The Sauer model was employed as originally proposed, using  $n_0 = 10^8$  nuclei and an initial bubble diameter of  $D_b = 60 \mu\text{m}$ . Changing these parameters yields minor variations of the cavitation behaviour. For the Zwart model the two empirical model constants,  $F_{vap}$  and  $F_{cond}$ , were varied as indicated in Table 2.

Figure 5 shows the results of Euler-Euler simulations. The images display contour plots of the vapour-volume fraction. The black line indicates the experimentally evaluated cavitation thickness as reported by the shadow-imaging method. Displayed results refer snapshots at converged state and constant total vapour-volume fraction. The Sauer model returns only a very small cavitation regime which extents 14.5 mm in downstream direction. Results obtained for the E.E.Zwart(a) model agree with the predictions of the Sauer model and improve with increasing model constants. Notice that a further increase of the constants is not possible as the convergence deteriorates.

Table 2. Summary of model parameters and predicted cavitation extent for the investigated Euler-Euler cases using the Zwart et al. [6] model.

Case	$F_{vap}$	$F_{cond}$	Cavitation extent [mm]
E.E. Zwart (a)	5	0.001	11.5
E.E. Zwart (b)	25	0.005	21.0
E.E. Zwart (c)	50	0.010	29.0

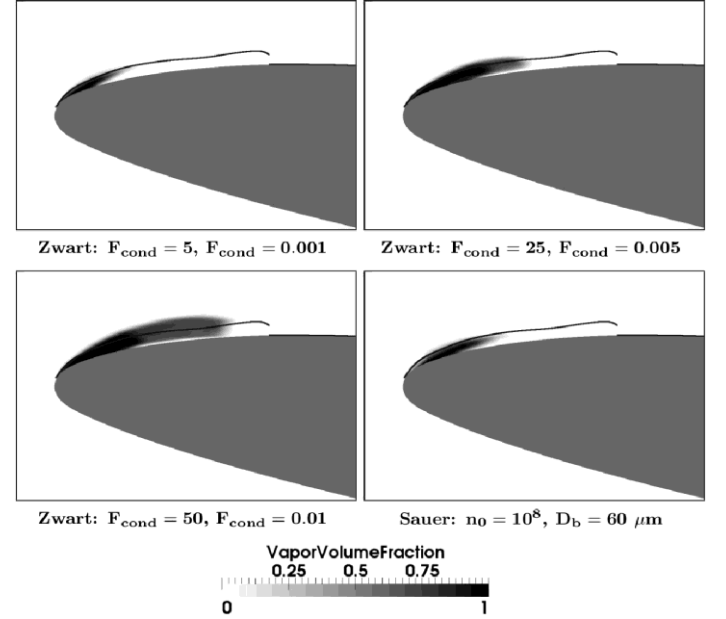


Fig.5 Euler-Euler simulation results for the NACA66(2)-415  $a = 0.8$  hydrofoil ( $AoA = 10.0^\circ$ ,  $\sigma = 3.00$ ,  $Re = 0.89 \cdot 10^6$ ).

Figure 6 depicts contour plots of the free-gas computed with a variable non-condensable gas formulation for Euler-Euler simulations with the Sauer model. It can be seen that dissolved gas is released as free gas in the low-pressure region at the leading edge. Contrary to the vapour region which disappears after the low pressure region, free gas survives even at higher pressure regions.

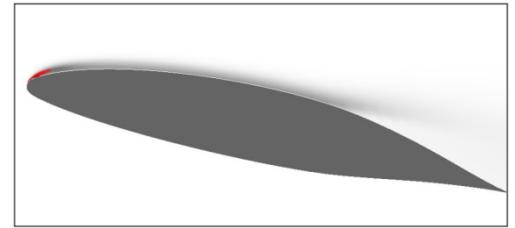


Fig.6 Release of free gas above the NACA66(2)-415  $a = 0.8$  hydrofoil ( $AoA = 10.0^\circ$ ,  $\sigma = 3.00$ ,  $Re = 0.89 \cdot 10^6$ ).

Figure 7 presents selected results of the Euler-Lagrange simulations by means of snapshots at steady vapour-volume fraction state. The contour plots indicate the vapour-volume fraction. Red spheres denote to scaled bubbles. Again the black lines describe the experimentally recorded cavitation zone. The Euler-Lagrange simulations show more fluctuations in the

cavitation size and area than the Euler-Euler simulations and thus reproduce a more realistic behaviour.

The analysis of different bubbles diameters at constant total vapour volume reveals a remarkable sensitivity of cavitation behaviour to the bubble size. When attention is given to constant-diameter bubbles shown in the top row of Figure 7, the cavitation extent increases with the bubble diameter. However, even for the large bubble diameter of  $91.54 \mu\text{m}$  the predicted cavitation extent falls below the experimentally observed vapour volume.

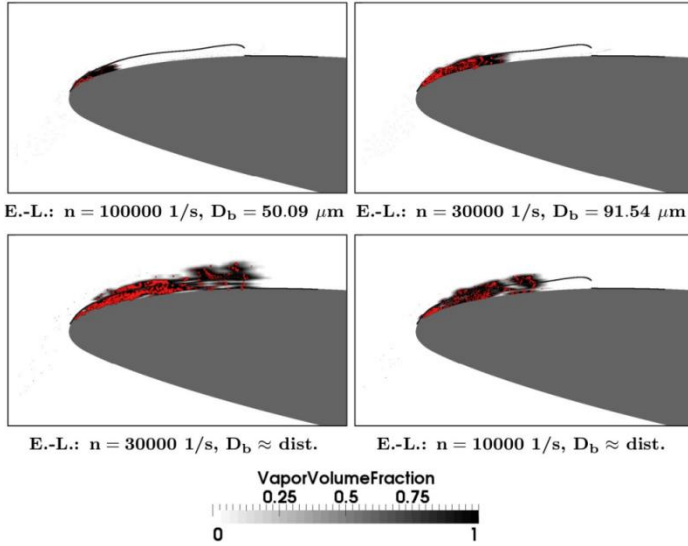


Fig.7 Euler-Lagrange simulation results for the NACA66(2)-415  $a = 0.8$  hydrofoil ( $AOA = 10.0^\circ$ ,  $\sigma = 3.00$ ,  $Re = 0.89 \cdot 10^6$ ).

The Euler-Lagrange simulations with the measured bubble distribution depicted in the left bottom graph of Figure 7 are closest to the experimental results. The cavitation extent and the cavitation thickness are in fair agreement with the experimental results indicated by the black line of the shadow-imaging method. Notice that the released vapour-volume is the same as for the simulations with constant bubble diameter displayed in the top row of Figure 7. This confirms that the correct diameter distribution is necessary to accurately predict the cavitation behaviour.

The variation of the total released vapour amount provides results which are in line with the expectations, i.e. less vapour volume leads to a smaller cavitation extent.

## 5. CONCLUSIONS

Cavitation simulations have been performed with Euler-Euler and Euler-Lagrange approaches. Emphasis is given to modelling water-quality issues. The Euler-Euler approaches require case-dependent coefficients to reproduce the correct cavitation behaviour. The coefficients are however not related to any water-quality parameter. The Euler-Lagrange revealed clear prospects to mimic water-quality effects. Euler-Lagrange simulations based upon the measured bubble spectrum outperformed the corresponding simulations with the same vapour volume using a constant bubble diameter and provided a fair predictive accuracy. Moreover, the parameter study displayed a severe dependency of the predicted cavitation

behaviour on the initiated bubble spectrum. In a next step the variable non-condensable gas model which can simulate different free-air contents will be coupled with the Euler-Lagrange approach using the free gas as an additional source of nuclei.

## ACKNOWLEDGEMENT

The project is funded by the German Federal Ministry of Economics and Technology under the aegis of the BMWi-project KonKav-I within the framework program “Schiffahrt und Meerestechnik für das 21. Jahrhundert”. Experimental results were kindly provided by Hamburg Ship Model Basin (HSVA), by Potsdam Model Basin (SVA) and by the Institute for General Electrical Engineering of the University of Rostock. Simulations were performed on the HLRN-II supercomputer system at the North German Cooperation for High-Performance computing (HLRN). This support is gratefully acknowledged by the authors.

## REFERENCES

- [1] R.E.A. Arndt and C. Dugue. Recent advances in tip vortex cavitation research. In International Symposium on Propulsors and Cavitation, volume STG 3007, page 142-149. Schiffbautechnische Gesellschaft e.V., 1992.
- [2] A.P. Keller. Cavitation scale effects empirically found relations and the correlation of cavitation number and hydrodynamic coefficients. In CAV2001, 2001.
- [3] J. Sauer. Instationär kavitierende Strömungen - Ein neues Modell, basierend auf Front Capturing (VoF) und Blasendynamik. PhD thesis, Universität Karlsruhe, 2000.
- [4] M. Abdel-Maksoud, D. Hänel, and U. Lantermann. Modelling and computation of cavitation in vortical flow. Int. J. of Heat and Fluid, 31:1065 – 1074, 2010.
- [5] Rung, T., Wöckner, K., Manzke, M., Stück, A., Brunswig, J., Ulrich, C. Challenges and Perspectives for Maritime CFD Applications Jahrbuch der Schiffbautechnischen Gesellschaft (Vol. 103), 2009.
- [6] P.J. Zwart, A.G. Gerber, and T. Belamri. A two-phase flow model for predicting cavitation dynamics. In ICMF 2004 International Conference on Multiphase Flow, number 152, Yokohama, Japan, 2004.
- [7] A.K. Singhal, M.M. Athavale, H. Li, and Y. Jiang. Mathematical basis and validation of the full cavitation model. Journal of Fluids Engineering, 124:617–624, September 2002.
- [8] I. Senocak. Computational Methodology for the Simulation of Turbulent Cavitating Flows. PhD thesis, University of Florida, 2002.
- [9] J. Wu, G. Wang, and W. Shyy. Time-dependent turbulent cavitating flow computations with interfacial transport and filter-based models. International Journal of Numerical Methods in Fluids, 49:739761, 2005.
- [10] J.-P. Franc and J.-M. Michel. Fundamentals of Cavitation, volume 76 of Fluid Mechanics and its Applications. Kluwer Academic Publishers, 2004.
- [11] G.F. Oweis, I.E. van der Hout, G. Tryggvason, and S.L. Ceccio. Capture and inception of bubbles near line vortices. Phys. Fluids, 17:022105, 2005.

- [12] C.-T. Hsiao, G. Chahine, and H.-L. Liu. Scaling effects on bubble dynamics in a tip vortex flow: Prediction of cavitation inception and noise. Technical report, Dynaflo, Inc., 2000.
- [13] S. Yakubov, B. Cankurt, M. Abdel-Maksoud and T. Rung. Hybrid MPI/OpenMP parallelization of an Euler-Lagrange approach to cavitation modelling, Parallel CFD conference, 2011.
- [14] D. Darmana, N. G. Deen, and J. A. M. Kuipers. Parallelization of an Euler-Lagrange model using mixed domain decomposition and a mirror domain technique: Application to dispersed gas-liquid two-phase flow. *J. Comput. Phys.*, 220:216–248, 2006.
- [15] Albrecht H-E, Borys M, Damaschke N, and Tropea C. *Laser Doppler and Phase Doppler Measurement Techniques*. Springer-Verlag 2003.
- [16] D.C. Wilcox. Turbulence modeling for cfd. In *DCW Industries, Inc.*, 2nd edition, number 152, Yokohama, Japan, 2004.

## The myth of the re-entrant jet

M. Hoekstra

MARIN, Wageningen, The Netherlands

m.hoekstra@marin.nl

### ABSTRACT

The re-entrant jet flow model is one of the options of wake closure in the Helmholtz/Kirchhoff free-streamline theory. It is a mathematically consistent steady flow model, without a physical equivalent because mass is not conserved. However, since numerous experimentalists have reported a liquid stream penetrating under a sheet cavity which they have identified as a re-entrant jet, it has played an important role in the discussion of dynamic cavitation behaviour. It is said to be responsible for the dynamic behaviour by impinging on the forward end of the cavity, upon which the cavity breaks and a vapour cloud is shed. In this paper we use numerical flow simulations to show that the re-entrant jet model is not an adequate description of the phenomena occurring, in spite of the apparent experimental evidence. These simulations have been carried out for the NACA0015 foil at 6 degrees angle-of-attack, i.e. a flow free of boundary layer separation in non-cavitating conditions. We demonstrate that partial cavitation soon after the inception phase invokes flow separation. Partial cavitation is therefore as a rule accompanied with a flow recirculation zone. This flow recirculation zone is present while the cavity is more or less stationary as well as during the major part of a shedding cycle in dynamic conditions. For developed shedding, the flow separation zone is swept from the suction side of the foil during each cycle. The flow phenomena found under dynamic conditions have therefore significant similarity with dynamic stall phenomena. The paper concludes that the story of the re-entrant jet as it has repeatedly been described in the literature on dynamic cavitation is very likely based on a visual illusion. Experimentalists are advised to reconsider and re-interpret their observations and results with a more realistic model of the underlying flow.

### NOMENCLATURE

$c$	chord length
$C_p$	pressure coefficient
$p$	pressure
$p_v$	saturated vapour pressure
$\alpha_v$	vapour volume fraction
$\rho$	density
$\rho_v$	density of vapour
$\rho_l$	density of water
$\sigma$	cavitation number

### 1. INTRODUCTION

Our concern is cavitation in flowing liquids, in particular partial cavitation on foils. When a foil is held stationary in a uniform and constant inflow stream, the appearance of the cavity on the suction side goes - under influence of decreasing cavitation number  $\sigma$  - through various stages from inception to super cavitation. For foils with a suction peak in the pressure distribution inception occurs near the peak's location. The cavity develops to a small and fairly stable attached cavity when  $\sigma$  is lowered. Upon further growth of the size of the cavity fluctuations appear, particularly in the tail part of the cavity. This is followed by fully dynamic behaviour in which clouds of cavitation are more or less regularly shed. It occurs typically when the cavity has reached a length of 0.35 – 0.5 of the foil's chord length. More stable conditions return once the length of the cavity clearly exceeds the chord length: the super cavitation condition.

In the dynamic stage of behaviour an important role is attributed to the so-called re-entrant jet. The literature on partial cavitation is full of this peculiar jet. In his invited lecture at the 4<sup>th</sup> International Symposium on Cavitation, Franc [1] expressed his conviction that "the re-entrant jet is the source of the cloud cavitation instability". It is said to penetrate under the cavity, moving opposite to the main flow direction, until it hits the front part of the cavity, pinches off the aft part which is subsequently carried downstream (shedding), upon which a new cavity and a new jet develop and the process is repeated.

The firm position of the re-entrant jet model is primarily due to apparent experimental evidence of a reversed-flow liquid stream penetrating underneath a partial cavity in dynamical situations. But is the widely accepted physical explanation of the visual information correct? Results of RANS-based numerical simulations of cavitating flows have led us to reconsider the relevance of the re-entrant jet model. As a matter of fact, these results demonstrate that the re-entrant jet flow mechanism has been widely misunderstood or misused and that there are physically more realistic alternatives.

In section 2 we give a brief account of the re-entrant jet flow model, conceived as a possible flow pattern in the context of free-streamline theory. Then a description follows of our computational model for cavitating flows and an outline is given of the results of systematic calculations. In section 5 follows a discussion of cavity formation and the underlying flow field, the outcome of which is summarized in the conclusions of section 6.

## 2. SOME BACKGROUND ON THE RE-ENTRANT JET

The re-entrant jet flow model belongs to the realm of the free-streamline theory. The development of this theory was initiated back in the second half of the 19th century (so well before Prandtl introduced his boundary layer theory), and the names of Helmholtz and Kirchhoff are usually attached to it. Free-streamline theory is typically applied to flows in which the free streamlines border jets, wakes or cavities. While the original developers had flows of a single-phase fluid in mind, free-streamline theory has proven to be more successful for two-phase flows (vapour/gas cavities or jets surrounded by air) and plausible reasons for that have been given by Batchelor [2].

The main elements of free-streamline theory applied to cavities formed at the rear of a body are:

- the flow is steady and irrotational;
- free streamlines detach from the body ("free" meaning that their shape is part of the solution) and develop under the condition that the pressure (and thus the velocity) is constant along them;
- a closure model is needed if the cavity is not of infinite extent;
- conformal mapping with complex variables is used to map the flow onto a Riemann surface.

There are several closure models (see Wu [3]) but in relation to cavitating flows the re-entrant jet model (Gilbarg & Serrin [4]) has been the preferred choice. In this model the free streamlines turn back to the rear of the body and a jet flow enters the near-wake or cavity (see Fig. 1). Mathematically this jet flow can escape to a second sheet of the Riemann surface, but from a physical point of view it is a problematic feature. This is an important observation: the re-entrant jet model is a mathematically consistent description of a steady flow, but physically there is no valid steady-flow counterpart. If the re-entrant jet model has any physical meaning it can only occur in unsteady flow and can only exist during a short time lapse.

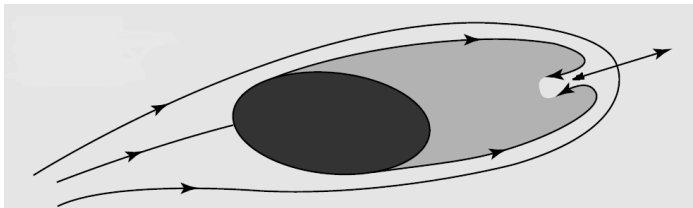


Figure 1: Schematic re-entrant jet flow model.

To be sure, this observation is not new, and it would seem to justify some doubt about the appropriateness of the re-entrant flow model. But any such doubt largely vanished once experimentalists started to report the observation of liquid jets in flows with dynamic cavitation. These liquid jets were immediately and apparently without much further thought identified as re-entrant jets.

Therefore the re-entrant jet flow model continued to be the reference for further theoretical and numerical work. Shortly after the appearance in 1950 of Gilbarg & Serrin's work [4], Tulin [5] introduced the linearised cavitation theory for 2D foils, the applicability of which was gradually extended by himself and several others. The re-entrant jet closure model features in this linearised theory, but it turned out that the differences between

closure models become immaterial as a result of the linearization [6].

The re-entrant jet flow model explicitly reappeared later when boundary-element methods were introduced for the simulation of partial cavitation. In (some of) these methods the re-entrant jet is truncated and the velocity of the flow entering the cavity is imposed (i.e. set equal to the constant velocity on the border of the cavity). Thus these methods have a mass sink in the cavity, to be compensated by a mass source in the external flow. For a partial cavity on a foil the flow pattern is then as sketched in Fig. 2. A streamtube, starting as a part of the inflow, passes over the top of the cavity, curls around the tail and then ends in the cavity. As Tulin [6] observed, this "causes a displacement of the outer streamlines in the *upstream* field, quite opposite to the real situation" (where it occurs in the *downstream* field as a result of wake formation). Moreover, because viscous losses along the streamline ending in the stagnation point aft of the cavity are small, Bernoulli's law tells that the  $C_p$ -value at the stagnation point must be close to 1 (which is indeed the outcome of BEM applications). However, such high pressures have never been measured at that location (e.g. Le & Franc [7]). In Franc & Michel [8] this is attributed to unsteadiness, but this is not at all a convincing argument.

So someone adopting the re-entrant jet flow model has to cope with at least two difficulties: a) mass is not conserved, so that there is no physical equivalent for the mathematically consistent formulation of the re-entrant jet flow model, being a steady flow model and b) how to explain the low pressure in the stagnation point aft of the cavity?

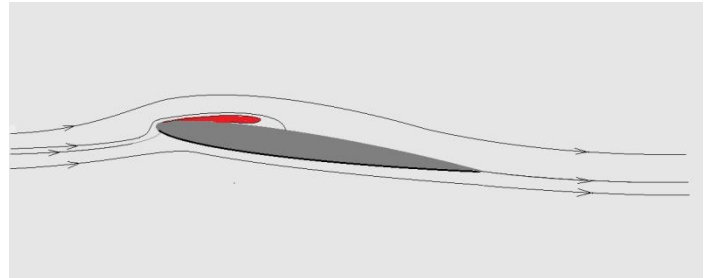


Figure 2: Schematic re-entrant jet flow in BEM modeling

It is relevant to notice here that all models based on potential flow theory have the following assumptions in common:

- in the cavity the vapour concentration is 100 per cent.
- the liquid-vapour interface is a material surface, i.e. locally aligned with the flow.
- motion inside the cavity, if any, is of no concern.

Evidently, if the first assumption is adopted, the second follows more or less as a consequence. For imagine that the interface is perfectly sharp while it is not a material surface. Mass conservation then requires that the velocity component normal to the interface increases by a factor  $\rho_l / \rho_v$ , i.e. roughly 40000 for water, across the interface. If that normal velocity would be only 0.025 per cent of the total velocity it would have to jump to 10 times the total velocity. Momentum conservation would require a pressure jump and a continuous tangential



velocity component across the interface. So the consequence is an abrupt change of velocity, flow direction and pressure. This seems absurd and it is unlikely that we can have a sharp interface which is not a material surface.

But suppose that the vapour concentration need not be 100 per cent everywhere, that phase changes occur in a finite span of time, so in a flowing liquid over a finite distance. This is what is assumed in the RANS model described in more detail in the next section and the results of which will be discussed in the sequel. The assumption of a sharp interface is abandoned. Admittedly this is partly for convenience: in a surface capturing method the interface is never sharp. But it seems also physically justifiable, if not on micro scale then at least on the scale of spatial and temporal resolution pertinent to RANS simulations. Motion inside the cavity is a natural part of the solution and as we shall see this leads to remarkable changes in the picture of partial cavitation and the underlying flow field.

### 3. MATHEMATICAL MODEL

When the pressure in a liquid drops below the saturated vapour pressure at the prevailing temperature, the liquid is in an unstable state and normally tends to form vapour pockets. So the fluid is locally either in liquid or in vapour state, if the presence of non-condensable gas is neglected. A cavitating flow is then a two-phase flow. On a macro scale we might also say that the fluid can be in a mixed state, i.e. small regions exist which are nevertheless big enough to be partly filled with liquid, partly with vapour. In our numerical simulations we even assume that the continuum hypothesis still applies so that we can deal with cavitating flows by solving continuum equations for a single, variable-density fluid. It means that no discontinuous changes occur in the density, nor in any of the other variables like velocity and pressure. The implication is that the liquid-vapour interface is never sharp; it has a finite thickness. As we have observed, this is in contrast with inviscid-flow models of cavitation. Support for the realism of this choice will be given in section 5. An advantage of the single-fluid approach is that there are no restrictions on the topology of the cavity: it allows break-up of a cavity and shedding of vapour clouds.

To compute cavitating flows we use a mathematical model consisting of the RANS equations applied to a variable-density fluid, complemented with an evaporation/condensation model (Hoekstra & Vaz [9]). We have used the  $k-\omega$  SST turbulence model (without modification of the eddy viscosity in the vapour region) in all computations. Compared to the RANS equations for an incompressible fluid, the density is an extra variable next to velocity, pressure and turbulence variables. The density is linked to the vapour volume fraction via

$$\rho = \alpha_v \rho_v + (1 - \alpha_v) \rho_l$$

In order to close the system of equations, the evaporation/condensation model is added, which is in our case a transport equation for the vapour volume fraction with a source/sink term:

$$\frac{\partial \alpha_v}{\partial t} + \nabla \cdot \alpha_v \mathbf{u} = \frac{S}{\rho_v}$$

The formulation of this source/sink term largely follows the proposal by Sauer/Schnerr [10, 11] and is here written as

$$\frac{S}{\rho_v} = 3 \left( \frac{4}{3} \pi n_0 \right)^{1/3} (1 - \alpha_v)^{1/3} (\alpha_v)^{2/3} \text{sign}(p_v - p) \sqrt{\frac{2 |p_v - p|}{3 \rho_l}}$$

which shows a dependency on the vapour volume fraction itself, on the difference  $p_v - p$  and on a multiplier with the single free parameter of the source term:  $n_0$ . This is the number of nuclei per unit of volume, in our computations chosen as  $n_0 = 10^8$ . To avoid misunderstanding, we note that it is just an amplification factor on the source term. Even if  $n_0$  has a low value, evaporation starts at any location where the pressure drops below the vapour pressure; we would have to add stochastic properties to the model to make that cavitation starts only when a nucleus is available.

### 4. DISCUSSION OF SIMULATION RESULTS

We have taken the NACA0015 foil, a symmetric foil with a thickness/chord ratio of 0.15, as a suitable test case for computational work. At six degrees angle-of-attack the flow past the foil in absence of cavitation is attached (no boundary layer separation) and the pressure distribution on the foil shows a suction peak close to the leading edge. Extensive experimental work on this foil has been done by the groups of Arndt and Keller (e.g. [12]). Kjeldsen and Arndt [13] have produced an overview diagram of the cavitation behaviour which is reproduced here in Fig. 3.

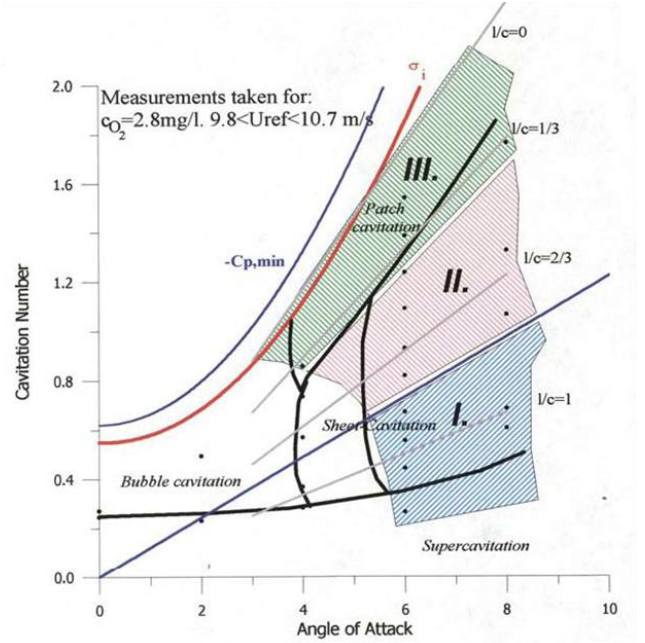


Figure 3: Cavitation behaviour of the NACA0015 foil as a function of cavitation number and angle-of-attack (from [13]).

All our calculations have been made for 2D conditions with the foil placed in a laterally constrained flow field. Free-slip tunnel walls were adopted, the height of the flow domain being 0.57 m while the chord length of the foil is 0.2 m. With an inflow speed of 6 m/s, the characteristic Reynolds number is

$Rn = 1.2 \times 10^6$ . The foil was set at six degrees angle-of-attack by rotating the foil about its centre of gravity which is at  $0.3086 c$  behind the leading edge. A low free-stream turbulence level was assumed by setting the eddy viscosity at the inlet plane equal to  $\mu_t = 0.01 \mu_l$ , where  $\mu_l$  is the dynamic viscosity of water  $\mu_l = 1.002 \times 10^{-3} \text{ kg/ms}$ . The main vapour properties were chosen as  $\rho_v = 0.024 \text{ kg/m}^3$  and  $\mu_v = 1.02 \times 10^{-5}$ .

In Hoekstra&Vaz [9] an account has been given of the results of computations with the mathematical model presented above in the more or less steady regime. We shall again describe here the main features of the cavity behaviour and the underlying flow as a function of the cavitation number, including the transition to dynamic behaviour (to be discussed in detail in a forthcoming paper [14]). In non-cavitating flow conditions the boundary layer is attached on both the suction and the pressure side of the foil. The boundary layer is laminar on the nose of the foil but - as follows from the level of the eddy viscosity - transition to a turbulent flow state takes place on both the suction and the pressure side.

As a direct consequence of the chosen evaporation model, inception of cavitation occurs for  $\sigma_i = -C_{p_{\min}}$ , which is 2.08 according to our computations. This fits nicely in the overview picture in Fig. 3.

The global state of affairs from inception to  $\sigma = 1.3$  (steady flow regime) is summarized in Fig. 4. On the horizontal axis is the relative chord position and on the vertical axis the cavitation number from high to low values. The two red lines mark the position on the foil of begin and end of the cavity, respectively, the black lines the separation and reattachment points, while the blue line indicates how far liquid penetrates underneath the cavity.

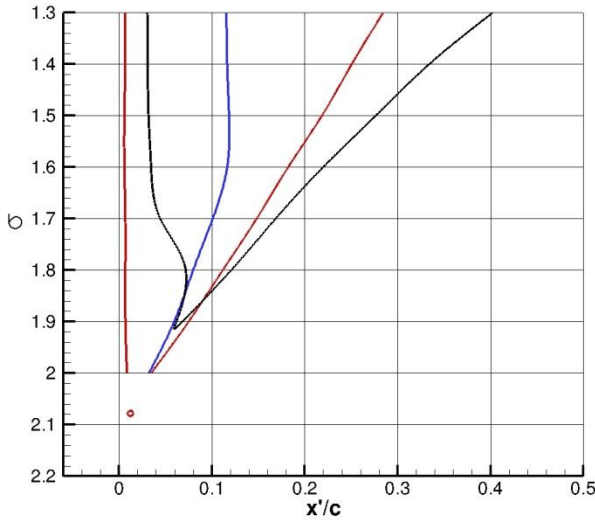


Fig. 4: Cavity length, extent of separation zone and liquid penetration depth for NACA0015 as a function of the cavitation number. Red: cavity extent (measured on 50% vapour fraction), Black: extent of separation zone, Blue: liquid penetration depth underneath the cavity, Red circle: inception point.

Cavitation first appears as a very thin sheet. For an observer it is a stationary (attached) cavity, i.e. its position is locked with respect to the foil, but the vapour is produced, travels along the foil over some distance and then condensates. As a salient feature, it has its tail part lifted from the foil surface (liquid under the tail). Clearly, this is a result of the velocity distribution in the boundary layer, because at high velocity the distance traveled by the vapour until it has fully condensated to liquid is longer than at low velocity.

Although there is expansion and the streamlines tend therefore to bend away from the foil near the front end of the cavity and to bend back to the foil at the tail of the cavity (with a accompanying change in the pressure distribution), the boundary layer does not separate in the early stages of cavity development. The vapour volume fraction is as yet below 1 in the whole cavity. The lift force is slightly higher than in non-cavitating flow.

But at  $\sigma$  just above 1.9, about when the lift reaches its maximum value, cavitation-induced boundary layer separation starts and a recirculation zone develops, bordered by separation and re-attachment points. Notice that from now on there is a liquid stream in the direction opposite to the main stream. But the cavity is stationary and an experimentalist confronted with such a state of affairs is unlikely to call it a re-entrant jet. And with good reasons, because the liquid stream in the direction opposite to the main stream is just a part of the flow in the recirculation zone, and not - as in the re-entrant jet model - coming from the external flow, curling around the cavity tail.

Flow separation starts under the tail of the cavity in the liquid part of the flow. This is physically plausible, considering the change in the pressure distribution caused by the appearance of cavitation. But the separation point moves to inside the cavity (black line crossing blue line in Fig. 4), although staying downstream of the front end of the cavity.

While the developed cavity is steady in the mean, cavity and recirculation zone partly overlap, as Fig. 5 indicates. It shows the situation (with the vertical scale blown up) for  $\sigma = 1.4$ . Notice the differences with the re-entrant jet model: there is no flow curling around the tail of the cavity. The streamline, ending in the stagnation point aft of the cavity (reattachment point) is in a steady flow of course connected with the separation point. It is the streamline bordering the recirculation zone. This immediately explains why  $C_p$  is far below 1 in the reattachment point.

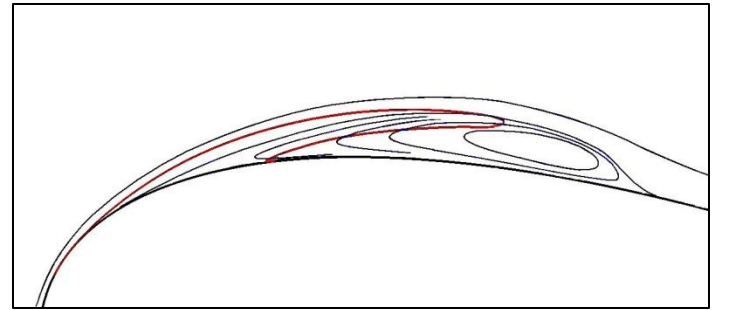


Fig. 5: Cavity outline ( $\alpha_v=0.5$  contour in red) and recirculation zone for a stable partial cavity

When the reattachment point passes mid-chord it gradually loses its strong foothold on the foil. As a result, the aft end of the cavity first starts to “breathe” but as the reattachment point nears the trailing edge an interaction with the flow at the tail of the foil is observed. From potential flow simulations we know how important the Kutta condition is for the lift production. In the present viscous flow computations we see the direction in which the flow leaves the trailing edge change, the lift force decreases, the location of the stagnation point on the nose of the foil changes and the cavity shrinks. The decreasing lift implies that part of the circulation around the foil will be shed, so a vorticity cloud (with clockwise rotation if the flow is from left to right) travels over the suction side. The boundary layer separation point moves aft and the recirculation zone is swept from the foil, upon which a new cycle starts. The maximum lift force during the oscillation cycle exceeds the lift under non-cavitating conditions.

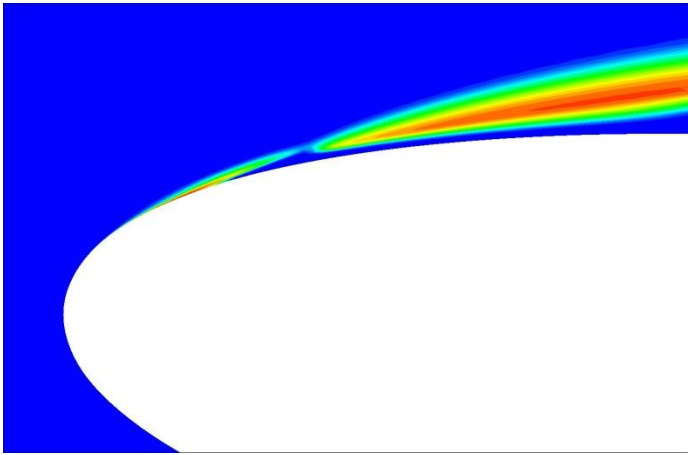


Figure 6: Example of computed break-up of partial cavity at its front end (NACA0015,  $\sigma=1.0$ ).

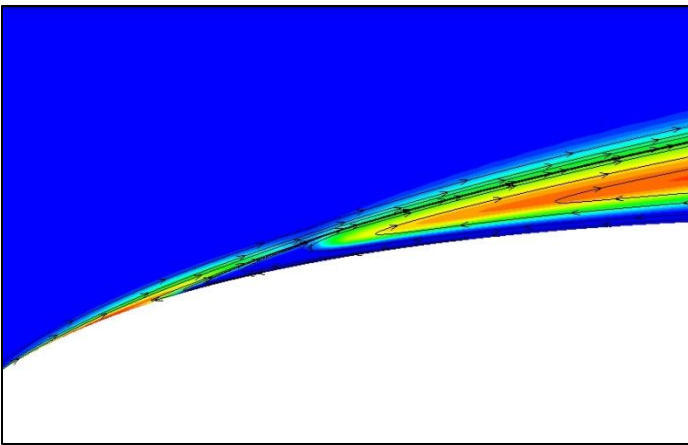


Figure 7: Detail of figure 6 with streamlines added.

The flow behaviour in the dynamic phase has strong similarity with what happens around an airfoil under dynamic stall (McCroskey [15]), in particular in what McCroskey calls the *deep stall* condition. There, of course, the frequency of the dynamic behaviour is determined by the forced pitching motion

of the foil while in our case the foil is stationary and dynamics is invoked by a natural instability. But the variation in the lift force and the flow phenomena associated with it are similar.

Like it has been observed in several experiments, also in the computations the sheet cavity sometimes breaks up close to the front end (see Fig. 6 for an example). It seems then - by visualizing the vapour distribution only - that the liquid under the cavity finds a way out and escapes to the external flow. But on inspection of the underlying velocity field nothing of the kind is happening (Fig. 7). That the re-entrant jet breaks through the cavity is a visual illusion.

## 5. PARTIAL CAVITATION AND UNDERLYING FLOW

When assuming the flow to be inviscid and the liquid-vapour interface to be a material surface and sharp, there are difficulties in explaining what happens for a partial cavity on a foil at the front end of the cavity as well as at the aft end. At the front end, Franc & Michel [8] give two options: a) the tangential detachment, where the flow separation point and the begin of the cavity coincide and where the flow leaves the foil surface with continuity of curvature or b) cavity detachment downstream of laminar flow separation. Since the first option seems somewhat artificial, they advocate the second option. We cite: “ a well developed cavity always detaches downstream of laminar separation of the boundary layer. The existence of separation (.....) is the only opportunity for a cavity to remain attached to the wall and to be sheltered from the incoming flow. If the boundary layer does not separate, the cavity is swept away by the flow and cannot attach to the smooth wall.” But the same authors saw also the consequences and posed the cavity detachment paradox: if the cavity must be preceded by laminar boundary layer separation, which itself is caused by an adverse pressure gradient, the liquid upstream of the separation must apparently be under tension and one would expect cavitation to appear there.

Our calculations show that if nuclei of suitable size are abundantly present in the flow, cavitation appears *ahead* of the separation point. Indeed, flow separation can appear only after the presence of a cavity has created the conditions to invoke it, viz. an enhanced adverse pressure gradient. In the computational results the liquid-vapour interface at the forward end of the cavity is not a material surface. Streamlines enter the cavitation region and there is a continuous production of vapour, which is traveling with the flow. This production requires a pressure below the vapour pressure as is clear from the source function formulation presented in section 3, which can give a positive source value only under that condition. This means that a pressure below the vapour pressure is a necessary condition for the flow near the location where cavitation starts to appear.

Also the flow at the tail of the cavity has never got a plausible physical explanation and indeed if the assumption is maintained that the border between cavity and liquid is sharp conflicts are unavoidable. But we have too long been preoccupied with the assumptions of inviscid flow and their consequences. Since also in experiments the tail of the cavity does not look sharp it seems appropriate to abandon the assumption of perfectly sharp interfaces. Our computational results [9] show that also then realistic cavity shapes and extents are predicted, but they give a kind of flow at the tail of the

cavity totally different from what the re-entrant jet model suggests, as has been illustrated with Fig. 5.

Only in dynamic conditions, when the recirculation zone is growing in size (so during a small part of the oscillation cycle), it might be filled with liquid from the external flow. There are two mechanisms for the growth of the zone, it expands because more vapour is produced in the zone, or it is filled by the external flow (indeed, an unsteady variant of the re-entrant jet mechanism). The first mechanism is evidently active. Whether that holds for the second mechanism as well might be confirmed by visualizing particle paths, but even if it is active then it is surely not the feature governing the dynamic process. Sato *et al.* [16] have earlier drawn a similar conclusion based on their experimental work for somewhat longer (“transitional”) cavities, that “the re-entrant jet appears as a result of transitional cavity oscillation rather than being the cause of it”.

What then about the experiments carried out by Kawanami *et al.* [17], which have been considered as the proof of the essential role of the re-entrant jet? They fitted a small bar perpendicular to the main flow direction on the suction side of a foil and showed that this had a strong influence on cloud shedding. But what does this prove actually? Such a bar will also disturb the flow in the recirculation zone, so is likely to influence the dynamic behaviour.

A last remark is in place. We have related the occurrence of instability and thus of cloud cavitation to the interaction of the cavity-induced flow separation with the trailing edge flow. We do not claim or suggest that it is the only mechanism for instability. For instance, Pham *et al.* [18] report to have found small scale waves on the liquid-vapour interface. As Fig. 5 indicates, the shear layer separating from the foil is in the middle of the cavity and a Kelvin-Helmholtz instability might well develop. Also the results of Arndt *et al.* [12], Leroux *et al.* [19] and Coutier-Delgosha *et al.* [20] have demonstrated that dynamic cavity behaviour depends on the angle-of-attack or rather on the ratio of cavitation number and angle-of-attack. But then, considering the variety and complexity of events under dynamic stall conditions as described by McCroskey [15], what else can we expect?

## 6. CONCLUSIONS

The mathematical model used in our calculations of cavitating flows is not perfect, and certainly not good enough to simulate correctly all aspects of such a complex phenomenon as cavitation. Besides, all observations made in this paper are based on numerical simulations for just one foil, the NACA0015, at a fixed angle of attack of 6 degrees. Therefore, not only have the results to be considered with reservation, we have also to be careful with generalisations. On the other hand, the model is undoubtedly more realistic than any potential-flow based model, and - importantly - it gives clear answers to questions which are problematic in the context of the assumptions made in inviscid flow models. Mass is conserved, the low  $C_p$  in the reattachment point is explained, and there is no cavity detachment paradox. Therefore we have sufficient confidence in our results to call the story of the re-entrant jet a myth.

Our results have shown that a sheet cavity developing on a foil is quick to create flow conditions causing flow separation. So except for very small cavity extent, a partial cavity is usually

accompanied by a flow recirculation zone (supposing that the flow reattaches to the foil aft of the cavity). The flow recirculation zone implies the existence of a reversed flow adjacent to the foil surface. So there is a flow in the direction opposite to the main flow direction from the reattachment point (which is typically beyond the tail of the cavity) to the separation point. This reversed flow is not necessarily merely a liquid flow, phase changes may well occur in the recirculation zone. In that case the liquid-vapour interface may be stationary (in nominally steady flows) or it may move (under dynamic conditions) but not – as a rule – with the local fluid speed.

One is free to call this a re-entrant jet flow, of course, but that is likely to put us on a wrong footing when interpretation of experimental results is at stake. The picture of a liquid stream curling around the cavity tail, a result of the re-entrant jet flow model, is then almost unavoidably in our mind. But that picture has been found to be highly misleading. So why not leave the re-entrant jet for what it is: a mathematically consistent, but physically troublesome flow model as a product of the free-streamline theory. In interpreting experimental results of partial cavitation it is essential to conceive a physically consistent underlying flow pattern; to think in terms of a recirculation zone caused by cavitation (or enhanced by cavitation if flow separation is already present in the non-cavitating flow); to realize that this recirculation zone may partly overlap the cavity, and that the motion of the cavity boundary is not necessarily moving with the local speed of the fluid.

This should make us aware that it is not sufficient just to look at cavitation, because the movement of the cavity border as today’s high-speed cameras show us is not necessarily the same as the movement of fluid particles. Then it turns out that a re-entrant jet that pushes the interface forward until it reaches the front end of the cavity and then cuts the cavity into two parts is a visual illusion.

## REFERENCES

- [1] Franc, J. P. (2001) Partial cavity instabilities and re-entrant jet. *4th Int. Symp. on Cavitation (CAV2001)*, California Institute of Technology, Pasadena, California.
- [2] Batchelor, G.K. (1967) *An Introduction to Fluid Dynamics*, Cambridge University Press.
- [3] Wu, T. Y. (1972) *Cavity and wake flows*. Annual Review of Fluid Mechanics, **4**, 243-284.
- [4] Gilbarg, D. & Serrin, J. (1950) Free boundaries and jets in the theory of cavitation. *J. Mathematics and Physics*, **29**, 1-12.
- [5] Tulin, M. P. (1953) Steady two-dimensional cavity flows about slender bodies. DTMB Report no. 843.
- [6] Tulin, M. P. (2003) On the theory and modeling of real cavity flows. *5th Int. Symp. on Cavitation (CAV2003)*, Osaka, Japan.
- [7] Le, Q., Franc, J.P. and Michel, J.M. (1993) Partial Cavities: Global Behaviour and Mean Pressure Distribution, *J. Fluids Engineering*, **115**, 243-248.
- [8] Franc, J. P. & Michel, J.M. (2004) *Fundamentals of Cavitation*, Vol. 76 in the series Fluid Mechanics and its Applications, Kluwer Academic Publishers.

- [9] Hoekstra, M. & Vaz, G.. (2009) The partial cavity on a 2D foil revisited. *7th Int. Symp. on Cavitation (CAV2009)*, AnnArbor, Michigan.
- [10] Sauer, J. (2000) Instationär Kavitierende Strömungen - Ein Neues Modell, Basierend auf Front Capturing (VoF) und Blasendynamik. *PhD University of Karlsruhe*, Germany.
- [11] Schnerr, G. H. & Sauer, J. (2001) Physical and numerical modeling of unsteady cavitation dynamics. *4th Int. Conf. on Multiphase Flow*, New Orleans, USA.
- [12] Arndt, R.E.A., Song, C.C.S., Kjeldsen, M., He, J. and Keller, A. (2000) Instability of Partial Cavitation: A Numerical/Experimental Approach, 23<sup>rd</sup> Symp. on Naval Hydrodynamics, Val de Reuil, France.
- [13] Kjeldsen, M. and Arndt, R.E.A. (2000) Spectral characteristics of sheet/cloud cavitation, *J. Fluids Engineering*, **122**, no. 3, 481-487.
- [14] Hoekstra, M. (2011) Exploratory RANS Simulations of Partial Cavitation and its Dynamics, paper to be presented at the 4<sup>th</sup> Int. Conf. on Computational Methods in Marine Engineering (MARINE 2011), Lisbon, Portugal.
- [15] McCroskey, W.J. (1981) The Phenomenon of Dynamic Stall, NASA Technical Memorandum 81264.
- [16] Sato, K., Tanada, M., Monden, S and Tsujimoto, Y. (2002) Observations of Oscillating Cavitation on a Flat Plate Hydrofoil. *JSME Int. Jnl., Series B*, Vol. 45, No.3, 646-654.
- [17] Kawanami, Y., Kato, H., Yamaguchi, H., Tagaya, Y. and Tanimura, M. (1996) Mechanism and Control of Cloud Cavitation, *J. Fluids Engineering* **119**, 788-795.
- [18] Pham, T.M., Larrarte, F. and Fruman, D.H. (1999) Investigation of Unsteady Sheet Cavitation and Cloud Cavitation Mechanisms, *J. Fluids Engineering* **121**, 289-296.
- [19] Leroux, J-B., Coutier-Delgosha, O. and Astolfi, J.A. (2005) A joint experimental and numerical study of mechanisms associated to instability of partial cavitation on two-dimensional hydrofoil. *Physics of Fluids* **17**.
- [20] Coutier-Delgosha, O., Stutz, B., Vabre, A. and Legoupil, S. (2007) Analysis of cavitating flow structure by experimental and numerical investigations, *J. Fluid Mechanics* **578**, 171-222.